University of Alberta

Photothermal Effects and Mesoporous Silica Encapsulation of Silicon Nanocrystals

by

Sarah Regli

A thesis submitted to the Faculty of Graduate Studies and Research
in partial fulfillment of the requirements for the degree of

Master of Science

Chemistry

Spring 2012
Edmonton, Alberta

This thesis is dedicated to my inspirational father,

Philip J. Regli

Abstract

The present thesis describes preliminary studies required for evaluating silicon nanocrystals (Si-NCs) as photothermal (PT) therapy agents and drug delivery vehicles. Group 14 semiconductor NCs are of particular interest for these applications because of their tailorable optical response and biological inertness.

Detailed studies of the PT efficiencies of different sized Si-NCs were performed. It was found the PT response exhibited by the presented Si-NCs showed a clear size dependence leading to the proposal that its origin is dominant due to the phenomenon of carrier cooling.

Mesoporous silica is a promising material for drug delivery applications because of its intrinsic high surface area and tailorable pore size. A surfactant-templated approach is described within this thesis that affords effective encapsulation of Si-NCs within 30 nm mesoporous silica nanospheres, The resulting photoluminescent particles were evaluated in proof-of-concept drug release investigations.

Acknowledgements

First and foremost, I would like to thank “the bossman”, Dr. Jon Veinot. He was the first person to just believe in me as a scientist even when I didn’t believe in myself. He doesn’t just form a group of researchers but he forms a family. I feel so blessed to have been a part of this family while having been away from my own family. With that I would also like to thank the entire Veinot group/family for all of their continued support throughout this process.

Dr. Joel Kelly, you at many times were a mini-supervisor for me. You were definitely my scientific role-model (other than your lab messiness). Thank you so much for your guidance throughout this journey of mine. Dr. Jose Rodriguez-Nunez, you instantly took the time to guide me within the lab and although you intimidated the heck out of me in the beginning you have always been someone I have looked up to. The two of you taught me to toughen up and be confident in my work.

Out of the current Veinot group, two members in particular deserve thanks for constantly challenging me and always being open to scientific discussions, Melanie Hoffman and Zhenyu Yang. Thank you guys for always being ready to write some science on glass walls (and always ready for some spontaneous push-ups).

Amber Shukaliak and Marie Barnes deserve a special thank you for being tremendous help as undergraduate researchers. You two are incredibly talented and I’m excited to see what the future holds for you!

Three of my closest companions here at the University of Alberta deserve thanking and include Melanie Hoffman, Adam Malcolm, and Dr. Matt Zamora. Melanie, although thanked for her overwhelming support in the group has also served as one of my biggest support networks in my personal life too. It only took her actually getting my name right in order for us to become exceptionally close friends. Adam Malcom, we became friends my very first day at the UofA and all torture and pranks aside, I am so grateful to have gone through this process with you. Dr. Matt Zamora, you have been an amazing friend helping me through this entire process, whether it be calming my nerves for my first conference or blowing off thesis writing steam you truly helped me get through it.

My wonderful interdisciplinary group of friends Shawn Compton, Marco Taucer, Amelia Walker, Mike Reid, Laura Poole and Nick Arkell, you guys have been a constant support network and I appreciate all of your help. For continuing support since being Guelph undergraduates I'd like to thank Michelle Boudreau and Natasha Holmes and for continued support since high school I would like to thank Julie Vu, Ashley Dutra and Britanny Carlos.

All of this would not have been possible without the support from both Regli and Manchee families back in Ontario. Specifically my brother Adam Regli and father Philip Regli who have been consistent inspirational tools for me.

Finally, I would like to thank the person who has been through it all with me, my partner Kyle Manchee. The two of us really embody "Chemical Physics" and whether it's at home, on the ski hill, or in the lab you have been an incredible part of this journey. I can't wait for what's next.

Table of Contents

Chapter 2: Photothermal Effect of Silicon Nanocrystals

List of Tables

List of Figures

List of Schemes

List of Symbols, Nomenclature, and Abbreviations

Ω: Ohm

ħ: Reduced Planck constant

μ: reduced mass of electron and hole effective masses

Au-NPs: Gold nanoparticles

BSA: Bovine serum albumin

CdSe: Cadmium selenide

cm^{-1}: Wavenumber

CuSe: Copper selenide

CTAB: cetyltrimethylammonium bromide

D.I.: De-ionized

DLS: Dyanmic light scattering

EFTEM: Energy filtered transmission electron microscopy

EtOH: Ethanol

E_c: Conduction band

$E_{exciton}$: Exciton energy

E_f: Fermi energy

E_g: Energy band-gap

E_v: Valence band

eV: Electron volts

Fe_3O_4: Iron oxide

GaAs: Gallium arsenide

Ge: Germanium

HF: Hydrofluoric acid

HRTEM: High resolution transmission electron microscopy

HSQ: Hydrogen Silsesquioxane

IBU: Ibuprofen

K: Kelvin

k: Wavevector

k-space: Momentum space

LaB_6: Lanthanum Hexaboride

LC: Liquid crystal

MCM-41: Mobil Composition of Matter number 41

meV: millielectron volts

MIBK: Methyl isobutyl ketone

MnO-NPs: Manganese oxide nanoparticles

MPS: Mesoporous silica

MRI: Magnetic resonance imaging

NaOH: Sodium hydroxide

NC: Nanocrystal

NIR: Near-infrared

NP: Nanoparticle

NR: Nanorod

NW: Nanowire

p: Momentum

PEG: Polyethlyene glycol

PEG-silane: 2-[Methoxy(polyethyleneoxy)propyl] trimethyoxy silane

PL: Photoluminescence

PT: Photothermal

PTFE: Polytetrafluoroethylene

PTT: Photothermal therapy

QD: Quantum dot

QY: Quantum yield

Si: Silicon

Si-NCs: Silicon nanocrystals

Si-NWs: Silicon nanowires

TEM: Transmission Electron Microscopy

TEOS: Tetraethoxy silane

Ti: Titanium

TOPO: Trioctylphosphine oxide

TGA: Thermogravimetric Analysis

UV: Ultraviolet

VIS: Visible

Chapter 1: Introduction to Silicon Nanocrystals

1.1 Semiconducting Materials

Semiconductors are, as the name suggests, materials that exhibit partial conductivity. Materials can generally be classified either as metallic, semiconducting or insulating. Metals are typically those that display electrical conductivity (movement of electrons) in the presence of an external electric field.[1,2] Insulators are those that do not display electrical conductivity in the presence of an electric field. Semiconducting materials lie within a grey area somewhere in between the definitions laid out for metals and insulating materials. At sufficiently high temperatures they can display electrical conductivity, but at 0 K, have full occupation of closely spaced energy states and movement of electrons is prohibited in the presence of an electric field.[1] The conditions for the different behaviour will be described in more detail below, but for the present discussion, it is important to note that semiconductors can exhibit either conducting or insulating properties depending upon their surroundings.

Metals have highly diffuse atomic orbitals which allow electrons to interact directly with nuclei from other atoms to create continuous bands of available energies over a large distance.[3,4] These continuous bands, permit the delocalization and by extension movement of electrons when exposed to an electric field leading to metallic conductivity. Metals usually exhibit conductivities in the 10^5-10^{10} $\Omega^{-1}cm^{-1}$ range.[5]

For nonmetals, the electrons used for bonding strongly interact only with a small number of neighboring atoms resulting in electrons being held more tightly to the atomic nuclei (i.e., bonds are localized).[3] As a result of the strong

interaction of the electrons to the atomic nuclei, nonmetals are unable to form continuous bands of available energies over large distances, and instead form many non-overlapping band sets.[3] The lower (filled) energy band set is referred to as the valence band (E_v) whereas the higher (empty) energy band set is referred to as the conduction band (E_c). The energy difference between the conduction and valence band is referred to as a band-gap (E_g) and is known as the energy required to promote an electron to permit conductivity.

$$E_g = E_c - E_v \quad \textbf{[1]}$$

This band-gap is what defines the material as a semiconductor or insulator (or a semi-metal, but these materials will not be discussed). The material band-gap is depicted schematically in Figure 1.1. Typically, a semiconductor is classified as a material with a band-gap between 0 eV and 4 eV, while an insulator has a band-gap greater than 4 eV.[6] Semiconductors usually exhibit conductivity in the range 10^{-9}-10^{2} $\Omega^{-1}cm^{-1}$.[5] Some examples of semiconducting materials include bulk crystals of silicon, germanium, gallium arsenide, indium antimonide, and cadmium selenide.[5] Insulators generally exhibit conductivity in the range of $<10^{-9}$ $\Omega^{-1}cm^{-1}$.[5] Some examples include quartz, calcium fluoride and alumina.[5]

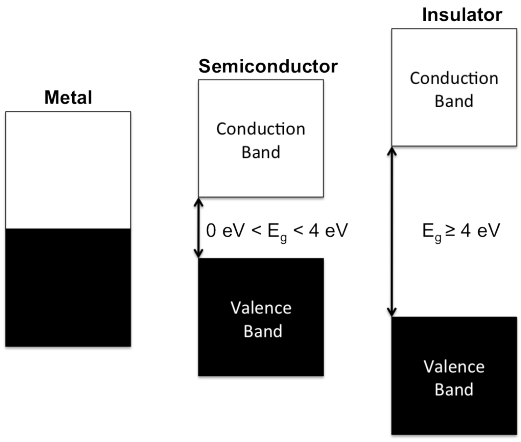

Figure 1.1: Schematic band-gap for a metal, semiconductor and insulator

Although the ranges in conductivity differ for metals and semiconductors, the most notable difference between metals and semiconductors is the temperature dependence of conductivity. A metal has reduced conductivity at higher temperatures, whereas a semiconductor has increased conductivity due to promotion of an electron from the valence to the conduction band, resulting in conductivity.[5] This temperature dependence presents a "grey-area" in the definition of semiconductors when considering electrical conductivity alone because at low temperatures semiconductors can exhibit insulating properties, and at high temperatures insulators can exhibit conducting properties.[5] Temperature and impurities can determine a semiconductor's conductivity and thus, give methods of tuning the conductivity.[6] The exquisite tunability of semiconductor electronic properties provides the foundation for modern electronics and these materials have had a monumental impact on our society.

1.2 Energy-band Characteristics for 3-dimensional Crystalline Semiconductors

When considering a molecule, molecular orbital theory is frequently used to describe the spread of electrons over all of the atoms in a molecule and its electronic properties.[7] In a bulk crystal, the electronic properties are governed by the periodicity of the material.[8] Treating the system using a periodic potential that modifies the wavefunction of electrons in a solid can approximate the periodic nature of a crystal. The resulting wavefunctions are known as Bloch functions and are written as: [9]

$$\psi_k = \sum_n e^{ikna} \chi_n \qquad \textbf{[1.2]}$$

where ψ is the electronic wavefunction, χ is the basis function representing atomic orbitals, *a* is the lattice spacing of the repeating unit, *n* is an atomic index, and *k* is an index indicating the number of irreducible, discrete representations of the wavefunction. This variable *k* is also referred to as a wavevector and is used as a label for quantized energy states. The wavevector, *k*, is proportional to the momentum, *p*, of an electron:

$$\vec{p} = \hbar\vec{k} \qquad \textbf{[1.3]}$$

Using a periodic potential, the relationship between energy *E*, and wavevector *k*, becomes challenging to evaluate compared to the relationship predicted from the free electron model where the potential is set to zero.[8] Using the free electron model, the energy depends on the absolute square of the wavevector and is given by the relationship: [9]

$$E = \frac{\hbar^2 k^2}{2m} \qquad \textbf{[1.4]}$$

Where m is the electron effective mass. This relationship is represented in Figure 1.2.

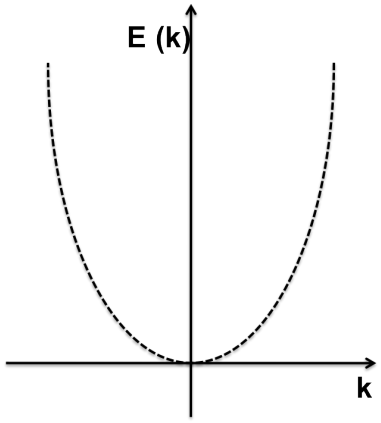

Figure 1.2: Free Electron Model Energy dispersion (One-dimensional case)[9]

Using k as the independent variable (i.e., Figure 1.2) plots energy as a function of wavevector and is often referred to as k-space. The reciprocal space (k-space) energy curve predicted by the free electron model is made up energy levels, quantized with k, that form what appears as a continuous band. This is the simplest depiction of how a continuous band is formed from atomic energy levels in a periodic lattice, however, the free electron model predicts no band gaps and cannot explain insulating or semiconducting behaviour.

We can include the periodicity of a lattice by using the nearly free electron model (using a weak periodic potential), the reciprocal space energy curve has some similarities to the free electron model but band-gaps are introduced (areas of forbidden electron occupation) this is shown in Figure 1.3a. By introducing a

periodic potential, energy relations should be equivalent at each lattice point and a reduced zone scheme can be represent by a lattice translation (Figure 1.3b).[8]

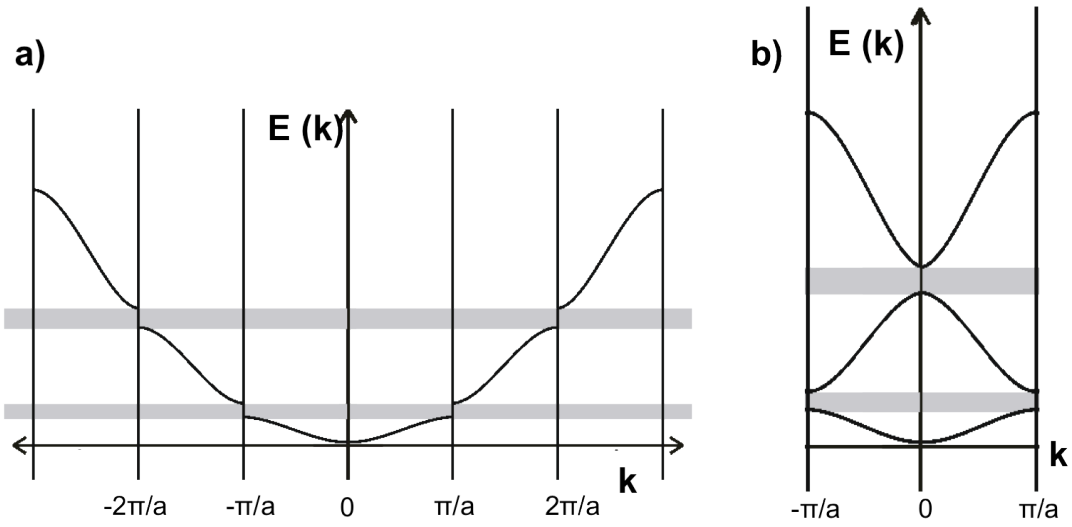

Figure 1.3: Nearly free electron model energy dispersion (one dimensional) a) for large k, b) the reduced zone scheme [8]

This is a simplified depiction of where the source of a band structure in a solid originates. In reality, the reduced zone scheme for a 3-dimensional structure is quite complicated as is shown in Figure 1.4 for 3-dimensional crystals of silicon (Figure 1.4a) and gallium arsenide (Figure 1.4b).[10] Here, the band structure is again the reduced zone scheme where the labels on the wavevector axis correspond to locations of high symmetry. This figure shows the band-gap for these materials and corresponds to 1.1 eV for silicon and 1.43 eV for GaAs.[10]

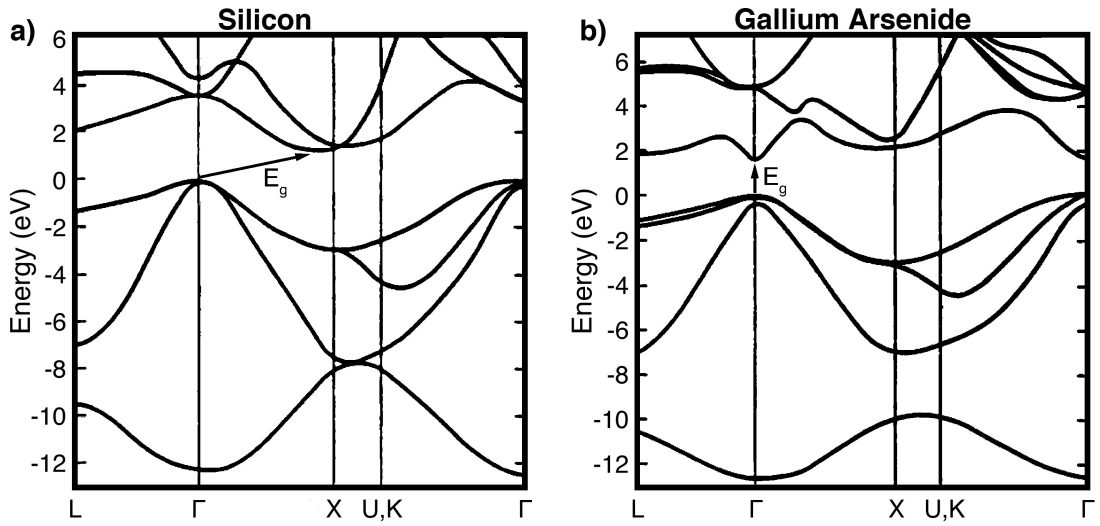

Figure 1.4: Energy band structure for a) silicon and b) gallium arsenide (adapted from reference 10)

One important aspect of Figure 1.4 is how the locations of the conduction and valence bands, differ between Si and GaAs. For GaAs (Figure 1.4b), the maximum of the valence band and the minimum of the conduction band are at the same coordinate in k-space, whereas the locations of the bands in k-space differ for Si. This is where these semiconductors can be classified. Semiconductors in which the valence band maximum and the conduction band minimum are at the same location in k-space are termed direct band-gap semiconductors; if they are at different locations in k-space they are referred to as indirect semiconductors.[7] For a direct band-gap, the promotion of an electron requires only a change in the electron energy and is possible with photon absorption.[8] For an indirect band-gap semiconductor a change in electron momentum is required for a band-gap transition and since photons carry negligible momentum, the absorption of a photon is not sufficient. As a result, lattice vibrations, also known as phonons, are

required to provide this change in momentum. In other words, the electronic transition (electron promotion) must be phonon-mediated.

When an electron located in the valence band undergoes a vertical transition it leaves behind a vacancy that is available for occupation by another electron, followed by another, causing a cascade of electrons. In this context, the vacancy can be viewed as a positive charge carrier (or hole) propagating throughout the valence band (see Figure 1.5).[5] For conductivity in semiconductors, both the electron and the hole are contributors and these species are referred to as carriers where holes are carriers of positive charge, and electrons, carriers of negative charge.[5]

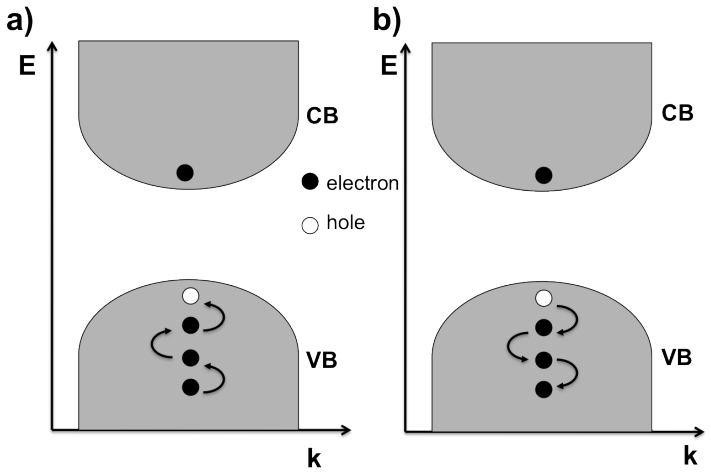

Figure 1.5: Movement of a) electrons and b) holes in the valence band of a semiconductor

Electrons and holes can form a bound electron-hole pair due to the Coulomb interaction between the particles; the resultant pair is referred to as an exciton.[5] Excitons are held together by an energy referred to as the exciton binding energy and takes on values of 14.3 meV for Si[11] and 4.4 meV for GaAs.[5]

When the thermal energy is less than the exciton binding energy, exciton recombination is responsible for photon emission in a semiconductor; otherwise emission is due to free electron-hole recombination.

For bulk crystals, light emission is poor for an indirect band-gap semiconductor compared with a direct band-gap semiconductor. The participation of a third body, a phonon, (in addition to the electron and hole) is required to conserve energy and momentum, causing the recombination rate to be substantially lower and resulting in long carrier recombination lifetimes (μs – ms range). This is in stark contrast to the short recombination times observed for direct band-gap semiconductors (ps – ns range).[12] When the energy from an excited state carrier is exchanged in the form of a phonon, it is referred to as a non-radiative recombination method.[5]

Since the microelectronics industry is dominated by silicon, it is an element of tremendous interest.[3] The remainder of this chapter and thesis focuses on the properties of silicon, and its behaviour as an indirect semiconductor.

1.3 Reducing the Dimensions in Silicon Materials

In bulk silicon, impurities can enhance conductivity. For large tunability of the carrier density, semiconductors can be doped with different atoms that act as donor or acceptor atoms.[6] For example, introducing aluminum (i.e., $2x10^{19}$ cm^{-3}) into the silicon (diamond) crystal structure, a shortage of electrons will provide free holes in the valence band; similarly, introducing phosphorus ($4x10^{20}$ cm^{-3}), free electrons in the conduction band.[11] This addition of impurities is termed

doping. Since these carrier concentrations can be tailored, tremendous control over the properties of the Si is possible. This has lead to the wide-ranging applications of Si in electronic devices such as diodes, transistors, logic gates, and integrated circuits.[13]

Reducing dimensions has a profound effect in many materials including Si. These effects are apparent when observing the density of states and the changes that arise within different dimensions; this is shown schematically in Figure 1.6. Density of states of a system, describes the number of available states at a given energy. The density of electron and hole states can be expressed in the general form:

$$D(E) \propto E^{\frac{d}{2}-1} \qquad \textbf{[1.5]}$$

Where *d* represents the dimensionality for 3, 2, and 1 dimensions and a number of discrete sub-bands appear due to the quantum confinement effect.[1]

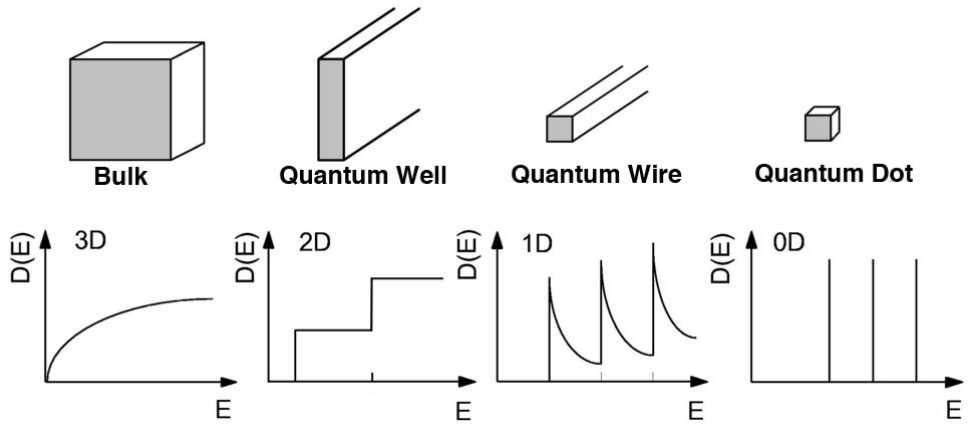

Figure 1.6: Density of electron states for different dimensionalities; Right to left decreasing in dimension beginning with 3-dimension (adapted from reference 1)

Confining materials within 2 dimensions forms a quantum well. In a structure of this type, the density of states is constant and does not depend on energy for a given energy level (Figure 1.6). These structures have found applications in laser diodes,[14,15,16] waveguides,[17,18,19] and high electron mobility transistors,[20,21,22] although most of the listed examples have been reported for GaN, GaAs, and GaP type structures. For Si, these structures are generally formed by sandwiching a thin semiconductor layer of nanometer dimension between materials of a wider band-gap; this structure effectively confines carriers to the semiconducting layer.[23] For silicon, this has been achieved by forming thick layers of silicon nitride outside of a thin silicon layer using plasma enhanced chemical vapour deposition with SiH_4/ He and NH_3/N_2 gas mixtures.[24] This has also been achieved by sandwiching silicon between SiO_2 layers, where Si is vapour deposited onto a SiO_2 film followed by thermal oxidation of the outer surface.[25]

Confinement of materials to one dimension, leads to quantum wires. Nanowires (NWs) are receiving significant attention for their potential applications in devices such as field effect transistors,[26,27] photodetectors,[28,29] biochemical sensors,[30,31] light-emitting diodes,[32,33] and complementary logic devices.[34,35,36]. For Si, there are many different approaches to forming NWs,[37, 38] some examples include using electron-beam lithography,[39, 40, 41] vapour-liquid-solid growth,[42, 43] and solution based syntheses using metal nanoparticle seeds (liquid-liquid-solid).[44, 45]

Further confining silicon in all dimensions leads to what is considered to be a "0-dimensional" structure. "Zero dimensional", crystalline semiconductors are often referred to as quantum dots (QDs) or nanocrystals (NCs).[46] From Figure 1.6, it is apparent that bands become quantized for zero-dimensional structures and hence "zero dimensional" structures exhibit atomic-like behaviour. By confining the electron and hole, exciton recombination has a higher probability and photoluminescence (PL) is often observed from these structures.[46] PL properties can be tuned by controlling NC size, due to an effect known as quantum confinement. The following sections describe quantum confinement in silicon and the discovery of room temperature PL from silicon. Finally, various synthetic methods for preparing silicon nanocrystals (Si-NCs) are outlined.

1.4 Quantum Confinement in Silicon Nanocrystals

Tailoring material properties through controlling particle size is a unique capability of inorganic, semiconducting solids. As shown earlier, as a structure approaches 0-dimensions, the density of states begins to undergo discretization. This is depicted schematically in Figure 1.7, where discrete band edges are formed for a NC to approach the zero dimensional limits. In Figure 1.7, shading indicates filling of electrons, filling up to what is known as the Fermi energy, E_f.[47] As a crystallite size begins to approach the zero dimensional limits, bands become discrete starting with the band edges; this process has a great effect on the size of band gaps,[47] and strongly affects the characteristics in semiconductors where the Fermi level lies at the center of a band gap, whereas in a metal, discretization at

the band edges has little to no effect on the charge carriers at the Fermi level existing at the center of a band.

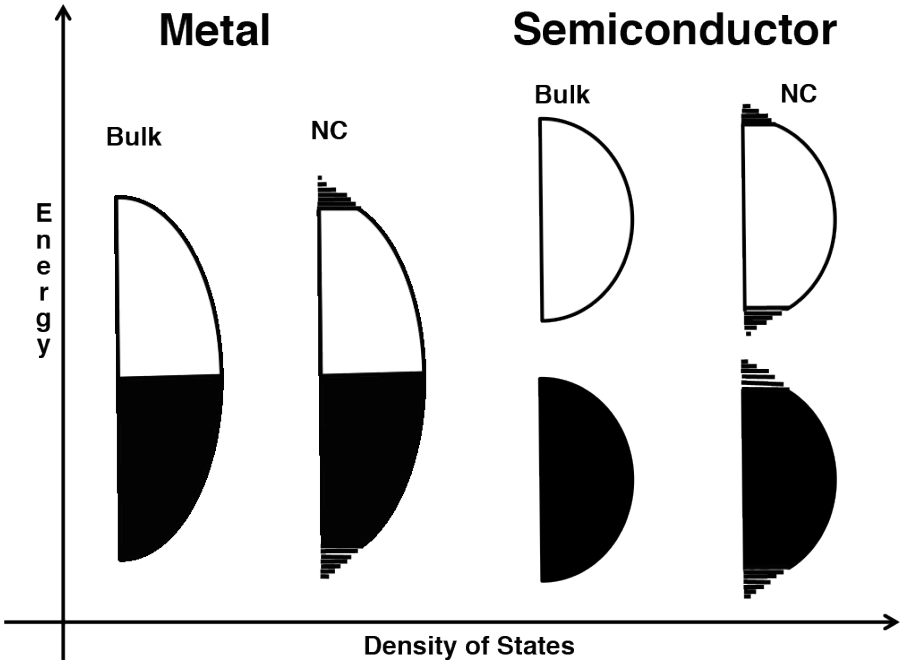

Figure 1.7: Density of states for bulk and nanocrystalline metals and semiconductors (adapted from reference 47)

Quantum confinement in a NC is observable when the NC size becomes comparable to the natural length scale of an exciton.[46, 47] This natural length, where and electron and a hole are bound, is known as the Bohr exciton radius, a_B, and is material dependant.[46] For silicon, the Bohr exciton radius is 4.3 nm.[1] Strong confinement of the charge carriers occurs when the radius of the NC is smaller than the Bohr exciton radius, but larger than the lattice spacing. By treating the exciton as a particle in a box (box being the size of the NC), energy levels can be obtained:[46]

$$E_{n_x n_y n_z} = \frac{\hbar^2 \pi^2}{2\mu}\left(\frac{n_x^2}{L_x^2} + \frac{n_y^2}{L_y^2} + \frac{n_z^2}{L_z^2}\right) \qquad \textbf{[1.6]}$$

Where n is an integer representing quantization, μ is the reduced mass of the electron and hole effective masses, and L is the length of the box. It is apparent from this rough treatment that energy levels are dependent on the size of the box, and the spacing between levels (or band gap) increases with decreasing box size.

A more accurate treatment is treating exciton as a spherical particle inside of a spherical potential well; the energy dependence on size can be determined using the earlier described Bloch functions.[1, 46] This yields:

$$E_{exciton} = E_g + \frac{\hbar^2 \chi_n^2}{2r^2 \mu} - E_c \qquad \textbf{[1.7]}$$

Where E_g is the band-gap energy, r represent the NC radius, χ are roots of spherical Bessel functions, and E_c is an energy correction that arises from the Coulombic attraction from the electron and the hole.

From these treatments, it is apparent that when the radius of a NC becomes smaller than the material's Bohr exciton radius, quantum confinement arises and the confinement energy of each carrier scales as $1/a^2$.[46] Therefore when NC size decreases, the spacing between energy levels increases, increasing the band-gap of the material. For silicon, this arises when the NC radius becomes smaller than 4.3 nm.[1]

1.5 Room Temperature Photoluminescence from Silicon

One of the first reports displaying room temperature PL from silicon was from Furukawa *et al.* who showed a photograph of a red emission from ultrafine silicon particles formed from magnetron rf sputtering.[48] Later, in 1990, a report by Canham, showed room temperature red PL from porous silicon (p-Si), formed from the electrochemical and chemical dissolution of bulk silicon.[49] It was found as the length of time for chemical dissolution (using hydrofluoric acid as the chemical etchant) increased, a blue-shift was observed in the PL.[49] This can be observed in Figure 1.8.

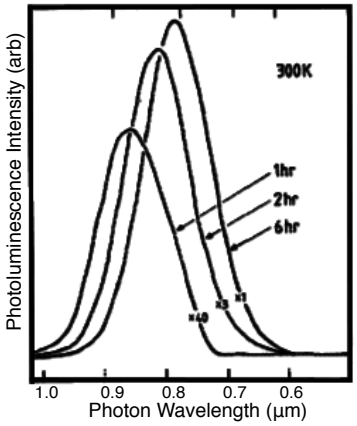

Figure 1.8: PL spectrum from p-Si using 514 nm line of an Ar laser showing PL blue shift with increased etching time (adapted from reference 49)

Since the energy of the photons (> 1.4 eV) are larger than the band-gap of bulk silicon (1.11 eV), these observed results were attributed to quantum confinement in these p-Si materials.[49] While the origin of this PL is still a matter under debate, it is believed that as pores begin to develop and enlarge, pores begin to overlap resulting in small isolated regions of confined silicon to form.[50]

Quantum confinement from these small silicon domains is one postulation as to where the room temperature red PL emission originates.[50] Using synchrotron studies, it was determined that the PL from porous silicon originated from light absorption of elemental Si and not due to an extrinsic oxide defect as had been proposed.[51]

Since this discovery, the development of synthetic techniques for Si-NCs has been tremendous. The followings sections aim to describe some of these synthetic techniques and their specific applications.

1.6 Silicon Nanocrystal Synthetic Methods

In this section, synthetic methods for the preparation of Si-NCs have been categorized into four sub-sections; solution-based precursor reduction, physical methods, gas-phase precursor reduction, and oxide-embedded.

1.6.1. Solution-Based Precursor Reduction

Of all synthetic methods, solution-based methods are the most widely studied for the synthesis of semiconductor and metal nanocrystals, however due to the complex reactivity of silicon, these methods are limited for Si-NC synthesis.[52]

One of the first reports for a wet-chemical synthesis of Si-NCs, was the reduction of $SiCl_4$ and $RSiCl_3$ by sodium metal at 385°C at high pressures to form Si-NCs ranging from 5-3000 nm in size (Scheme 1.1A).[53] A variation on this synthesis was later reported by Dhas *et al.*, who reduced $Si(OEt)_4$ (tetraethoxysilane, TEOS) with sodium metal using ultrasonication at -70°C to

form Si-NPs, which were later thermally processed at 400°C to form Si-NCs (Scheme 1.1B).[54]

Various reports have shown the formation of Si-NCs, upon reaction of $SiCl_4$ with various zintl salts (i.e., KSi, NaSi, Mg_2Si) to form chloride terminated NC surfaces (Scheme 1.1C).[55,56,57] A homogeneous reduction method was reported using $LiAlH_4$ to reduce $SiCl_4$ to yield Si-NCs, however this method was not recommended and an erratum was published due to the unnoted side product of pyrophoric silane making this an unsafe solution technique (Scheme 1.1D).[58,59,60,61] A safer variation on this method, was to use sodium napthalide as a reducing agent to yield chloride terminated Si-NCs (Scheme 1.1E).[62] It was also shown; that by using a precursor salt, hydride terminated Si-NCs could be formed (Scheme 1.1F).[63]

Scheme 1.1: Different solution based reduction methods to form Si-NCs (adapted from reference 64)

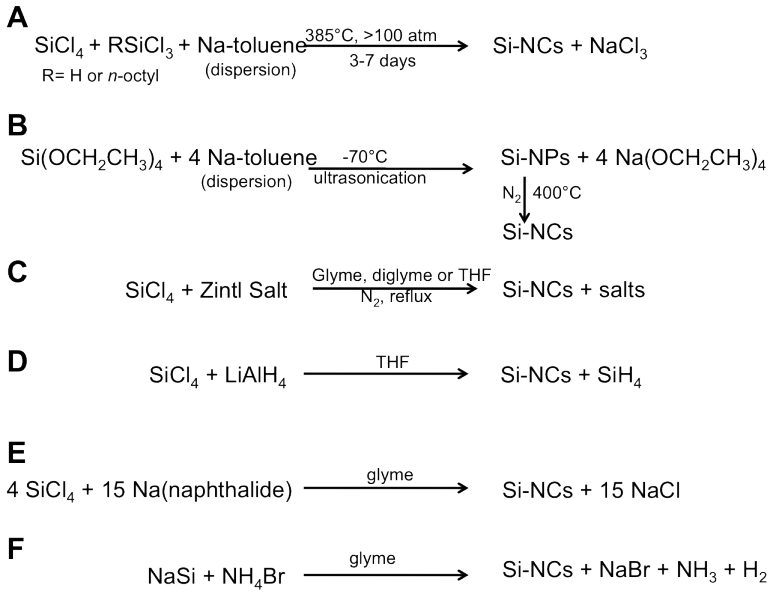

One of the major issues associated with many solution-based methods is their large size distributions, and the lack of PL tunability as these methods typically yield blue emitting Si-NCs.[56, 58]

1.6.2. Physical Methods for Silicon Nanocrystal Formation

There are a few reports in the literature that utilize mechanical methods to yield Si-NCs. One particular method is to form Si-NCs by grinding and sonicating p-Si.[65,66,67] Although data suggests these methods are not individual Si-NCs, but larger structures with NC domains, these methods have shown tunability to yield various emitting species ranging from red to blue emissions.[65,67]

Another physical method for the formation of Si-NCs, is the mechanochemical synthesis of Si-NCs using a high energy ball mill to fracture bulk silicon chunks into small Si-NCs.[68, 69] This method yielded NCs less than 10 nm in diameter and a solution that exhibited blue emission upon UV-excitation.[68] Again with physical methods, control over size distribution and PL tunability maintained to be an issue.[68]

1.6.3. Gas-Phase Precursor Decomposition

Numerous reports describe the decomposition of silane or disilane, to form Si-NCs.[70,71,72,73,74,75] First reports showed that large NCs (30-80 nm in size) could be formed by flowing a silane/hydrogen gas mixture through an epitaxial reactor.[70] An extension of this flowed disilane through a pyrolysis oven using a hot aerosol to control growth and aggregation.[72] The most commonly reported

methods for gas-phase decomposition methods currently, involve CO_2 laser pyrolysis of silane,[71,73] or a non-thermal plasma treatment of silane.[75,76] Both methods provide effective decomposition of the silane precursor to yield red luminescent, hydride terminated Si-NCs 3-5 nm in size.[73,76]

1.6.4. Oxide Embedded Silicon Nanocrystals

Silicon rich oxides (SROs) are a specific type of solid precursor readily able to form Si-NCs embedded in an inert silica matrix, and have been particularly of interest for their applications in non-volatile memory.[77,78] These typically consists of thermally processing SiO_x forms of the oxide ($0 \leq x \leq 2$). Due to the relative thermodynamic instability of SiO_x sub-oxides, thermal processing causes disproportionation of the oxide into elemental Si and the thermodynamically stable oxide, SiO_2.[79] Wang *et al*. reports as the temperature of SROs (in an inert atmosphere) increases between 300-400°C amorphous Si-NPs begin to rapidly nucleate with precipitation of silicon atoms onto existing clusters as the temperature is increased, followed by crystallization of the NPs at 1100°C.[79]

These sub-oxides are generally formed by ion implantation or chemical vapour deposition using SiH_4 and N_2O as reactant gases, followed by thermal processing to yield Si-NCs embedded in SiO_2.[80,81,82,83] Variations in NC sizes (and thus PL) can be achieved by varying Si content (i.e., x) and different thermal processing conditions.[80,84]

SROs can also be formed using different sol-gel methods (Appendix A). One method reported the use of triethoxysilane ($HSi(OEt)_3$) as a sol-gel precursor to form SROs under acid catalyzed conditions (Scheme 1.2A).[85] The authors showed this SRO could be thermally processed at 1050°C or higher to form oxide embedded Si-NCs with a red emission. A variation on this method is using $HSiCl_3$ as a sol-gel precursor to similarly form SROs, addition of water is all that is required in this method, as HCl is readily formed upon hydrolysis further catalyzing the sol-gel reaction (Scheme 1.2B).[86] This method was also shown to yield red-emitting Si-NCs after thermal processing of the oxide-composite at temperatures of 1100°C or greater.

Scheme 1.2: Sol-gel reactions yielding SROs; A) Using triethoxysilane as a precursor, B) using trichlorosilane as a precursor

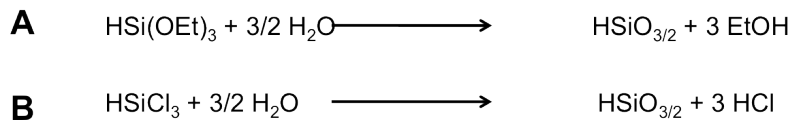

1.6.5. Hydrogen Silsesquioxane as a Precursor for Oxide Embedded Silicon Nanocrystals

Silsesquioxanes are molecules composed of a silicon and oxygen framework with an empirical formula of $RSiO_{3/2}$ where R may be a variety of different chemical functionalities.[87] These molecules are solution processable, and commonly exist as ladder or cage structures.[87] Hydrogen silsesquioxane (HSQ) is a well studied, cage-structured silsesquioxane with a molecular formula of H_{8}-

Si_8O_{12} (Scheme 1.3).[88] It has been found that upon oxidative thermal treatment the HSQ cage structure collapses into a SiO_2 network releasing SiH_4 as a by-product.[89] In 2006 Hessel *et al.*, treated HSQ as a SRO and upon thermal processing in a reducing atmosphere found that Si-NCs embedded in a silica matrix could be formed (Scheme 1.3).[90] The presence of crystallites upon thermal processing at 1100°C was detected using x-ray diffraction (XRD) (Figure 1.9).

Scheme 1.3: Thermal processing of HSQ yielding Si-NCs embedded in a silica matrix (adapted from reference 90)

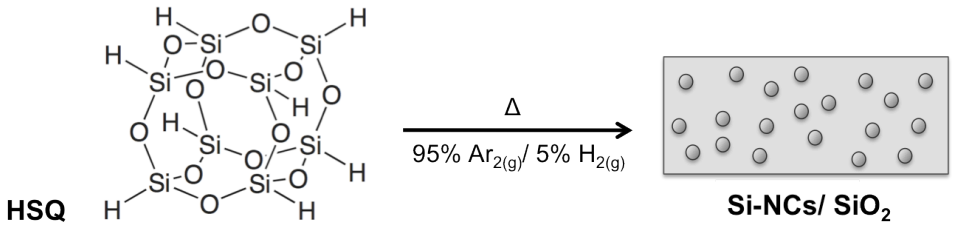

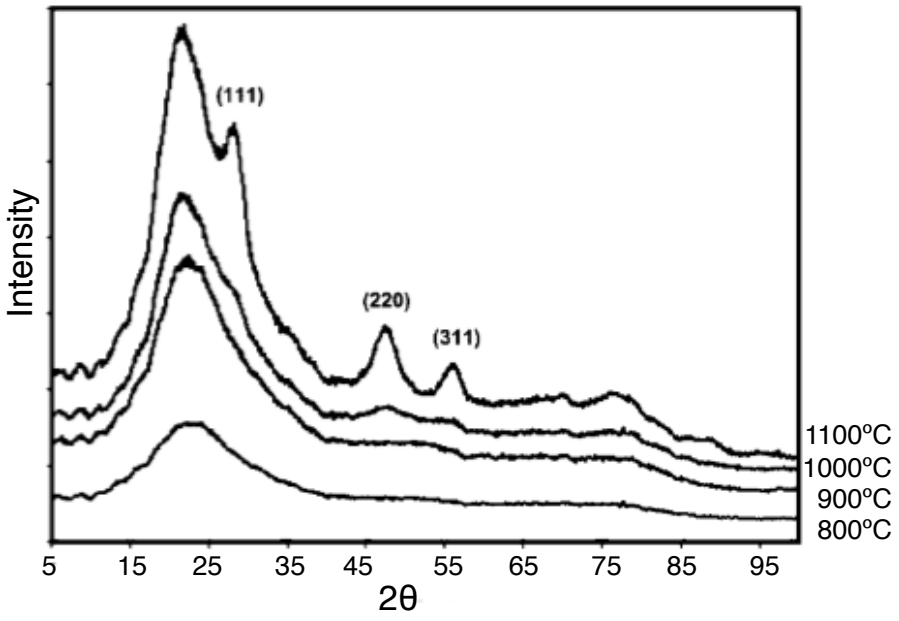

Figure 1.9: XRD of the thermally processed HSQ-derived oxide composites at different temperatures (adapted from reference 90)

Upon imaging the oxide composite with transmission electron microscopy (TEM), the authors found small NCs exhibiting a red PL (Figure 1.10). In order to obtain freestanding Si-NCs, the authors performed a hydrofluoric acid (HF) etch to remove the silica matrix yielding hydride terminated Si-NCs.[90,91] A blue-shift in the PL was observed over increased etching periods, tuning NC emission across the visible spectrum (Figure 1.11).[90] Hessel *et al.* proved that HSQ was an effective precursor for the formation of luminescent, oxide embedded Si-NCs.

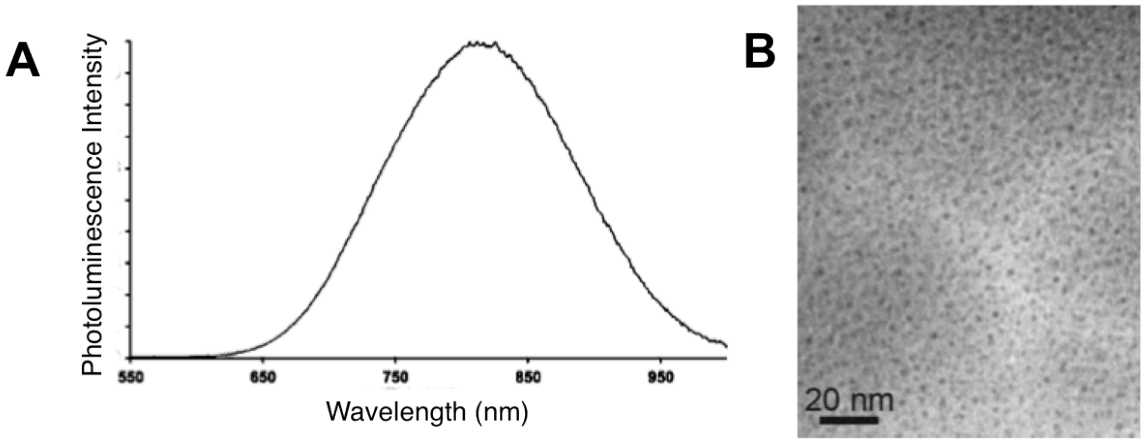

Figure 1.10: A) PL of the HSQ-derived NC/oxide composite B) TEM of the NC/ oxide composite (adapted from reference 90)

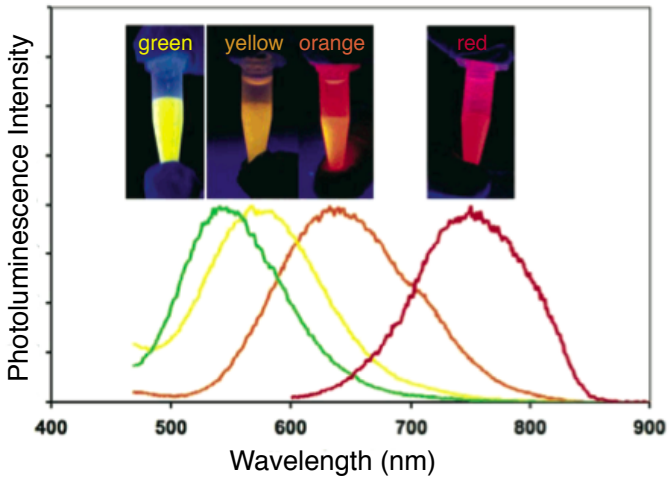

Figure 1.11: PL of hydride terminated Si-NCs after different etching times (adapted from reference 90)

A subsequent report by Hessel *et al.* found that larger Si-NCs could be formed upon thermal processing of HSQ at higher temperatures.[92] Oxide composites processed at 1200°C, 1300°C, and 1400°C exhibited red-shifted PL and peak narrowing in XRD, consistent with quantum confinement (larger NCs having a smaller band-gap).[92] The strange result, however, arose from HSQ processed at 1100°C for 24 hours. Authors found a significant PL red-shift after thermally processing HSQ for 24 hours, however no change in crystallite size was observed upon XRD characterization.[92] Authors attributed this result to the passivation of volume defects after prolonged heating causing larger NCs that would normally appear "dark" to be luminescent, therefore red-shifting the PL.[92] Both of these reports showed HSQ to be an effective precursor to form Si-NCs with tunable PL, into the visible region and extend out into the NIR spectral region with larger NCs or by prolonged thermal processing.[90,92]

1.7 Surface Passivation of Silicon Nanocrystals

Due to an increase in the surface area to volume ratio for NCs, the surface has a large influence on the band-gap of the material.[93,94] When hydride or chloride terminated Si-NCs are exposed to oxygen, the optical properties of the NC are profoundly affected and often compromised.[95] One method to avoid this is to passivate the surface with a layer in order to prevent oxidation and also to provide solution dispersibility. There have been many methods for Si-NC passivation and the following serves as a brief discussion of some of those methods.

1.7.1. Substitutional Approaches

Beginning with a halogen terminated Si-NC, several substitution methods can be performed to yield organic passivated NCs. Yang *et al.* showed chloride terminated Si-NCs could be substituted for an alkyl functionality upon reaction with alkyl lithium or Grignard reagent (Scheme 1.4).[56] Another substitution method reported by Zou *et al.*, showed that chloride termination could be converted to a methoxy terminated upon methanol addition, which subsequently could be hydroxylated with the addition of water, where upon addition of an alkyl trichlorosilane, functionalization would occur based on an oxide layer (Scheme 1.4).[93] Similarly, Li *et al.* found using an alkyl trimethoxysilane, alkyl funtionalization based on an oxide layer could be achieved (Scheme 1.4).[73]

Scheme 1.4: Different substitutional approaches for Si-NCs with alkyl functionalities (adapted from reference 95)

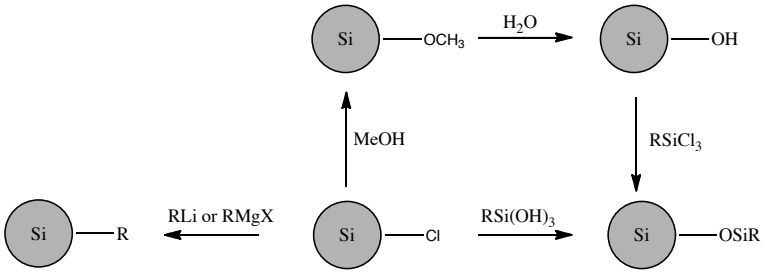

These methods of functionalization of Si-NCs offer solubility in an organic solvent, and photoluminescent stability.

1.7.2. Hydrosilylation

One of the most common methods for Si-NC functionalization is hydrosilylation. Hydrosilylation involves the insertion of an unsaturated bond into silicon-hydride species, and using an alkene or alkyne can result in alkyl termination.[96] Hydrosilylation has been studied extensively for bulk silicon systems and can also be applied to Si-NCs.[96] Some form of initiation is required to allow insertion across the silicon-hydride bond; hydrosilylation can be initiated using a catalyst or by thermal or photochemical initiation. Hydrosilylation offers the advantage of the addition of a variety of functional groups from a terminal alkene or alkyne. Warner *et al.* showed hydrosilylation on hydride terminated Si-NCs could be achieved using a platinum catalyst and allylamine, yielding water-soluble amine terminated Si-NCs (Scheme 1.5).[97,98] There are numerous reports of thermally initiated hydrosilylation using a variety of alkenes,[73,99,100] however,

photochemically initiated hydrosilylation is most commonly reported for reactions with alkenes, alkynes, as well as carboxylic acid acids within the literature (Scheme 1.5).[101,102,103,104,105,106]

Scheme 1.5: Different methods for hydrosilylation of Si-NCs (adapted from reference 95)

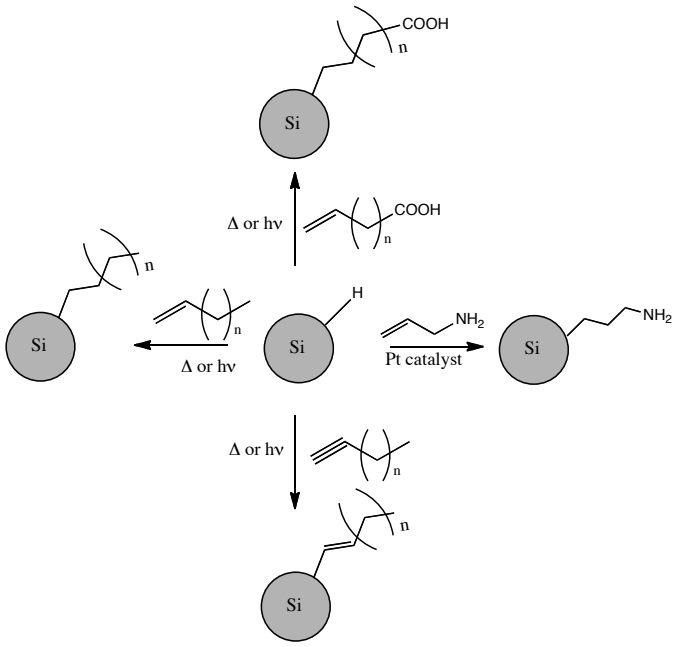

Using hydrosilylation to passivate Si-NCs is a straightforward, versatile method commonly used within the literature and has led to some of the highest photoluminescent quantum yields to date.[107]

1.8 Biological Applications of Silicon Nanocrystals

Semiconductor nanocrystals offer medical applications in fields such as diagnostics, imaging, targeted drug-delivery, and photodynamic therapy.[108] These applications have been particularly investigated for CdSe NCs or quantum dot

(QD) species. Due to the ability to tune surface chemistry, QDs can be modified with a targeting moiety for *in vivo* targeting and imaging of tumour vasculature.[108,109] QDs offer advantages including narrow emission bandwidths, broad excitation, and large Stoke's shifts which favour their use over molecular species as luminescent bio-labels.[110] CdSe QDs have been studied extensively for these biological applications.[111,112,113] However, an unstable surface coating permits air oxidation and can cause the release of highly toxic cadmium ions from the QD core, making toxicity a significant issue in such systems.[108,114,115]

Si has been proposed as a non-toxic alternative for the biological applications studied for CdSe.[116] Although these biological studies have not been studied as extensively as CdSe QDs, there are some reports showing the potential of Si nanostructures for many of the listed biological applications. In 2004 Li *et al.*, demonstrated that polyacrylic acid functionalized Si-NCs could be used as a biological label for fluorescent cell imaging of Chinese hampster ovary cells.[117,118] Erogbogbo *et al.* in 2008 demonstrated fluorescent imaging of live pancreatic cancer cells using micelle encapsulated Si-NCs.[119] In a follow-up study micelle encapsulated Si-NCs were injected into mice for tumour vasculature targeting, sentinel lymph node mapping, and multicolour fluorescent imaging with different sized NCs.[120] These results, while preliminary, hold promise for utilizing Si-NCs for biological applications. The synthesis and characterization of Si-NCs that maintain their PL in aqueous media is vital for future biological applications.

1.9 Thesis Outline

The material in this introduction serves as a foundation for the research presented in the subsequent chapters. This research focuses on the synthesis and functionalization of Si-NCs following methods developed by Hessel *et al.* and Kelly *et al.*[90,104] Chapter 2 presents a fundamental study of the photothermal properties of Si-NCs. This chapter compares the photothermal properties of different NC sizes and proposes a mechanism for where the observed photothermal effect derives from. Chapter 3 studies the synthesis of encapsulating Si-NCs within a mesoporous silica shell. A proof-of-concept drug-delivery study, investigating the possibility of these multifunctional materials as a photoluminescent drug-delivery agent, is present. The final chapter, serves to not only lay out future work of these projects, but to present a proof-of-concept photothermal drug-delivery study as a method of targeted drug-release, bringing unity to both of these divided chapters.

1.10 References

1. Gaponenko, S.V. *Optical Properties of Semiconductor Nanocrystals*; Cambridge University Press: USA, 1998.
2. Mott, N.F.; Jones, H., *The Theory of the Properties of Metals and Alloys*; Dover Publictions: New York, 1958.
3. Minoli, D., *Nanotechnology Applications to Telecommunications and Networking*; John Wiley & Sons: New Jersey, 2006.
4. Smart, L.E.; Moore, E.A., *Solid State Chemistry 3rd Edition*; Taylor and Francis Group: Boca Raton, 2005.
5. Grahn, H.T., *Introduction to semiconductor physics*; World Scientific: Berlin, 1999.
6. Yu, P.Y.; Cardona, M., *Fundamentals of Semiconductors: Physics and Materials Properties 3rd Edition*; Springer: Germany, 2001.
7. Atkins,P.; Overton, T.; Rourke, J.; Weller, M.; Armstrong, F., *Inorganic Chemistry 4th edition*; W.H. Freeman and Company: New York, 2006.
8. Ashcroft, N.W.; Mermin, N.D., *Solid State Physics*, Thomson Learning: USA, 1976.
9. Hoffmann, R., *Angew. Chem. Int. Ed. Engl.*, **1987**, 26 (9), 846-878.
10. Brus, L., *J. Phys. Chem.*, **1994**, 98 (14), 3575-3581.
11. Madelung, O., *Semiconductors- Basic data 2nd edition*; Springer: Germany, 1996.
12. Fauchet, P.M.; Tsybeskov, L.; Peng, C.; Duttagupta, S.P.; von Behren, J.; Kostoulas, Y.; Vandyshev, J.M.V.; Hirschman, K.D., *IEEE J. Sel. Top. Quantum Electron.*, **1995**, 1 (4), 1126-1139.
13. Huff, H., *Into the Nano Era, Moore's Law Beyond Planar Silicon CMOS*; Springer: Germany, 2009.
14. Brendel, M.; Kruse, A.; Jönen, H.; Hoffman, L.; Bremers, H.; Rossow, U.; Hangleiter, A., *Appl. Phys. Lett.*, **2011**, 99 (3), 031106.
15. Dupuis, R.D.; Dapkus, P.D., *Appl. Phys. Lett.*, **1978**, 32 (5), 295-297.
16. Lindström, C.; Burnham, R.D.; Scifres, D.R., *Appl. Phys. Lett.*, **1983**, 42 (2), 134-136.
17. Stievater, T.H.; Rabinovich, W.S.; Park, D.; Khurgin, J.B.; Kanakaraju, S.; Richardson, C.J.K., *Opt. Express*, **2008**, 16 (4), 2621-2627.
18. Fidaner, O.; Okyay, A.K.; Roth, J.E.; Schaevitz, R.K.; Kuo, Y-H.; Saraswat, K.C.; Harris, J.S.; Miller, D.A.B, *IEEE Photonics Technol. Lett.*, **2007**, 19 (20), 1631-1633.
19. Chang-Hasnain, C.J.; Chuang, S.L., *J. Lightwave Technol.*, **2006**, 24 (12), 4642-4654.
20. Rosenberg, J.J.; Benlamri, M.; Kirchner, P.D.; Woodall, J.M.; Pettit, G.D., *IEEE Electron Device Lett.*, **1985**, 6 (10), 491-493.
21. Griem, H.T.; Hsieh, K.H.; D'haenens, I.J.; Delaney, M.J.; Henige, J.A.; Wicks, G.W.; Brown, A.S., *J. Cryst. Growth*, **1987**, 81 (1-4), 383-390.
22. Rabbaa, S.; Steins, J., *J. Phys. D: Appl. Phys.*, **2011**, 44 (32), 325103.

23. Fang, A.Q.; Park, H.; Kuo, Y-H.; Jones, R.; Cohen, O.; Liang, D.; Raday, O.; Sysak, M.N.; Paniccia, M.J.; Bowers, J.E., *Mater. Today*, **2007**, 10 (7-8), 28-35.
24. Steigmeier, E.F.; Morf, R.; Grützmacher, D.; Auderset, H.; Delley, B.; Wessicken, R., **1996**, 69 (27), 4165-4167.
25. Kanemitsu, Y.; Okamoto, S., *Mater. Sci. Eng. B.*, **1997**, 48 (1-2), 108-115.
26. Chang, P-C.; Lu, J.G., *IEEE Trans. Electron Devices*, **2008**, 55 (11), 2977-2987.
27. Wu, X.; Kulkarni, J.S.; Collins, G.; Petkov, N.; Almécija, D.; Boland, J.J.; Erts, D.; Holmes, J.D., *Chem. Mater.*, 20 (19), 5954-5967.
28. Wang, J.; Gudiksen, M.S.; Duan, X.; Cui, Y.; Lieber, C.M., *Science*, **2001**, 293 (5534), 1455-1457.
29. Pettersson, H.; Trägardh, J.; Persson, A.I.; Landin, L.; Hessman, D.; Samuelson, L., *Nano Lett.*, **2006**, 6 (2), 229-232.
30. Ravindran, R.; Sadie, J.A.; Scarberry, K.E.; Yang, H.S.; Bakir, M.S.; McDonald, J.F.; Meindl, J.D., *Electronic Components and Technology Conference*, **2010**, 5490826, 1015-1020.
31. Sirbuly, D.J.; Tao, A.; Law, M.; Fan, R.; Yang, P., *Adv. Mater.*, **2007**, 19 (1), 61-66.
32. Könenkamp, R.; Word, R.C.; Schlegel, C., *Appl. Phys. Lett.*, **2004**, 85 (24), 6004-6006.
33. Hayden, O.; Greytak, A.B.; Bell, D.C., *Adv. Mater.*, **2005**, 17 (6), 701-704.
34. Huand, Y.; Duan, X.; Cui, Y.; Lauhon, L.J.; Kim, K-H.; Lieber, C.M., *Science*, **2001**, 294 (5545), 1313-1317.
35. Morales, A.M.; Lieber, C.M., *Science*, **1998**, 279 (5348), 208-211.
36. Duan, X.; Lieber, C.M., *Adv. Mater.* **2000**, 12 (4), 298-302.
37. Bandaru, P.R.; Pichanusakorn, P., *Semicond. Sci. Technol.*, **2010**, 25 (2), 024003.
38. Teo, B.K.; Sun, X.H., *Chem. Rev.*, **2007**, 107 (5), 1454-1532.
39. Regonda, S.; Aryal, M.; Hu, W., *J. Vac. Sci. Technol. B*, **2008**, 26 (6), 2247-2251.
40. Juhasz, R.; Elfström, N.; Linnros, J., *Nano Lett.*, **2005**, 5 (2), 275-280.
41. Choi, Y-K.; Zhu, J.; Grunes, J.; Bokor, J.; Somojai, G.A., *J. Phys. Chem. B*, **2003**, 107 (15), 3340-3343.
42. Park, W.I.; Zheng, G.; Jiang, X.; Tian, B.; Lieber, C.M., *Nano Lett.*, **2008**, 8 (9), 3004-3009.
43. Wang, Y.; Schmidt, V.; Senz, S.; Gösele, U., *Nat. Nanotechnol.*, **2006**, 1 (3), 186-189.
44. Chan, C.K.; Patel, R.N.; O'Connell, M.J.; Korgel, B.A.; Cui, Y., *ACS Nano*, **2010**, 4 (3), 1443-1450.
45. Heitsch, A.T.; Fanfair, D.D.; Tuan, H-Y.; Korgel, B.A., *J. Am. Chem. Soc.*, **2008**, 130 (16), 5436-5437.
46. Klimov, V.I., *Nanocrystal Quantum Dots 2nd edition*; Taylor and Francis Group: Boca Raton, 2010.
47. Alivisatos, A.P., *J. Phys. Chem.*, **1996**, 100 (31), 13226-13239.
48. Furukawa, S.; Miyasato, T., *Jpn. J. Appl. Phys.*, **1988**, 27 (11), L2207-L2209.

49. Canham,, L.T., *Appl. Phys. Lett.*, **1990**, 57 (10), 1046-1048.
50. Sailor, J.; Kavanagh, K.L., *Adv. Mater.*, **1992**, 4 (6), 432-434.
51. Sham, T.K.; Jiang, D.T.; Coulthard, I.; Lorimer, J.W.; Feng, X.H.; Tan, K.H.; Frigo, S.P.; Rosenberg, R.A.; Houghton, D.C.; Bryskiewicz, B., *Nature*, **1993**, 363 (6427), 331-334.
52. Greenwood, N.N.; Earnshaw, A., *Chemistry of the Elements*, Pergamon Press, New York, 1984.
53. Heath, J.R., *Science*, **1992**, 258 (5058), 1131-1133.
54. Dhas, N.A.; Raj, C.P.; Gedanken, A., *Chem. Mater.*, **1998**, 10 (11), 3278-3281.
55. Bley, R.A.; Kauzlarich, S.M., *J. Am. Chem. Soc.*, **1996**, 118 (49), 12461-12462.
56. Yang, C-S.; Bley, R.A.; Kauzlarich, S.M.; Lee, H.W.H.; Delgado, G.R., **1999**, 121 (22), 5191-5195.
57. Mayeri, D.; Phillips, B.L.; Augustine, M.P.; Kauzlarich, S.M., *Chem. Mater.*, **2001**, 13 (3), 765-770.
58. Wilcoxon, J.P.; Samara, G.A., *Appl. Phys. Lett.*, **1999**, 74 (21), 3164-3166.
59. Huber, D.L.; Wilcoxon, J.P.; Samara, G.A., *Appl. Phys. Lett.*, **2008**, 92 (2), 029902.
60. Wells, A.S.; *Org. Process Res. Dev.*, **2010**, 14 (3), 484-484.
61. Wilcoxon, J.P.; Samara, G.A.; Provencio, P.N., *Phys. Rev. B*, **2007**, 76 (19), 199903
62. Baldwin, R.K.; Pettigrew, K.A.; Ratai, E.; Augustine, M.P.; Kauzlarich, S.M., *Chem. Commun.*, **2002**, (41), 1822-1823.
63. Neiner, D.; Chiu, H.W.; Kauzlarich, S.M., *J. Am. Chem. Soc.*, **2006**, 128 (34), 11016-11017.
64. Veinot, J.G.C., *Chem. Commun.*, **2006**, (40), 4160-4168.
65. Belomoin, G.; Therrien, J.; Smith, A.; Rao, S.; Twesten, R.; Chaieb, S.; Nayfeh, M.H.; Wagner, L.; Mitas, L., *Appl. Phys. Lett.*, **2002**, 80 (5), 841-843.
66. Nayfeh, M.H.; Barry, N.; Therrien, J.; Akcakir, O.; Gratton, E.; Belomoin, G., *Appl. Phys. Lett.*, **2001**, 78 (8), 1131-1133.
67. Bley, R.A.; Kauzlarich, S.M.; Davis, J.E.; Lee, H.W.H., *Chem. Mater.*, **1996**, 8 (8), 1881-1888.
68. Heintz, A.S.; Fink, M.J.; Mitchell, B.S., *Adv. Mater.*, **2007**, 19 (22), 3984-3988.
69. Heintz, A.S.; Fink, M.J.; Mitchell, B.S., *Appl. Organometal. Chem.*, **2010**, 24 (3), 236-240.
70. Murthy, T.U.M.S.; Miyamoto, N.; Shimbo, M.; Nishizawa, J., *J. Cryst. Growth*, **1976**, 33 (1), 1-7.
71. Ehbrecht, M.; Ferkel, H.; Huisken, F.; Holz, L.; Polivanov, Y.N.; Smirnov, V.V.; Stelmakh, O.M.; Schmidt, R., *J. Appl. Phys.*, **1995**, 78 (9), 5302-5306.
72. Wilson, W.L.; Szajowski, P.F.; Brus, L.E., *Science*, **1993**, 262 (5137), 1242-1244.
73. Li, X.; He, Y.; Swihart, M.T., *Langmuir*, **2004**, 20 (11), 4720-4727.

74. Salivati, N.; Shuall, N.; Baskin, E.; Garber, V.; McCrate, J.M.; Ekerdt, J.G., *J. Appl. Phys.*, **2009**, 106, 063121.
75. Liptak, R.W.; Kortshagen, U.; Campbell, S.A., *J. Appl. Phys.*, **2009**, 106, 064313.
76. Anthony, R.; Kortshagen, U., *Phys. Rev. B*, **2009**, 80, 115407.
77. Tiwari, S.; Rana, F.; Hanafi, H.; Hartstein, A.; Crabbé, E.F., *Appl. Phys. Lett.*, **1996**, 68 (10), 1377-1379.
78. Lombardo, S.; De Salvo, B.; Gerardi, C.; Baron, T., *Microelectron. Eng.*, **2004**, 72 (1-4), 388-394.
79. Wang, J.; Wang, X.F.; Li, Q.; Hryciw, A.; Meldrum, A., *Philos. Mag.*, **2007**, 87 (1), 11-27.
80. Shimizu-Iwayama, T.; Kurumado, N.; Hole, D.E.; Townsend, P.D., *J. Appl. Phys.*, **1998**, 83 (11), 6018-6022.
81. Shimizu-Iwayama, T.; Nakao, S.; Saitoh, K.; Itoh, N., *J. Phys. Conden. Matter*, **1994**, 6 (39), L601-L606.
82. Dusane, S.; Bhave, T.; Hullavard, S.; Bhoraskar, S.V.; Lokhare, S., *Solid State Commun.*, **1999**, 111 (8), 431-435.
83. Calleja, W.; Falcony C.; Torres, A.; Aceves, M.; Osorio, R., *Thin Solid Films*, **1995**, 270 (1-2), 114-117.
84. Meldrum, A.; Hryciw, A.; MacDonald, A.N.; Blois, C.; Marsh, K., *J. Vac. Sci. Technol.*, **2006**, 24 (3), 713-717.
85. Sorarù, G.D.; Modena, S.; Bettotti, P.; Das, G.; Mariotto, G.; Pavesi, L., *Appl. Phys. Lett.*, **2003**, 83 (4), 749-751.
86. Henderson, E.J.; Kelly, J.A.; Veinot, J.G.C., *Chem. Mater.*, **2009**, 21 (22), 5426-5434.
87. Li, G.; Wang, L.; Ni, H.; Pittman, C.U.; *J. Inorg. Organomet. Polym.*, **2002**, 11 (3), 124-154.
88. Azinović, D.; Cai, J.; Eggs, C.; König, H.; Marsmann, H.C.; Vepřek, S., *J. Lumin.*, **2002**, 97 (1), 40-50.
89. Yang, C-C.; Chen, W-C., *J. Mater. Chem.*, **2002**, 12 (4), 1138-1141.
90. Hessel, C.M.; Henderson, E.J.; Veinot, J.G.C., *Chem. Mater.*, **2006**, 18 (26), 6139-6146.
91. Williams, K.R.; Muller, R.S., *J. Microelectromech. Syst.*, 5 (4), 256-269.
92. Hessel, C.M.; Henderson, E.J.; Veinot, J.G.C., *J. Phys. Chem. C.*, **2007**, 111 (19), 6956-6961.
93. Zou, J.; Baldwin, R.K.; Pettigrew, K.A.; Kauzlarich, S.M.; *Nano Lett.*, **4**, (7), 1181-1186.
94. Reboredo, F.A.; Galli, G., *J. Phys. Chem. B*, **2005**, 109 (3), 1072-1078.
95. Pavesi, L.; Turan, R., *Silicon Nanocrystals*; Wiley-VCH: Weinheim, 2010.
96. Buriak, J.M., *Chem. Rev.*, **2002**, 102 (5), 1271-1308.
97. Warner, J.H.; Hoshino, A.; Yamamoto, K.; Tilley, R.D., *Angew. Chem. Int. Ed.*, **2005**, 44 (29), 4550-4554.
98. Tilley, R.D.; Warner, J.H.; Yamamoto, K.; Matsui, I.; Fujimori, H., *Chem. Commun.*, **2005**, (10), 1233-1835.

99. Jariwala, B.N.; Dewey, O.S.; Stradins, P.; Ciobanu, C.V.; Agarwal, S., *ACS Appl. Mater. Interfaces*, **2011**, 3 (8), 3033-3041.
100. Kelly, J.A.; Shukaliak, A.M.; Fleischauer, M.D.; Veinot, J.G.C., *J. Am. Chem. Soc.*, 133 (24), 9564-9571.
101. Sato, S.; Swihart, M.T., *Chem. Mater.*, **2006**, 18 (17), 4083-4088.
102. Clark, R.J.; Dang, M.K.M.; Veinot, J.G.C., *Langmuir*, **2010**, 26 (19), 15657-15664.
103. Prtljaga, N.; D'Amato, E.; Pitanti, A.; Guider, R.; Froner, E.; Larcheri, S.; Scarpa, M.; Pavesi, L., *Nanotechnology*, **2011**, 22 (21), 215704.
104. Kelly, J.A.; Veinot, J.G.C., *ACS Nano*, **2010**, 4 (8), 4645-4656.
105. Stewart, M.P.; Buriak, J.M., *J. Am. Chem. Soc.*, **2001**, 123 (32), 7821-7830.
106. Hua, F.; Swihart, M.T.; Ruckenstein, E., *Langmuir*, **2005**, 21 (13), 6054-6062.
107. Jurbergs, D.; Rogojina, E., *Appl. Phys. Lett.*, **2006**, 88 (23), 233116.
108. Azzazym H.M.E.; Mansour, M.M.H.; Kazmierczak, S.C., *Clin. Biochem.*, **2007**, 40 (13-14), 917-927.
109. He, X.; Wang, K.; Cheng, Z., *Wiley Interdiscip. Rev. Nanomed. Nanobiotechnol.*, **2010**, 2 (4), 349-366.
110. O'Farrell, N.; Houlton, A.; Horrocks, B.R., *Int. J. Nanomed.*, **2006**, 1 (4), 451-472.
111. Jamieson, T.; Bakhshi, R.; Petrova, D.; Pocock, R.; Imani, M.; Seifalian, A.M., *Biomater.*, **2007**, 28 (31), 4717-4732.
112. Alivisatos, P., *Pure Appl. Chem.*, **2000**, 72 (1-2), 3-9.
113. Medintz, I.L.; Uyeda, H.T.; Goldman, E.R.; Mattoussi, H.; *Nat. Mater.*, **2005**, 4 (6), 435-446.
114. Alivisatos, A.P.; Gu, W.; Larabell, C., *Annu. Rev. Biomed. Eng.*, **2005**, 7, 55-76.
115. Hardman, R., *Environ. Health Perspect.*, **2006**, 114 (2), 165-172.
116. Park, J-H.; Gu, L.; von Maltzahn, G.; Ruoslahti, E.; Bhatia, S.N.; Sailor, M.J., *Nat. Mater.*, **2009**, 8 (4), 331-336.
117. Li, Z.F.; Ruckenstein, E., *Nano Lett.*, **2004**, 4 (8), 1463-1467.
118. Erogbogbo, F.; Tien, C-A.; Change, C-W.; Yong, K-T.; Law, W-C.; Ding, H.; Roy, I.; Swihart, M.T.; Prasad, P.N., *Bioconjugate Chem.*, **2011**, 22 (6), 1081-1088.
119. Erogbogbo, F.; Yong, K-T.; Roy, I.; Xu, G.; Prasad, P.N.; Swihart, M.T., *ACS Nano*, **2008**, 2 (5), 873-878.
120. Erogbogbo, F.; Yong, K-T.; Roy, I.; Hu, R.; Law, W-C.; Zhao, W.; Ding, H.; Wu, F.; Kumar, R.; Swihart, M.T.; Prasad, P.N., *ACS Nano*, **2011**, 5 (1), 413-423.

Chapter 2: Photothermal Effect of Silicon Nanocrystals

2.1 Introduction

The photothermal (PT) effect is a phenomenon associated with the conversion of incident light to thermal energy. This phenomenon was theoretically predicted in 1961 by Gärtner to be a characteristic of semiconducting materials.[1] In semiconducting materials, this effect was attributed to the diffusion of electron-hole pairs through a crystal, contributing to the thermal conductivity and localized heating. This effect was experimentally observed in 1965 by Gordon *et al.* who observed the time-dependant refraction of an incident laser beam on a transparent sample and proposed this to be the result of light absorption of the material leading to localized heating.[2] Since its discovery, PT effects have been reported for different molecular chromophores (e.g., hemoglobin, indocyanine green, etc.),[3] as well as semiconductor [4, 5, 6] and metal nanostructures.[7, 8, 9] These discoveries have led to a unique research field of photothermal therapy (PTT) where PT materials are explored for their potential uses in cancer phototherapy.

2.1.1. Photothermal Effects in Semiconducting Nanostructures

The PT effect of indirect semiconductors silicon and germanium was predicted in 1961 by Gärtner who predicted mathematically that in semiconductors, when electron-hole pairs are created, they diffuse through the crystal to regions of lower carrier concentrations and contribute to the overall thermal conductivity of the crystal lattice.[1] The challenge in accurately verifying this experimentally lies in the ability to measure the thermal conductivity within

bulk semiconductors before and after irradiation. In recent years however, this PT effect has been experimentally observed in semiconductor nanostructures of Si and Ge.

In 2003, Wang *et al.* observed a PT effect from Si nanowires (Si-NWs) causing the ignition of NWs when exposed to a conventional photographic flash.[4] The PT effect was proposed to increase as a result of quantum confinement effects in Si-NWs, leading to the observed light induced ignition. PT heating was also observed for porous silicon in 2008, by Lee *et al.,* measuring the changes in temperature of an aqueous solution.[10]

Lambert *et al.* explored the PT properties of water-soluble Ge-NCs in 2007.[5] Upon irradiation of an aqueous colloidal suspension of Ge-NCs with a Ti:Sapphire Near-Infrared (NIR) laser, solution temperature was found to increased. This phenomenon was proposed to arise from the localized heating of the Ge-NC core.[5] The resulting solution temperatures from localized heating are reproduced in Figure 2.1 where different concentrations of aqueous Ge-NC colloidal solutions are irradiated using the NIR laser.

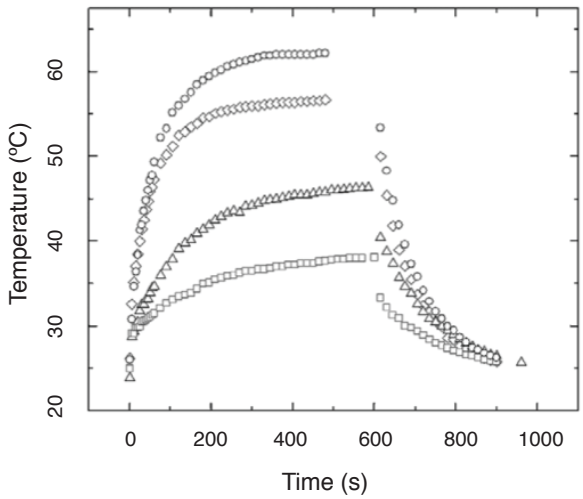

Figure 2.1: Ge-NC aqueous colloidal solutions irradiated with a Ti:sapphire NIR laser showing increased temperature with increasing NC concentrations (reproduced from reference 5)

Direct band-gap semiconductor nanostructures have also been shown to produce a PT effect. Hessel *et al.* determined the photothermal efficiency for the aqueous dispersions of CuSe-NCs to be 22% under 800 nm excitation.[6]

2.1.2. Metal Nanostructures Exhibiting Photothermal Effects

The early fundamental studies of PT effects focused on semiconductors, studying the concept of heat dissipation from materials due to excitation of an electron.[1] Researchers have since explored a variety of metallic materials which offer the benefit of enhanced absorption cross-sections. These materials (to name a few) include carbon nanotubes,[11] Pd-nanosheets,[9] and a variety of Au and Ag nanostructures.[7, 8, 12, 13, 14] Due to the enhanced and tunable surface plasmon resonance exhibited within Au nanostructures, they have been viewed as ideal candidates for studying photothermal effects.[7] The PT effect has been studied for a wide variety of Au nanostructures including Au-NPs,[15] NRs,[16] nanoshells,

nanopyramids,[17] and nanocages.[12] Au-NRs have been determined to have the highest PT efficiencies under NIR irradiation (the ideal spectral region for biological applications due to the transparency of tissue, blood and water).[18]

2.1.3. Photothermal Therapy

Using heat to treat cancer has existed and evolved through many decades. Introducing heat to infectious areas has grown from using a cauterizing iron in the 1600's,[19] to using ultrasonic waves to induce hyperthermia.[20, 21] The outstanding challenge in effectively employing this therapeutic approach is inducing heat selectively to tumor tissues without significant damage to healthy tissue. Another tumor therapy method is photodynamic therapy (PDT), commonly referred to as photochemotherapy. This method causes cell destruction based on singlet oxygen or free radicals formed during a photochemical process. In general, a photosensitizer is administered intravenously, given several days to accumulate in the tumor tissue, and then the targeted volume is irradiated with visible light.[22] One major disadvantage of PDT is that the administered photosensitizer tends to remain in the body for extended periods of time making patients highly sensitive to light.[8]

Photothermal therapy (PTT) is an alternative to PDT where photothermal agents are employed for their localized heating leading to local cell or tissue destruction.[8] PTT using metal nanostructures such as Au has the advantage of being able to use NIR radiation as a source to penetrate deep into the tissue for treatment of deep-seeded tumors.[7] Preliminary studies indicated using Au-NRs as

PTT agents could result in localized heating causing cell damage to both healthy and cancerous cells, but only cancerous cells were damaged with lower heating effects that could be controlled by the irradiation power.[8] Although toxicological evaluations are required before these materials can be used for therapeutic cancer treatment, these proof-of-concept experiments indicate that these nanostructures are promising candidates for relatively mild cancer treatment.

2.1.4. Photothermal Effect of Silicon Nanocrystals

The PT effects observed for different semiconducting and metallic nanostructures provide motivation for the work reported in this chapter. Au-NRs and Au-nanoshells have been the most widely studied for use as a PTT agent, however there are certain disadvantages associated with these nanostructures. The first is their size. In order to enhance the blood-assisted circulation in the body, nanostructures should be within the range of 5-50 nm.[23,24] Au-nanoshells have particle sizes typically ranging from 100-200 nm[8] and of the Au-NRs studied for PT effects, the smallest fall onto the cusp of this upper bound.[7] The second disadvantage is the cytotoxicity of CTAB (cetyltrimethylammonium bromide), the surfactant used as a stabilizing agent for Au-NRs.[25] In order to utilize a material as a PTT agent it is vital the material be non-toxic.

Nanostructured Si has been shown to be non-toxic. This was shown by Park *et al.* for p-Si where biodegradation was observed to form silicic acid ($Si(OH)_4$), which is effectively excreted from the human body through urine.[26] Erogbogbo *et al.* demonstrated the non-toxicity of Si-NCs by studying cell

survival, showing cell survival greater than 60% at 0.5 mg/mL Si-NC concentrations.[27] Since Si-NCs are non-toxic and NCs formed from HSQ are in the appropriate size regime, these materials make a good candidate for the potential use as a PTT agent.

As mentioned in section 2.1.1., PT effects have been observed for solutions of Ge-NCs and p-Si, however, the exact mechanism of heating is unclear and the impact of NC size has not been explicitly evaluated. This chapter is set out to study the PT effects in Si-NCs as a function of size, defect concentration, and irradiation wavelength in order to propose a mechanism of heating and evaluate these materials as possible PTT agents.

2.2 Materials and Methods

2.2.1. Reagents and Materials

Hydrogen silisesquioxane (HSQ) was obtained from Dow Corning under the tradename FOx® as a solution in methyl isobutyl ketone (MIBK). Electronic grade hydrofluoric acid (49% $HF_{(aq)}$, J.T. Baker), reagent grades of toluene, chloroform, hydrochloric acid, ethanol and methanol were obtained from Sigma Aldrich and used as received. 1-dodecene, also purchased from Sigma Aldrich, was filtered through activated alumina to remove any peroxide impurities immediately before use.

2.2.2. Preparation of Silicon Nanocrystal Composite with NCs *ca.* 4 nm in size

To prepare a composite of Si-NCs embedded within an oxide matrix an established literature procedure was followed.[28] In brief, the MIBK solvent was removed, *in vacuo*, from the FOx® solution leaving a white powder of HSQ. This HSQ solid was heated to 1100°C for 1 hour under a reducing atmosphere of 5% H_2/ 95% Ar in a quartz boat within a tube furnace. The resulting solid was a dark brown composite made up of Si-NCs (*ca.* 4 nm) embedded within a silica (SiO_2) matrix. This composite was ground to a fine powder using a mortar and pestle.

2.2.3. Preparation of Si-NC composite with NCs *ca.* 6 nm and 9 nm in size

Si-NCs of sizes larger than 4 nm can be prepared within the oxide matrix by thermally processing the composite described above at higher temperatures before grinding the composite. The as prepared composite was placed into a carbon boat following which was placed in a high temperature tube furnace. The composite was then processed at either 1200°C (6 nm NCs) or 1300°C (9 nm NCs) for one hour under flowing Argon. The resulting composite was then ground up using a mortar and pestle.

2.2.4. Liberation of Si-NCs

In order to functionalize the Si-NCs with an alkyl surface group, NCs must first be liberated from the oxide matrix. For a typical liberation, approximately 2 g of composite was transferred to a Teflon® beaker. To this, 1 mL of HCl (12 M)

and 30 mL of HF (25 M) were added to the composite and stirred, creating a dark brown, cloudy mixture. After 5 minutes, 10 mL of ethanol (EtOH) was added. After an additional 5 minutes, hydride terminated Si-NCs were extracted from the aqueous layer using three 20 mL toluene extractions, leaving behind a colourless transparent aqueous solution. All remaining HF was neutralized using a saturated solution of calcium chloride. The dark brown toluene/ Si-NC extracts were placed into glass test tubes and centrifuged using a low speed centrifuge for 5 minutes. After centrifugation, the toluene supernatant was decanted leaving a precipitate of hydride terminated Si-NCs.

2.2.5. Functionalization of Silicon Nanocrystals

To functionalize the hydride terminated Si-NCs literature methods for hydrosilylation were followed.[29,30] The hydride terminated Si-NC precipitate was re-dispersed in 50 mL of 1-dodecene, and transferred into an oven dried Schenk flask, yielding a brown cloudy solution. The reaction mixture was degassed using three vacuum pump cycles and maintained under an argon atmosphere. The flask was placed in a silicone oil bath and heated to 190°C overnight (or >3 hours) to induce thermal hydrosilylation of the terminal alkene. The resulting product mixture was a transparent orange-brown solution, indicating colloidal stability and successful functionalization of dodecyl ligands onto the Si-NC surface.

The reaction mixture was placed into four 50 mL PTFE centrifuge tubes, filling the tubes about a quarter full. NCs were precipitated using a 3:1 mixture of EtOH:MeOH. Particles were centrifuged at 14 000 rpm for 20 min using a

Beckman J2-21 high speed centrifuge, followed by decanting the supernatant. Three centrifugation wash cycles were performed using chloroform to re-disperse the precipitate and MeOH to precipitate NCs. After the final wash, the precipitated Si-NCs were dispersed in toluene, filtered through a hydrophobic PTFE filter, and stored in a vial until further use.

2.2.6. Photothermal Data Collection

To measure the photothermal effect of colloidal Si-NCs, a PTFE coated K-type thermocouple, with data-logger (Teletemp Corporation), was used to monitor temperature changes. 1.96 g of a Si-NC toluene solution, was placed in a quartz cuvette, capped, stirred and irradiated with laser line of choice (for most of the experiments, the 514 nm line of the argon laser was chosen). Irradiation was carried out using a Coherent Innova 90C argon ion laser (for section 2.3.2. a Millenia diode-pumped solid-state visible continuous wave 532 nm laser was used). The thermocouple was placed through the cap and into the solution held in a marked location. Each measurement was repeated a minimum of nine times as the observed heating effect could vary significantly due to slight differences in stirring rate, nearby ventilation, etc. Figure 2.2 shows a picture of the experimental set-up.

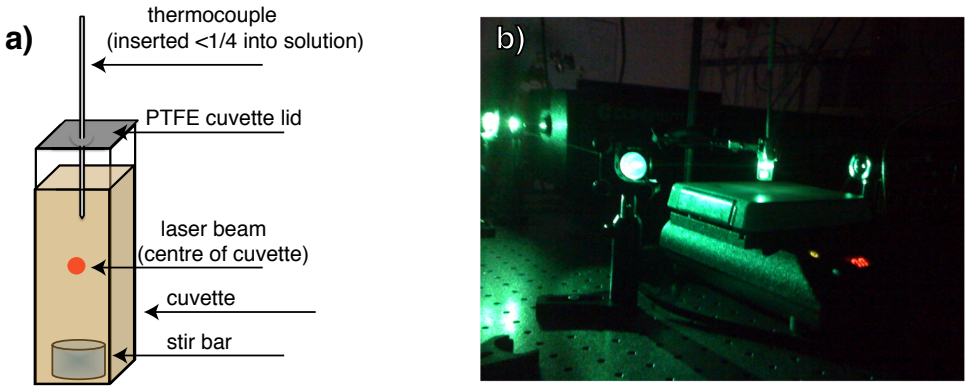

Figure 2.2: Photothermal experimental set-up a) schematic of cuvette b) laser irradiation of NP solution

2.2.7. Photoluminescence Data Collection

PL spectra were obtained by irradiation of a glass vial, containing the sample solution, with a 325 nm line of a He-Cd laser. Emitted photons were collected with a fiber optic connected to an Ocean Optics USB2000 spectrometer. The spectrometer spectral response was normalized using a black body radiator.

2.2.8. Dynamic Light Scattering

DLS measurements were made using a Malvern, Zetasizer Nano-ZS instrument with a built-in 633 nm laser. Zetasizer 2.0 software was used for analysis. Dilute solutions of Si-NCs in toluene were analyzed using a quartz cuvette.

2.3 Results and Discussion

2.3.1. Will Silicon Nanocrystals Exhibit a Photothermal Effect?

At first inspection, a literature precedent for the PT effect exhibited within indirect semiconducting nanostructures is evident.[4,5,10] This precedent leads to the

natural expectation that Si-NCs would similarly exhibit a PT effect. However, comparing the light absorption of nanostructured silicon to nanostructured gold it seems, Si-NCs are approximately one hundred thousand times less efficient than Au-NRs at absorbing incident light. This is likely due to silicon's indirect band-gap nature.

This relation can be readily estimated by performing a "back-of-the-envelope" type calculation comparing the light absorption in Au-NRs to Si-NCs. A study by Beard *et al.* shows the absorption cross-section for different Si-NC sizes,[31] reporting approximate values of:

$$\sigma = 1 \times 10^{-16} cm^2 \text{ for 3.8 nm Si-NCs and}$$
$$\sigma = 5 \times 10^{-15} cm^2 \text{ for 9.5 nm Si-NCs.}$$

Where σ is the absorption cross-section. Au-NRs with an aspect ratio of 3.3, have been reported to have an approximate molar extinction coefficient of:

$\varepsilon = 4 \times 10^{9} M^{-1} cm^{-1}$ for Au-NRs 15 nm in diameter and 50 nm in length.

Where ε is the molar extinction coefficient.

By performing a simple conversion using the following relationship (describing the transformation of absorption cross-sections to molar extinction coefficients):[32]

$$\sigma = 2.303 \times \frac{1000}{N_A} \varepsilon$$

leads to molar extinction values of:

$$\varepsilon = 2.6 \times 10^{4} M^{-1} cm^{-1} \text{ for 3.8 nm Si-NCs and}$$
$$\varepsilon = 1.3 \times 10^{6} M^{-1} cm^{-1} \text{ for 9.5 nm Si-NCs.}$$

Comparing Si-NCs extinction coefficients with Au-NRs, it is apparent that Au-NRs absorb light *ca.* 100,000 times better than 3.8 nm Si-NCs and *ca.* 1000 times more effectively that 9.5 nm Si-NCs.

This "back-of-the-envelope" type calculation is an indication of one of two things. Either the PT effect will not be observable in a colloidal solution of Si-NCs, or that higher concentrations than those used for Au-NRs will be required to achieve a pronounced PT effect from colloidal Si-NCs.

2.3.2. A First Attempt to Measure the Photothermal Effect for Si-NCs

After comparing the light absorption of Si-NCs and Au-NRs, an observable PT effect from Si-NCs seemed unlikely. However, upon irradiation of 2 g of a toluene/ Si-NC solution it was found that Si-NCs had a profound PT effect upon irradiation with a 532 nm laser with a power of 1 W. Figure 2.3 shows the change in temperature of different concentrations of Si-NCs 4 nm in size passivated with a dodecane alkyl chain and dispersed into toluene. As the NC concentration increases by 4 mg/mL a temperature increase of 4°C to 30°C with respect to increasing concentration was observed in the NC solution. Based upon the "back-of-the-envelope" estimate noted above, this observation was an unexpected result. It is important to note the change in temperature of blank toluene was monitored during irradiation and was negligible even after 30 min. of irradiation.

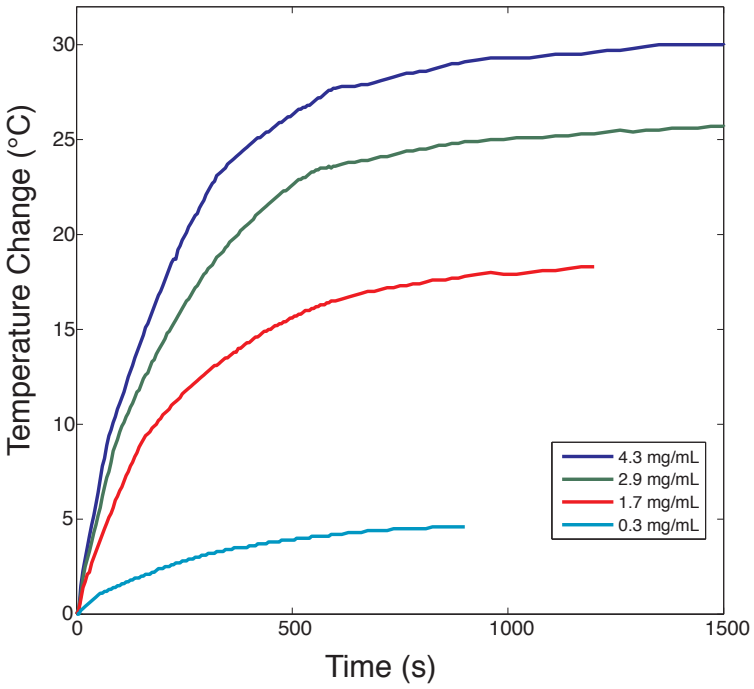

Figure 2.3: Photothermal effects observed from different concentrations of Si-NCs upon irradiation of a NC/ toluene solution with 1 W of 532 nm light

The astounding PT effects observed for colloidal solutions of Si-NCs in toluene led to results comparable to the report by Chen *et al.* where PT efficiencies were calculated from their experimental results.[7] The natural progression of PT studies of Si-NCs was to quantify these PT efficiencies of Si as a comparison.

2.3.3. Calculating Photothermal Efficiencies

Photothermal (PT) efficiencies were calculated using the method reported by Wang *et al.*[7] This model is based upon an energy balance of a colloidal nanoparticle (NP) solution during the photothermal heating process.[7] The following is a brief summary of the mathematical model provided by Wang *et al.*

The energy balance equation for a colloidal NP solution can be expressed as:

$$(m_s c_{p,s} + m_c c_{p,c}) \frac{d\Delta T}{dt} = Q_{laser} - Q_{loss}$$

Where m_s is the mass of the solution, $c_{p,s}$ is the constant-pressure heat capacity of the solution (in our case taken as the constant-pressure heat capacity of the solvent $c_{p,s}$=1.125 J•g^{-1}•K^{-1}),[33] m_c is the mass of the quartz cuvette, $c_{p,c}$ is the constant-pressure heat capacity of quartz (literature value $c_{p,c}$=0.839J·g^{-1}·K^{-1}), ΔT is the temperature change of the solution at a specified time interval, Q_{laser} is the energy of the system as a result of laser irradiation, and Q_{loss} is the energy dissipated from the system.

The contributions to Q_{laser} include absorption of light from the particles in solution and the cuvette and can be represented as:

$$Q_{laser} = I(1-\xi)(1-10^{-E_\lambda})\eta + I\xi$$

Here, I is the reflection corrected laser power, ξ is the absorption of the cuvette and solvent, E_λ is the absorbance value of the NC solution at the particular irradiation wavelength, and η is the photothermal efficiency.

The heat dissipated is approximated using the first two terms of a Taylor series expansion:

$$Q_{loss} = B\Delta T + C(\Delta T)^2$$

Where B and C are coefficients. Using these heat representations in the energy balance equation:

$$(m_s c_{p,s} + m_c c_{p,c}) \frac{d\Delta T}{dt} = I(1-\xi)(1-10^{-E_\lambda})\eta + I\xi - B\Delta T - C(\Delta T)^2$$

In order to solve for the unknown variables, *B* and *C*, the temperature decay was monitored after the laser was switched off, making Q_{laser} equal to zero, reducing the energy balance equation to:

$$J\frac{d\Delta T}{dt} = -B\Delta T - C(\Delta T)^2$$

Where *J* is a constant representing the mass and heat capacity parameters. This energy balance equation can be respresented as a first-order non-linear ordinary differential equation of the form:

$$J \cdot y'(t) + B \cdot y(t) + C \cdot (y(t))^2 = 0$$

Solving this differential equation to find *y(t)* we find:

$$y(t) = -\frac{Be^{B \cdot C_1}}{Ce^{B \cdot C_1} - Be^{B \cdot t / J}}$$

Where C_1 is an integration constant.

After the laser shutter was closed the temperature decay was monitored and fit to an equation of the form of *y(t)* to solve for parameters B and C (Data fitting was performed using MATLAB).

In order to solve for ξ, replacing colloidal nanoparticle solution with just the solvent reduces the energy balance equation to:

$$J\frac{d\Delta T}{dt} = I\xi - B\Delta T - C\Delta T$$

When the temperature increase reaches a steady state the temperature differential becomes zero and one can solve for ξ.

The variables are all known and one can solve for the photothermal efficiency by considering the steady state of the temperature rise for the colloidal solution:

$$\eta = \frac{B \cdot \Delta T_s + C \cdot (\Delta T_s)^2 - I\zeta}{I(1-\zeta)(1-10^{-E_\lambda})}$$

Note, the value for ζ was taken to be zero as no apparent temperature change was observed for a toluene blank.

2.3.4. Photothermal Effect of 4 nm sized Silicon Nanocrystals

When Si-NCs were irradiated with 250 mW of power from a 514 nm line of an argon laser, a temperature increase is observed which reaches a steady state after 30 min. of irradiation. By fitting the temperature decay as stated in 2.3.3. a PT efficiency can be determined.

Figure 2.4 shows the PT data and decay fits collected for three samples of 4 nm Si-NCs at different toluene dilutions. Samples were diluted to have an absorbance of 1.5, 1.2, and 0.8 at 514 nm and compared to determine an average PT efficiency of 57.8%. Table 2.1 summarizes the data that was used to determine an average PT efficiency of 57.8%. Based upon these calculations, 57.8% of absorbed light is effectively dissipated as heat to the surrounding environment.

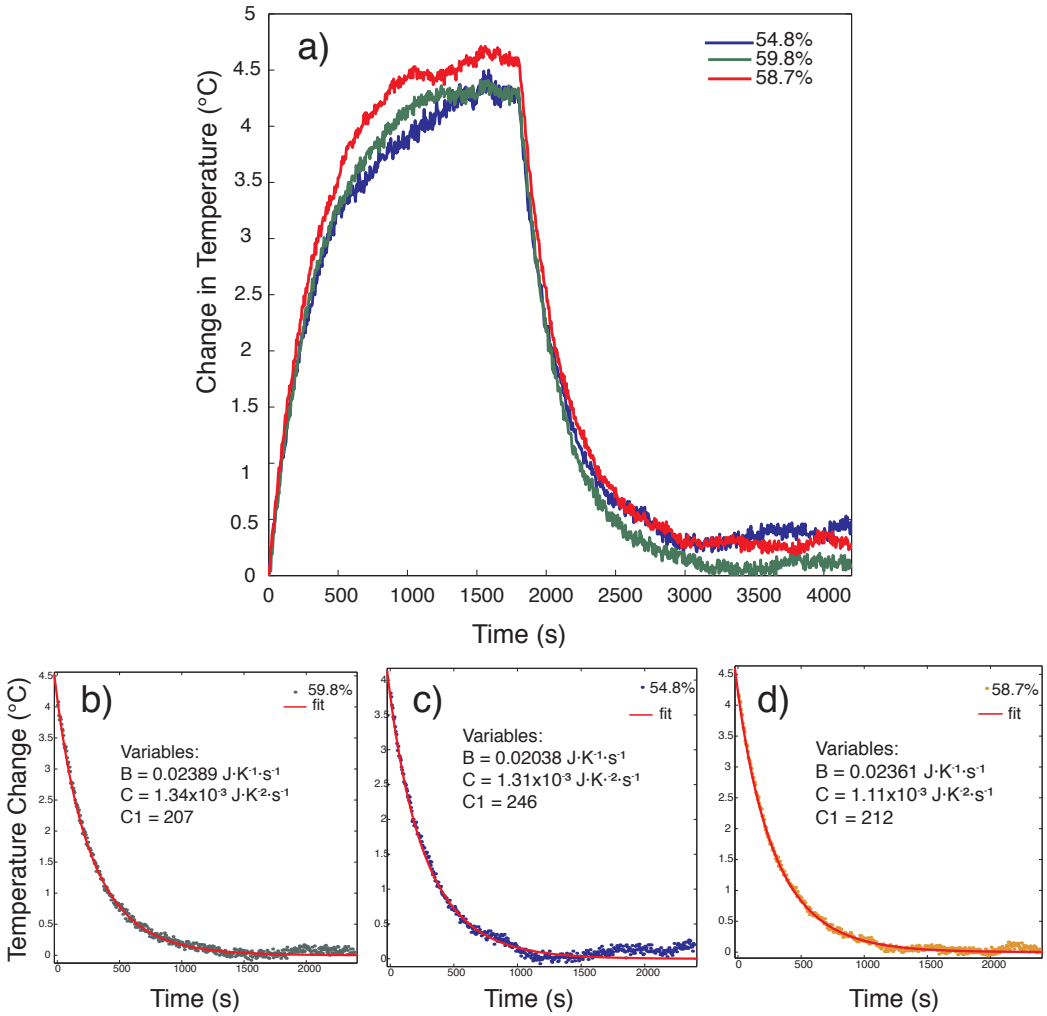

Figure 2.4: Observed PT effect for 4 nm Si-NCs a) Temperature increase and decay for three different NC concentrations, b)-d) respective decay fits used to determine respective PT efficiencies

Table 2.1: Tabulated variables used for calculation of PT efficiency for 4 nm Si-NCs

Absorbance at 514 nm	**Variable B ($J \cdot K^{-1} \cdot s^{-1}$)**	**Variable C ($J \cdot K^{-2} \cdot s^{-1}$)**	**Constant C_1**	**PT efficiency (η)**
1.5	0.02361	1.11×10^{-3}	212	58.7%
1.2	0.02389	1.34×10^{-3}	207	59.8%
0.8	0.02038	1.31×10^{-3}	246	54.8%
			Average η	**57.8%**

Si-NCs are often believed to be ridden with defects.[34] These defects can act as non-radiative decay channels, reducing photoluminescent quantum yields (QYs). Typical Si-NC QYs reported range from *ca.* 1-60%, with the majority around 5-20%. [31, 35, 36] From this PT analysis of 4 nm Si-NCs it is unclear whether this effect is from non-radiative decay due to defects or carrier cooling in the form of phonons from the relaxation of an electron to the conduction band minimum before recombination. Studies outlined in the following sections aim at investigating these effects.

2.3.5. Size Dependence of the Photothermal Effect

As discussed in Chapter 1 section 1.6.5, processing the Si-NC/oxide composite at temperatures greater than 1100°C yield larger Si-NCs. By processing at 1200°C and 1300°C, Si-NCs approximately 6 nm and 9 nm in size, respectively, are obtained. This increase in size, leads to a red-shift in the photoluminescence (PL) due to quantum confinement (Chapter 1 section 1.4). This apparent red-shift can be observed in Figure 2.5. The PL maxima observed are approximately at *ca.* 785 nm, 900 nm, and 965 nm for 4 nm, 6 nm, and 9 nm NCs respectively.

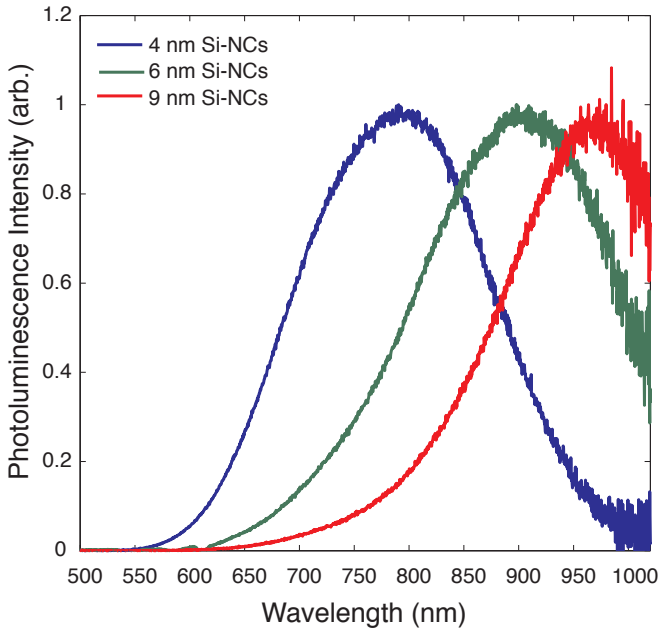

Figure 2.5: Photoluminescence of dodecyl functionalized Si-NCs in toluene 4 nm (blue), 6 nm (green), and 9 nm (red) in size

To measure NC sizes in solution, dynamic light scattering was used (Figure 2.6). Dynamic light scattering (DLS) is a technique capable of measuring particle size in solution based on the time-dependant fluctuation of scattering intensity from an incoming laser. While this technique, is not a tool to be used stand-alone for size analysis, it is an agreement with sizes previously reported for Si-NCs prepared by this method, and is an effective tool for observing size trends.[37] A similar trend in size is observed using DLS consistent with PL shifting and quantum confinement of Si-NCs. These sizes (shown in Figure 2.6) are in agreement with those listed by Hessel *et al.* which were measured using X-ray diffraction.

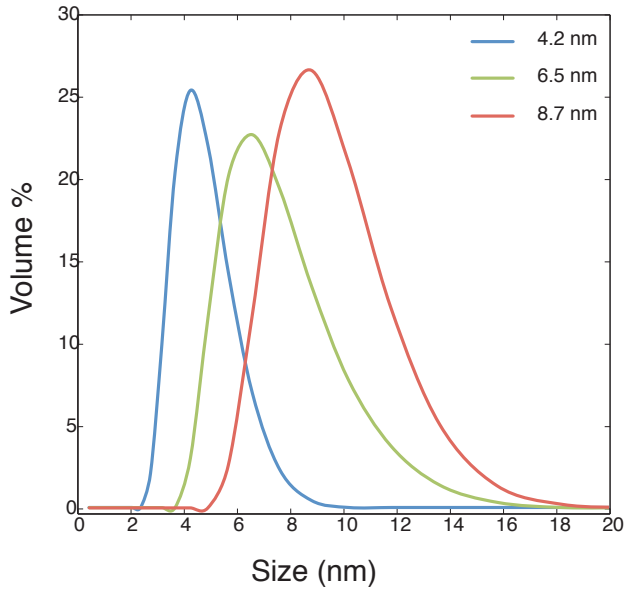

Figure 2.6: DLS measurements showing respective sizes for different dodecyl functionalized Si-NCs in toluene

These size analyses show the correlation between Si-NC sizes and their optical properties. Since the PT effect of Si-NCs is hypothesized to be due to either non-radiative exciton recombination from defects or from carrier cooling, both of these postulates should result in an enhanced PT effect from larger Si-NCs. Defects are expected to scale with surface area and volume of a NCs, leading to an enhanced PT effect if the process is in fact defect mediated.[38] A greater effect from carrier cooling should also be experienced by a larger NC due to the decrease in the energy band-gap due to quantum confinement.

A comparison of the PT effect of *ca.* 6 nm and 9 nm Si-NCs to that of 4 nm Si-NCs indicated an enhanced PT effect was observed with increased NC size. Figure 2.7 and Table 2.2 show the PT data and tabulated results for Si-NCs approximately 6 nm in size. These results show that 6 nm Si-NCs have an average PT efficiency of 68.3% (i.e., just over 10% increase from 4 nm Si-NCs). Figure

2.8 and Table 2.3 show the PT data and tabulated results for 9 nm Si-NCs. These results show that these larger NCs have an average PT efficiency of 74.7%, just over 15% greater than that obtained for the 4 nm NCs, and just over 5% greater than the 6 nm NCs.

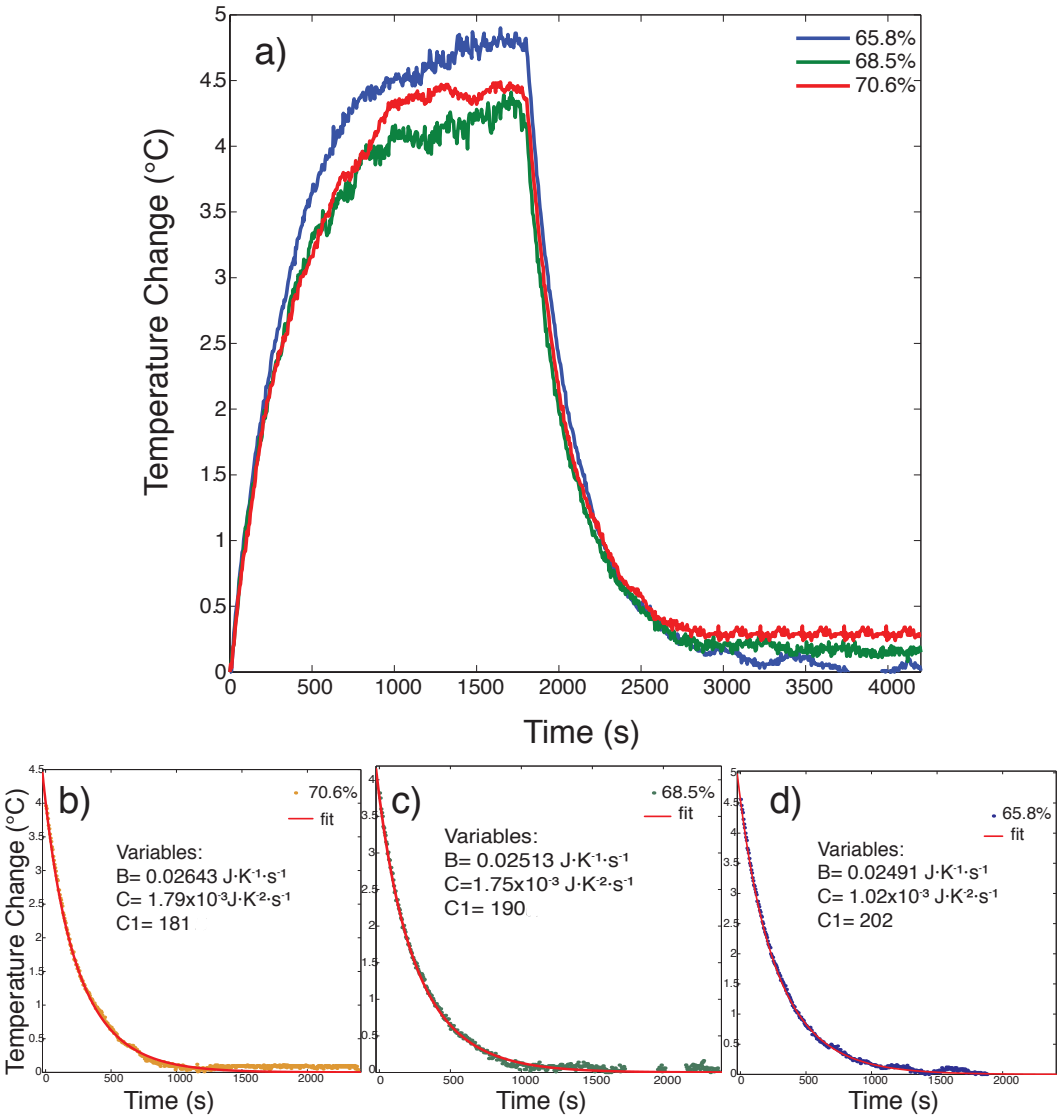

Figure 2.7: Observed PT effect for 6 nm Si-NCs a) Temperature increase and decay for three different NC concentrations, b)-d) respective decay fits used to determine respective PT efficiencies

Table 2.2: Tabulated variables used for calculation of PT efficiency for 6 nm Si-NCs

Absorbance at 514 nm	**Variable B ($J \cdot K^{-1} \cdot s^{-1}$)**	**Variable C ($J \cdot K^{-2} \cdot s^{-1}$)**	**Constant C_1**	**PT efficiency (η)**
1.5	0.02491	1.02×10^{-3}	202	65.8%
1.2	0.02643	1.79×10^{-3}	181	70.6%
0.9	0.02513	1.75×10^{-3}	190	68.5%
			Average η	**68.3%**

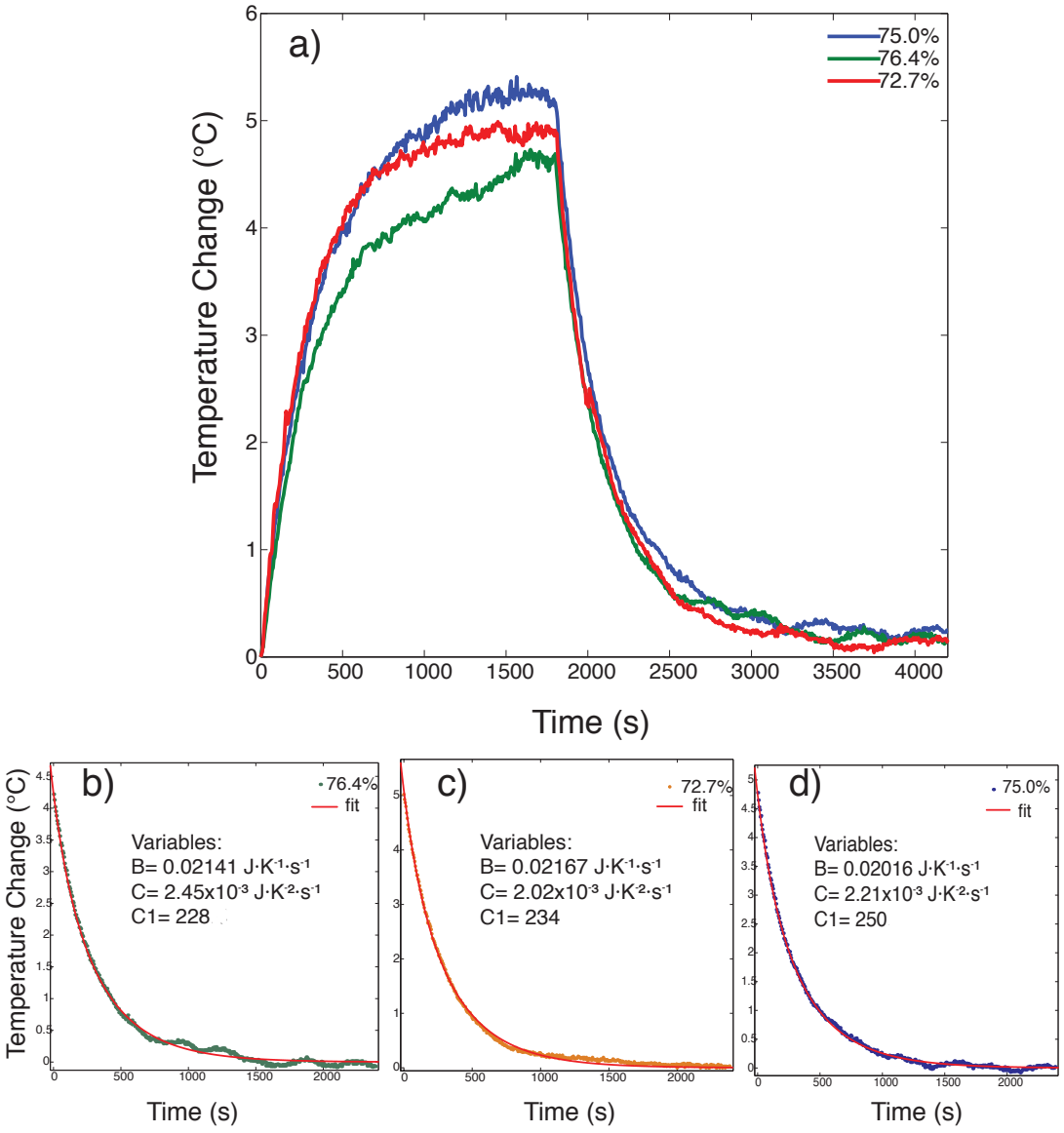

Figure 2.8: Observed PT effect for 9 nm Si-NCs a) Temperature increase and decay for three different NC concentrations, b)-d) respective decay fits used to determine respective PT efficiencies

Table 2.3: Tabulated variables used for calculation of PT efficiency for 9 nm Si-NCs

Absorbance at 514 nm	**Variable B ($J \cdot K^{-1} \cdot s^{-1}$)**	**Variable C ($J \cdot K^{-2} \cdot s^{-1}$)**	**Constant C_1**	**PT efficiency (η)**
1.5	0.02016	2.21×10^{-3}	229	75.0%
1.2	0.02167	2.02×10^{-3}	234	72.7%
0.9	0.02141	2.45×10^{-3}	228	75.0%
			Average η	**74.7%**

The PT results reported here indicate larger Si-NCs exhibit a more pronounced PT effect. These findings are particularly interesting because the larger NCs have emission in the NIR region (i.e., the spectral region where the tissue is transparent), and begin to absorb longer wavelength photons. These results hold promise for larger Si-NCs being employed as PTT agents. These results however, do not provide insight into the mechanism by which the PT effect is achieved. One way to study this is to observe the behaviour for NCs that have been subjected to longer thermal processing times. In principle prolonged heating should remove defects via annealing.

2.3.6. Photothermal Effects of Si-NCs after Prolonged Thermal Processing

Hessel *et al.* report that thermal processing of HSQ for extended periods of time caused a red-shift in PL without inducing a change in the NC size distribution.[37] Because there was no change in particle size, the observed red-shift clearly did not arise as a result of quantum confinement and was attributed to the enhancement of PL from larger NCs due to defect passivation.[37] The observed change in PL can be observed in Figure 2.9 showing dodecyl functionalized Si-NCs from thermal processing of HSQ at 1100°C for 1 hour (blue trace) and 24 hours (green trace). The PL maxima are red-shifted from approximately *ca.* 760 nm to *ca.* 925 nm.

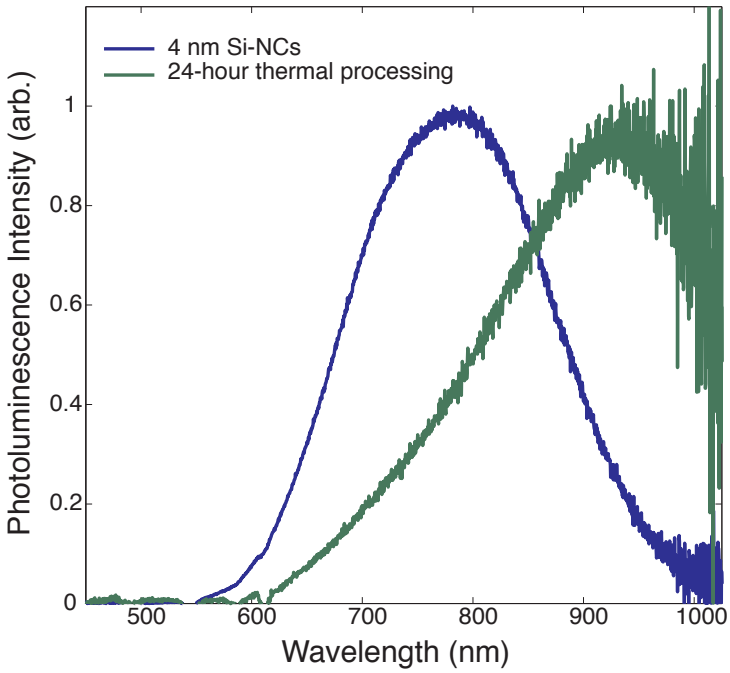

Figure 2.9: Photoluminescence of 4-nm Si-NCs thermally processed at 1100°C for one hour (blue) and 24 hours (green)

Figure 2.10 shows the DLS data collected for the two dodecene functionalized Si-NCs derived from different HSQ thermal processing times. While from DLS, there is a slight shift in the NC size from 4.2 nm to 5.1 nm, this size change is within the detection limits of the method and is not great enough to account for the large observed PL red-shift. In this regard, the large red-shift in the alkyl functionalized Si-NCs processed for 24 hours is thus attributed to defect passivation.

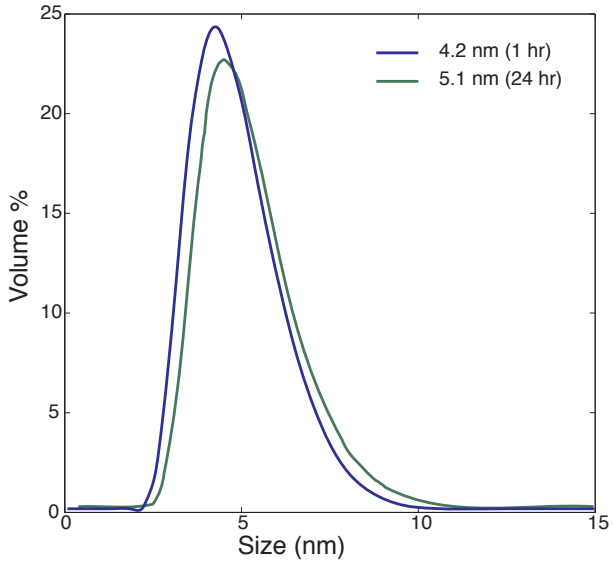

Figure 2.10: DLS of 4-nm Si-NCs thermally processed at 1100°C for one hour (blue) and 24 hours (green)

To determine if the PT effect is mediated by non-radiative recombination due to present defects, the PT effects can be observed for samples after prolonged thermal processing in order to remove defects. It is expected that if PT effects are dominated by defects, samples formed from prolonged thermal processing should result in a diminished PT efficiency. The PT effects observed for defect minimized NCs are depicted in Figure 2.11 and tabulated in Table 2.4. These results show that Si-NCs with minimized defects result in a PT efficiency of 58.0% which is extremely similar to that noted for Si-NCs formed by thermally processing HSQ for 1 hour (i.e., 57.8%).

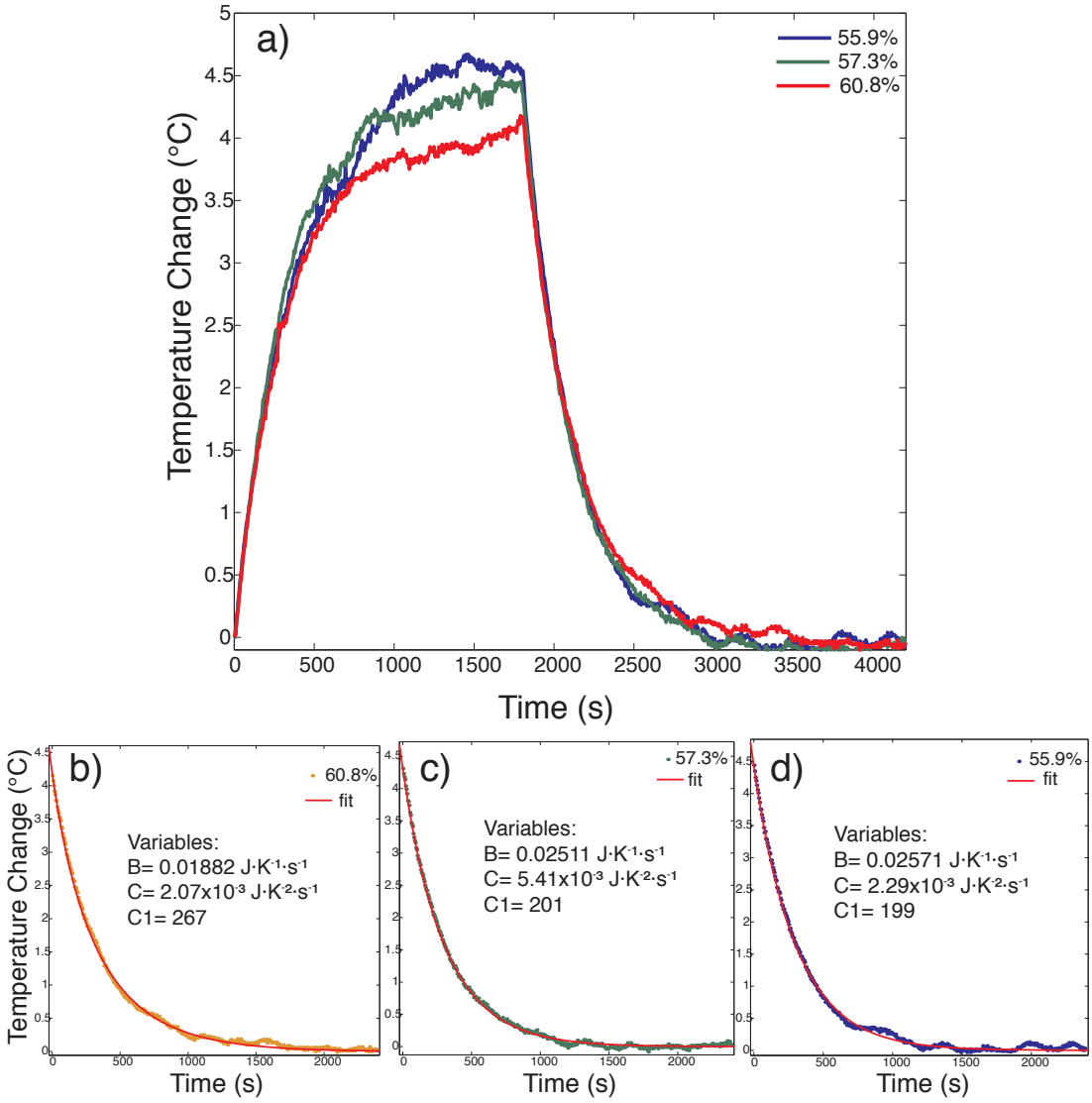

Figure 2.11: Observed PT effect for 4 nm Si-NCs after prolonged thermal processing a) Temperature increase and decay for three different NC concentrations, b)-d) respective decay fits used to determine respective PT efficiencies

Table 2.4: Tabulated variables used for calculation of PT efficiency for 4 nm Si-NCs after prolonged thermal processing

Absorbance at 514 nm	**Variable B ($J \cdot K^{-1} \cdot s^{-1}$)**	**Variable C ($J \cdot K^{-2} \cdot s^{-1}$)**	**Constant C_1**	**PT efficiency (η)**
1.5	0.02571	2.07×10^{-3}	267	55.9%
1.2	0.02511	5.41×10^{-3}	201	57.3%
0.8	0.01882	2.07×10^{-3}	199	60.8%
			Average η	**58.0%**

These results indicate the PT effect in Si-NCs is likely not mediated by defects in the NC leaving the alternative hypothesis of carrier cooling of electrons from relaxation to the conduction band minimum the likely explanation. One way to study this hypothesis is to study the PT effects using the same NC samples with different irradiation wavelengths. Higher energy irradiation should result in higher PT efficiencies.

2.3.7. Photothermal Effect of 4 nm Si-NCs using a 488 nm line of Irradiation

As stated earlier, higher energy irradiation of Si-NCs, should cause an increase in the PT efficiency if carrier cooling is responsible for the PT effect. A schematic of carrier cooling is shown in Figure 2.12. This was investigated using the 488 nm line of the same argon laser. Although this line is not significantly higher in energy than the 514 nm line used in prior studies, it is reasonable the energy difference will be large enough to cause an increase in the PT efficiency because there is an exponential increase in absorbance with visible photon energy.[39]

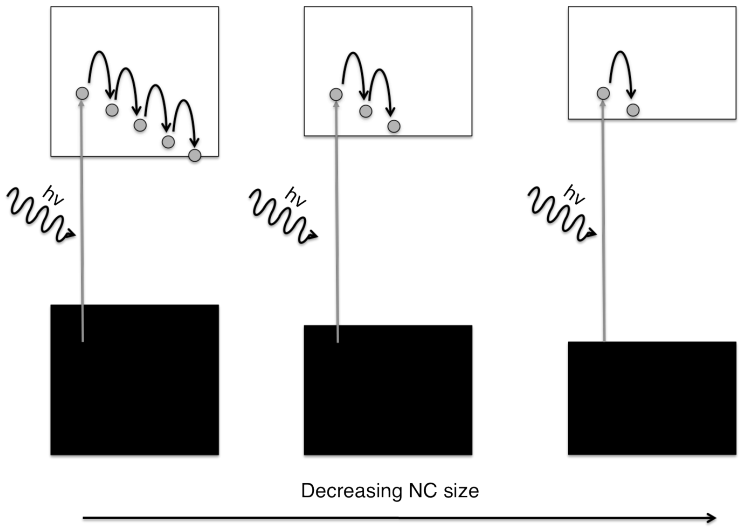

Figure 2.12: Schematic of the degree of carrier cooling for different NC sizes

Figure 2.13 and Table 2.5 show the PT data collected for the irradiation of 4 nm Si-NCs using the 488 nm line of an argon laser. From these results an average PT efficiency of 63.8% is obtained for the higher energy irradiation. An approximate 6% PT efficiency increase is observed when compared with the 514 nm line (Figure 2.4), where an average efficiency of 57.8% is obtained. Although this efficiency it not substantially higher, it does indicate increasing the irradiation energy for Si-NCs causes an increase in the PT efficiency.

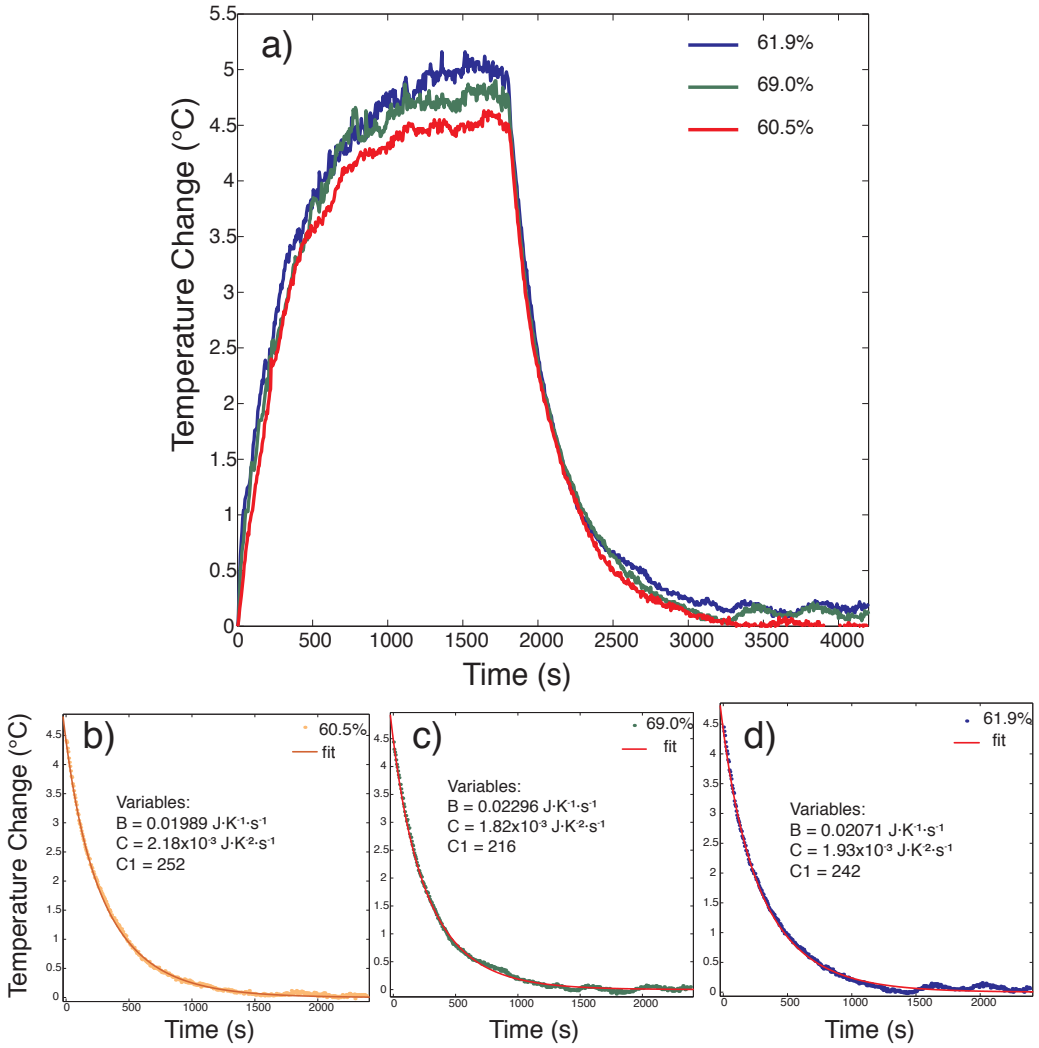

Figure 2.13: Observed PT effect for 4 nm Si-NCs using higher energy irradiation a) Temperature increase and decay for three different NC concentrations, b)-d) respective decay fits used to determine respective PT efficiencies

Table 2.5: Tabulated variables used for calculation of PT efficiency for 4 nm Si-NCs using higher energy irradiation

Absorbance at 488 nm	**Variable B ($J \cdot K^{-1} \cdot s^{-1}$)**	**Variable C ($J \cdot K^{-2} \cdot s^{-1}$)**	**Constant C_1**	**PT efficiency (η)**
2.5	0.02071	1.93×10^{-3}	242	61.9%
1.9	0.02296	1.82×10^{-3}	216	69.0%
1.4	0.01986	2.18×10^{-3}	252	60.5%
			Average η	**63.8%**

These results lead us to propose that the mechanism by which the PT effect occurs in Si-NCs is due to carrier cooling, releasing heat in the form of phonons, upon electron (or hole) relaxation to the conduction band minimum (or valence band maximum).

2.4 Conclusion

This chapter presented a study for the PT effect of Si-NCs. Upon irradiation with a high power laser (1W), temperature changes in solution of up to 30°C were observed. This behaviour was quantified by PT efficiencies, and average efficiencies of 57.8%, 68.3%, and 74.7% were found for Si-NCs 4 nm, 6 nm, and 9 nm in diameter, respectively. Two mechanisms were proposed to account for the effect, and using a different energy laser line it was determined the observed PT effect was dominant due to carrier cooling from the relaxation of an excited electron to the conduction band minimum in the form of phonons.

For bulk systems, the PT effect is presumed to arise from the diffusion of electron/ hole pairs, diffusing to regions of lower carrier concentration, contributing to the thermal conductivity of the lattice and causing localized heating. This is not reasonable for the present system because the dimension of the Si-NC materials investigated here approach the Bohr exciton radius (i.e., 4.3 nm),[40] hence carrier diffusion is unlikely.

The present studies have raised the possibility of using Si-NCs as PTT agents. Further investigation of the PT properties using NIR radiation will determine if these particles will be practical for PTT. The PT properties of water-

soluble NCs is another area of study which will give insight into possible PTT applications. Although Si-NCs are about one hundred thousand times poorer at absorbing light then Au-NRs, their observed effect is significant, offering heat tunability with concentration and optical tunablity across the visible and NIR spectrum with size.

2.5 References

1. Gärtner, W.W., *Phys. Rev.* **1961**, 122 (2), 419-424.
2. Gordon, J.P.; Leite, R.C.C.; Moore, R.S.; Porto, S.P.S.; Whinnery, J.R., *J. Appl. Phys.* **1965**, 36 (1), 3-8.
3. Chen, W.R.; Adams, R.L.; Heaton, S.; Dickey, D.T.; Bartels, K.E.; Nordquist, R.E., *Cancer Lett.* **1995**, 88 (1), 15-19.
4. Wang, N.; Yao, B.D.; Chan, Y.F.; Zhang, X.Y., *Nano Lett.* **2003**, 3 (4), 475-477.
5. Lambert, T.N.; Andrews, N.L.; Gerung, H.; Boyle, T.J.; Oliver, J.M.; Wilson, B.S.; Han, S.M., *Small*, **2007**, 3 (4), 691-699.
6. Hessel, C.M.; Pattani, V.P.; Rasch, M.; Panthani, M.G.; Koo, B.; Tunnell, J.W.; Korgel, B.A., *Nano Lett.* **2011**, 11 (6), 2560-2566.
7. Chen, H.; Shao, L.; Ming, T.; Sun, Z.; Zhao, C.; Yang, B.; Wang, J., *Small*, **2010**, 6 (20), 2272-2280.
8. Huang, X.; Jain, P.K.; El-Sayed, I.H.; El-Sayed, M.A., *Lasers Med. Sci.* **2008**, 23 (3), 217-228.
9. Tang, S.; Huang, X.; Zheng, N., *Chem. Comm.* **2011**, 47, 3948-3950.
10. Lee, C.; Kim, H.; Hong, C.; Kim, M.; Hong, S.S.; Lee, D.H.; Lee, W.I., *J. Mater. Chem.*, **2008**, 18 (40), 4790-4795.
11. Moon, H.K.; Lee, S.H.; Choi, H.C., *ACS Nano*, **2009**, 3 (11), 3707-3713.
12. Khlebtsov, B.N.; Khanadeev, V.A.; Maksimova, I.L.; Terentyuk, G.S.; Khlebtsov, N.G., *Nanotechnol. Russ.*, **2010**, 5 (7-8), 454-468.
13. Guo, R.; Zhang, L.; Qian, H.; Li, R.; Jiang, X.; Liu, B., *Langmuir*, **2010**, 26 (8), 5428-5434.
14. Link, S.; El-Sayed, M.A., *Int. Rev. Phys. Chem.*, **2000**, 19 (3), 409-453.
15. Richardson, H.H.; Hickman, Z.N.; Govorov, A.O.; Thomas, A.C.; Zhang, W.; Kordesch, M.E., *Nano Lett.*, 6 (4), 783-788.
16. Chou, C-H.; Chen, C-D.; Wang, C.R.C., *J. Phys. Chem. B.*, **2005**, 109 (22), 11135-11138.
17. Liu, G.L.; Kim, J.; Lu, Y.; Lee, L.P., *Nat. Mater.*, **2006**, 5 (1), 27-32.
18. Weissleder, R., *Nat. Biotechnol.*, **2001**, 19 (4), 316-317.
19. Winchester, D.J.; Winchester, D.P., *Breast Cancer 2nd Edition*, BC Decker, USA, 2006.
20. Kremkau, F.W., *J. Clin. Ultrasound*, **1979**, 7 (4), 287-300.
21. Goldberg, S.N., *Eur. J. Ultrasound*, **2001**, 13 (2), 129-147.
22. Wilson, B.C.; Patterson, M.S., *Phys. Med. Biol.* **1986**, 31 (4), 327-360.
23. Jiang, W.; Kim, B.Y.S.; Rutka, J.T.; Chan, W.C.W., *Nat. Nanotechnol.*, **2008**, 3 (3), 145-150.
24. Choi, H.S.; Liu, W.; Misra, P.; Tanaka, E.; Zimmer, J.P.; Ipe, B.I.; Bawendi, M.G.; Frangioni, J.V., *Nat. Biotechnol.*, **2007**, 25 (10), 1165-1170.
25. Alkilany, A.M.; Nagaria, P.K.; Hexel, C.R.; Shaw, T.J.; Murphy, C.J.; Wyatt, M.D., *Small*, **2009**, 5 (6), 701-708.
26. Park, J-H.; Gu, L.; von Maltzahn, G.; Ruoslahti, E.; Bhatia, S.N.; Sailor, M.J., *Nat. Mater.*, **2009**, 8 (4), 331-336.

27. Erogbogbo, F.; Tien, C-A.; Change, C-W.; Yong, K-T.; Law, W-C.; Ding, H.; Roy, I.; Swihart, M.T.; Prasad, P.N., *Bioconjugate Chem.*, **2011**, 22 (6), 1081-1088.
28. Hessel, C.M.; Henderson, E.J.; Veinot, J.G.C., *Chem. Mater.* **2006**, *18* (26), 6139-6146.
29. Buriak, J.M., *Chem. Rev.*, **2002**, 102 (5), 1271-1308.
30. Kelly, J.A.; Veinot, J.G.C., *ACS Nano*, **2010**, 4 (8), 4645-4656.
31. Beard, M.C.; Knutsen, K.P.; Yu, P.; Luther, J.M.; Song, Q.; Metzger, W.K.; Ellingson, R.J.; Nozik, A.J., *Nano Lett.*, **2007**, 7 (8), 2506-2512.
32. Protasenko, V.; Hull, K.L.; Kuno, M., *Chem. Edu.*, **2005**, 10 (4), 269-282
33. Weast, R.C.; Astle, M.J., *CRC Handbook of Chemistry and Physics*, Chemical Rubber Publishing Company, Boca Raton, Florida.
34. Goderfoo, S.; Hayne, M.; Jiavescu, M.; Stesmans, A.; Zacharias, M.; Lebedev, O.I.; Van Tendeloo, G.; Moshchalkov, V.V., *Nature Nanotech.*, **2008**, 3 (3) , 174-178.
35. Erogbogbo, F.; Yong, K-T.; Roy, I.; Xu, G.; Prasad, P.N.; Swihart, M.T., *ACS Nano*, **2008**, 2 (5), 873-878.
36. Anthony, R.J.; Rowe, D.J.; Stein, M.; Yang, J.; Kortshagen, U., *Adv. Funct. Mater.*, **2011**, ASAP.
37. Hessel, C.M.; Henderson, E.J.; Veinot, J.G.C., *J. Phys. Chem. C.*, **2007**, 111 (19), 6956-6961.
38. Cheylan, S.; Elliman, R.G., *Appl. Phys. Lett.*, **2001**, 78 (9), 1225-1227.
39. Alivisatos, A.P., *J. Phys. Chem.*, **1996**, 100 (31), 13226-13239.
40. Gaponenko, S.V., *Optical Properties of Semiconductor Nanocrystals*; Cambridge University Press, New York, 1998.

Chapter 3: Encapsulation of Silicon Nanocrystals within Mesoporous Silica Nanospheres

*Portions of this Chapter have been published:
Regli, S.; Kelly, J.A.; Veinot, J.G.C., *Mater. Res. Soc. Symp. Proc.*, **2011**, 1359 (NN), 149-154.

3.1 Introduction

3.1.1. Mesoporous Silica

Mesoporous silica, discovered in 1992 by Beck *et al.*, is a high surface area form of silica, with pores of sizes between 2-50 nm.[1, 2] A prototypical example of this class of material is MCM-41, abbreviated for Mobil Composition of Matter.[1] Mesoporous silica differs from other microporous materials (e.g., zeolites) in that the pores are formed using a templating agent (often a surfactant) and often exhibit regular spacing. These materials were first studied for uses in catalysis and adsorption applications where allowing molecules to access larger internal surfaces, enhances both catalytic activity and adsorbent capacity.[1,2]

The proposed mechanism for the formation of mesoporous silica is summarized in Schematic 3.1. The most crucial component for pore formation is the inclusion of a surfactant in the reaction mixture. A surfactant often used for MCM-41 formation is cetyltrimethylammonium bromide (CTAB), which has a 16-carbon chain hydrophobic tail and a quaternary ammonium cation as a hydrophilic head group. When a surfactant, such as CTAB, reaches a critical concentration (0.98 mM for CTAB in water), micelles form in solution.[3] As the surfactant concentration in solution becomes greater the micelle assemblies become ordered; the degree of ordering is dependant on surfactant concentration and surrounding temperature. An ordering phase diagram for CTAB is shown in Figure 3.1.[4] Since this ordering occurs in solution it is referred to as a liquid crystal (LC).[5]

To use this LC formation as a template for silica growth, a sol-gel reaction is performed (Appendix A). Using a precursor such as tetraethoxysilane (TEOS) hydrolysis and condensation occurs to form a large cross-linked network of silica, with silica filling the space surrounding micellar regions. The final step in the formation of mesoporous silica is the removal of the surfactant template by calcination or washing (Scheme 3.1).

Scheme 3.1: Proposed Mechanism for the Formation of Mesoporous Silica (adapted from reference 2)

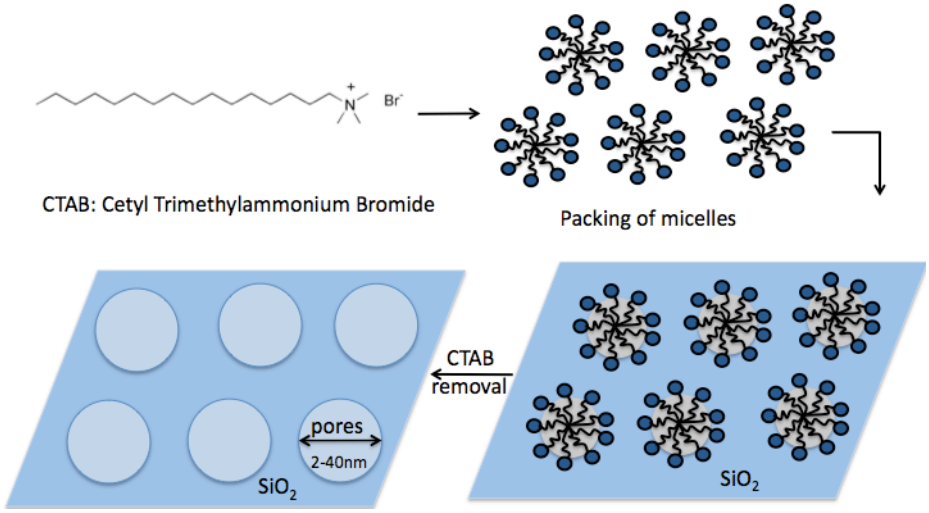

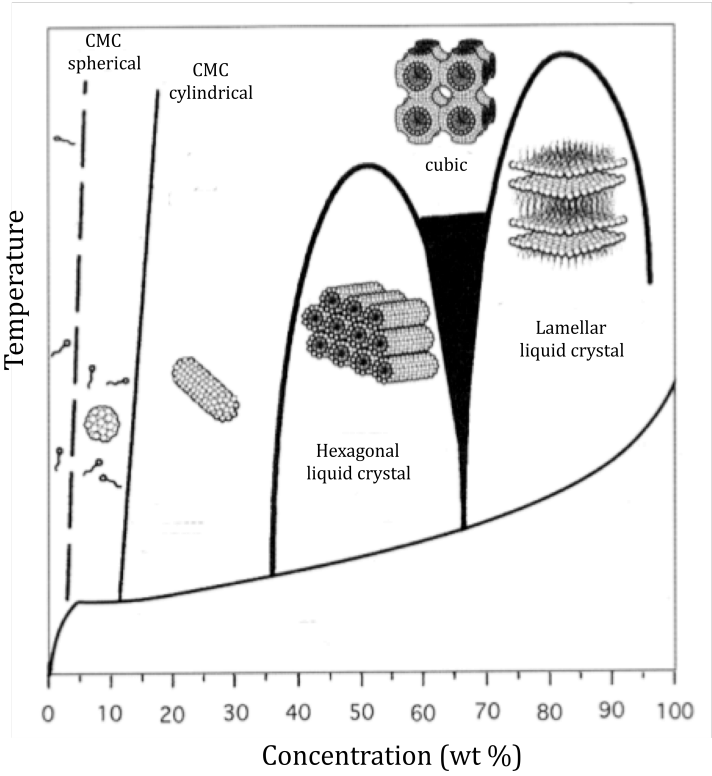

Figure 3.1: Phase Diagram of CTAB in water showing LC behaviour (adapted from reference 4)

3.1.2. Applications of Mesoporous Silica

Since its discovery, mesoporous silica has found its use in catalysis [6] and adsorption.[7] However the large interest in these porous materials has since spread to many other areas of application including sensing,[8] ion-exchange,[6] and drug delivery,[9] among others.[10,11,12] First discovered as an extension of adsorption inclusion chemistry, drug delivery is a particularly intriguing utilization of these materials.[13]

In 2001 Vallet-Regi *et al.*, reported the use of MCM-41 as a drug delivery system for the release of ibuprofen (IBU).[13] IBU was chosen for its pharmacological activity, its size (the size of IBU being ~1.0 nm x 0.6 nm and pore sizes being ~4 nm), and the potential for hydrogen bonding (Figure 3.2).[13]

Through UV-VIS spectroscopy and thermogravimetric analysis (TGA), Vallet-Regi *et al.* determined that MCM-41 pores could be effectively loaded with IBU by suspending a powder within an IBU/ hexanes solution.[13] The IBU loaded sample was added to a sample of simulated body fluid and the release of IBU into the fluid was monitored over time using UV-VIS spectroscopy.[13] This demonstration of drug-delivery showed great potential for different biological applications of mesoporous silica materials.

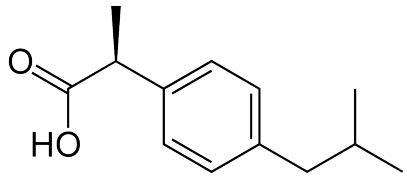

Figure 3.2: Structure of Ibuprofen

Investigations of using mesoporous silica for drug-delivery have studied the effects of varied functional groups,[14] different drugs,[15,16,17,18] and controlled release,[14,19,20] among others.[21,22] In particular, studies have shown that amine functionalization of the silica surface lead to higher IBU loading and slower rates of release as opposed to the hydroxyl terminated silica surface.[14] Vallet-Regí in numerous reports has shown the loading of different species into pores such as bovine serum albumin (BSA) and amoxicillin, through enlarging the pores to facilitate uptake of the larger BSA protein.[15, 16] Controlled release of a loaded drug has been achieved by methods of immobilization of proteins onto the pore entrance of mesoporous silica which can be triggered by the presence of saccharides for release of loaded molecules or by introduction of the drug into the micellar composition and released by change in pH.[19, 20] These examples are a few

of many within the field of mesoporous silica drug delivery. With further studies, these materials may find their potential use as an acceptable platform for delivery of nano-sized dosages of medicine with a controlled release.

3.1.3. Mesoporous Silica Encapsulation of Nanoparticles

In 2006, Kim *et al*. reported the formation of mesoporous silica encapsulated hydrophobic Fe_3O_4 nanoparticles (NPs), as a method of inducing water solubility of the initially hydrophobic NP.[23] In Scheme 3.2, the proposed mechanism for mesoporous silica encapsulation of hydrophobic NPs is shown. The first step in formation of mesoporous silica is a colloidal suspension of hydrophobic NPs. The second step is the addition of a surfactant to the colloidal NP solution. The surfactant in this step is utilized both as a phase transfer and templating agent. The surfactant (in this case CTAB), acts as a phase transfer agent from hydrophobic-hydrophobic interactions of the NP alkyl chains and the alkyl chains of the surfactant, rendering the NP water-soluble. CTAB also acts as a templating agent (although not depicted in the Scheme 3.2), from the packing of micelles around the surface, a key component in mesoporous silica formation (see Schematic 3.1). The final step is the addition of TEOS, a sol-gel precursor, to form a large cross-linked network of SiO_2 filling the space around micelles. Upon removal of the CTAB template, a porous silica shell is left surrounding the NP core, allowing aqueous dispersions of the hydrophobic particle.[23]

Scheme 3.2: Mechanism for formation of mesoporous silica encapsulated hydrophobic NPs (adapted from reference 23)

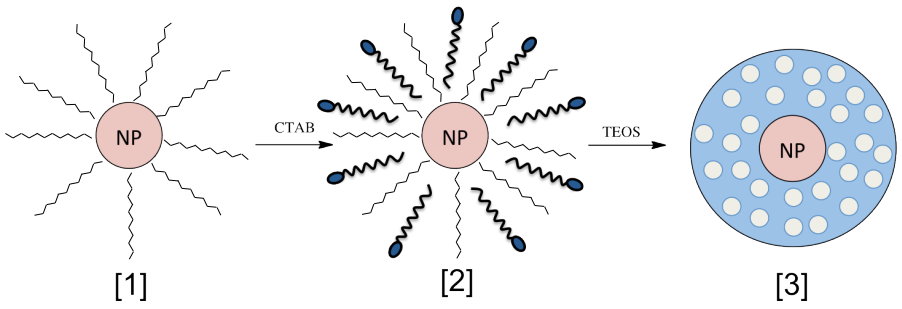

Figure 3.3 shows a transmission electron microscopy (TEM) image of mesoporous silica encapsulated Fe_3O_4 NPS where Kim *et al.* further showed the size of the mesoporous silica shell surrounding the NP was dependant on initial NP concentration; as the NP concentration decreased the resulting mesoporous silica nanosphere increased.[24] These materials were classified as multifunctional i.e., having more than one function with its magnetic Fe_3O_4 core, and a high surface area porous, inert shell. These two reports showed the potential for these multifunctional materials as an MRI imaging agent, a drug-delivery vehicle, and a fluorescence imaging tool upon functionalization of the silica surface with a dye.[23, 24]

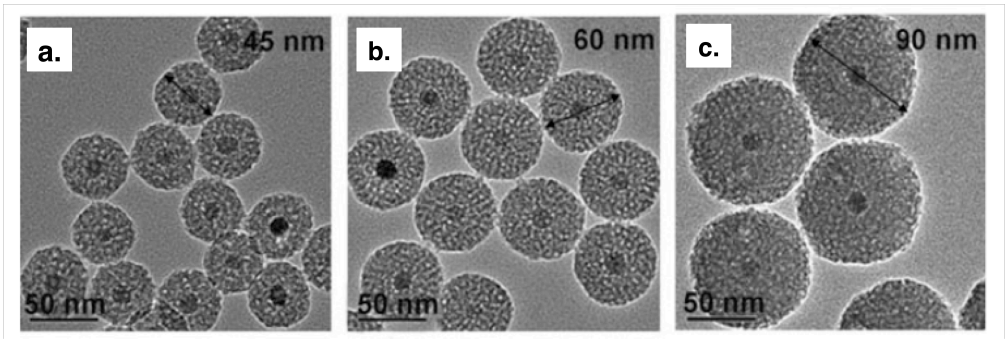

Figure 3.3: TEM images of mesoporous silica encapsulated Fe_3O_4 NPs with diameters of (a) 45 nm, (b) 60 nm and (c) 90 nm in order of decreasing initial NP concentration (from reference 24)

In 2009, the encapsulation of CdSe quantum dots (QDs) with mesoporous silica, was reported by Hu *et al*.[25] This particular synthesis was performed to form water soluble luminescent QDs for biological uses, however, the authors encountered substantial photoluminescence (PL) quenching of the silica encapsulated QDs after 48 hours of storage in ambient conditions.[25] Figure 3.4 shows the TEM images of these structures, along with the PL loss over time. The authors attributed this quenching to photo-induced oxidation occurring under ambient conditions through ligand exchange of the QD trioctylphosphine oxide (TOPO) ligand with the CTAB in solution.[25] A major issue regarding the use of these materials in biological media is the potential of leaching of cytotoxic Cd^{2+}.[26, 27]

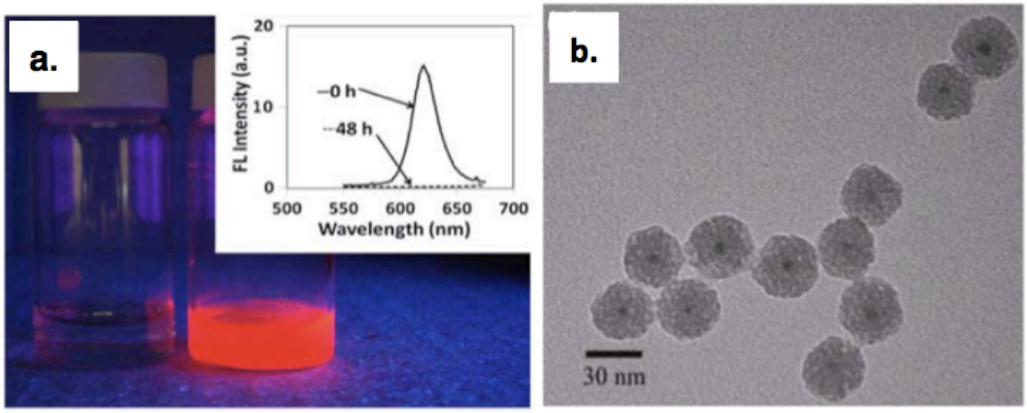

Figure 3.4: Mesoporous silica encapsulated CdSe QDs; a) PL 0 hours and 48 hours after encapsulation, b) TEM images showing the encapsulated particles (from reference 25)

In addition to those noted above, there are many other reports describing encapsulation of different NPs within a mesoporous silica shell. These extend from Au nanostructures,[28, 29] to MnO-NPs.[30] For encapsulated Au-NPs the effects of the shell growth on the optical properties were found to increase absorbance of

light in the NIR region of the electromagnetic spectrum, enhancing its photothermal properties.[28] Encapsulated Au nanorods (NRs), were synthesized to yield a porous silica platform that allowed for ready surface functionalization expanding the applicability of NRs.[29] MnO encapsulated NPs were synthesized and investigated as a potential MRI imaging agent.[30]

Si has recently been reported as non-toxic and this finding makes Si a suitable material for biological applications.[31,32] Since the formation of mesoporous multifunctional materials is a growing area of research for biological applications, combining luminescent Si-NCs with these materials is desirable. This chapter explores the formation of multifunctional mesoporous silica encapsulated Si-NCs and their possible applications in drug-delivery.

3.2 Materials and Methods

3.2.1. Reagents and Materials

Hydrogen silisesquioxane (HSQ) was obtained from Dow Corning under the tradename FOx® (flowable oxide) as a solution in methyl isobutyl ketone (MIBK). 2-[Methoxy(polyethyleneoxy)propyl] trimethyoxy silane (PEG-silane, MW 596-725 g/mol, 9-12 EO) was purchased from Gelest. Electronic grade hydrofluoric acid (49% $HF_{(aq)}$, J.T. Baker), reagent grades of toluene, hexanes, chloroform, hydrochloric acid, ethanol, methanol, ethyl acetate, ibuprofen (IBU) and tetraethoxy silane (TEOS) were obtained from Sigma Aldrich and used as received. Solid forms of sodium hydroxide (NaOH) and cetyltrimethylammonium bromide (CTAB) were obtained from Sigma Aldrich and used to prepare their

respective aqueous solutions. 1-dodecene, also purchased from Sigma Aldrich, was filtered through activated alumina to remove any peroxide impurities before use.

3.2.2. Encapsulation of Si-NCs within a Mesoporous Silica Shell

Dodecyl-terminated Si-NCs were synthesized using procedures described in Chapter 2 Sections 2.2.2-2.2.5. Mesoporous silica encapsulated Si-NCs were synthesized using a procedure similar to that reported by Kim *et al.*[23] For a typical synthesis 0.5 mL of a 50 mg/mL solution of Si-NCs in chloroform was added drop-wise to 5 mL of 55 mM CTAB solution and stirred to form an emulsion. The CTAB/NC mixture was stirred vigorously at 50°C for 30 min to form an aqueous dispersion of Si-NCs. The solution was transferred to a 100 mL round bottom flask and to it, 45 mL of 13 mM NaOH (pre-heated to 50°C), 0.5 mL of TEOS, and 3 mL of ethyl acetate were added in sequence resulting in a pale-yellow looking solution. The reaction mixtures was stirred overnight at room temperature.

Mesoporous silica encapsulated Si-NCs were purified by 4 cycles of centrifugation at 14000 rpm at 20 min per cycle using EtOH to suspend the particles. Resulting particles were placed in a glass vial and stored in EtOH until further use.

Mesoporous silica encapsulated Si-NCs were characterized using transmission electron microscopy, energy filtered transmission electron microscopy, and photoluminescence spectroscopy.

3.2.3. Improving Water-Solubility of Encapsulated Si-NCs

Encapsulation was performed as stated above. One hour after the addition of TEOS, 0.5 mL of PEG-silane was added. The solution was stirred for 30 min at 50°C and then aged at 50°C for 20 hours. The solution was filtered with a 0.45 μm hydrophilic nylon filter (Fisher) while warm and diluted to 50 mL with D.I. water. The solution was then heated to 90°C for 24 hours in a sealed vessel. The water-soluble encapsulated Si-NCs were dialyzed to remove excess surfactant.

Water-soluble, mesoporous silica encapsulated Si-NCs were characterized by transmission electron microscopy, dynamic light scattering, and photoluminescence spectroscopy.

3.2.4. Reagent Loading/ Release using Encapsulated Species

To load the pore of mesoporous silica encapsulated Si-NCs, procedures similar to that by Vallet-Regi *et al.* were followed.[13] In brief, 20 mg of a dried powder sample of encapsulated NCs (without the PEG-silane) was placed in a test tube. To the test tube, 10 mL of a 33 mg/mL IBU in hexanes solution was added and the mixture was stirred for 24 hours. Subsequently, the particles were isolated by centrifugation, the supernatant was removed, and the resulting precipitate was washed with hexanes. The particles were dried under an argon flow overnight. To the test tube containing dry particles, 10 mL of a pH=7 phosphate buffer was added. At specified time intervals, the test tube was placed into the centrifuge for 5 min, and a 100 μL aliquot was removed for analysis by UV-VIS spectroscopy in order to quantify the amount of IBU released into the buffer.

3.2.5. Transmission Electron Microscopy

Transmission electron microscopy (TEM) imaging was performed using a JEOL-2010 electron microscope. A LaB_6 filament was used for a thermionic emission source with an accelerating voltage of 200 keV. TEM imaging was performed on samples drop-coated from ethanol onto a carbon-coated copper grid.

3.2.6. Statistical Analysis using TEM images

With the TEM images obtained, a statistical analysis was performed to obtain mean nanosphere sizes. Particles sizes were measured using image processing software ImageJ. For a statistical analysis, 100 particles were measured for their size except in the case of nanospheres formed using 8.6 mg/mL and 15 mg/mL where only 50 particles could be measured due to the very large particle sizes. Standard deviations were reported at the 95% confidence level.

3.2.7. Photoluminescence Spectroscopy

PL spectra were obtained by irradiation of a glass vial, containing sample solution, with a 325 nm line of a He-Cd laser. Emitted photons were collected with a fiber optic connected to an Ocean Optics USB2000 spectrometer. The spectrometer spectral response was normalized using a black body radiator.

3.2.8. UV-VIS Spectroscopy

UV-VIS spectroscopy was performed using an Agilent 8453 instrument with UV-Visible ChemStation software. Samples were placed in a 50-2000 μL Eppendorf cuvette with a 2 mm path length.

3.3 Results and Discussion

The following describes the synthetic conditions for the synthesis of mesoporous silica encapsulated Si-NCs, and investigates the effects the synthesis has on the NC's optical properties.

3.3.1. Influence of Concentration on Resulting Nanosphere Size

The Si-NC mass concentration during the encapsulation procedure profoundly impacted the resultant nanosphere size. The general trend observed was nanosphere sizes decreased with increasing Si-NC concentration. This trend can be observed using TEM imaging shown in Figure 3.5 and also by a plot from mean nanosphere sizes in Figure 3.6. Figure 3.5a, shows mesoporous silica encapsulated Si-NCs using of 8.6 mg/mL of Si-NCs in chloroform. From this encapsulation condition a mean size of 369 nm ± 416 nm diameter nanospheres were obtained. Increasing the concentration to 15 mg/mL (Figure 3.5b), a bimodal size distribution is obtained with larger nanospheres having a mean size of 202 nm± 259 nm, surrounded by smaller non-sphereical agglomerates. Further increasing the Si-NC concentration to 28 mg/mL (Figure 3.5c), results in a mean size of 19.3 nm ± 7.7 nm in smaller particle aggregates (*ca.* 100 nm in size) and no large particles. Finally, when the Si-NC concentration was 50 mg/mL (Figure

3.5d) uniform nanospheres with a mean size of 31.8 nm ± 6.9 nm were realized. From TEM imaging the random porous nature of the shell is evident.

This trend of decreasing nanosphere size with increasing NC concentration can be rationalized by considering the proposed mechanism for NC encapsulation (Schematic 3.2). The second step shown in Schmatic 3.2 depicts the addition of a surfactant to an alkyl functionalized, organic solution of NCs. The surfactant, CTAB plays two roles in facilitating the templation of mesoporous silica nanospheres. First, interactions of the alkyl chains from the surfactant with the surface bonded alkyl chain (i.e., dodecyl) chain on the NC render the hydrophobic Si-NC water-soluble. Second, CTAB forms micelles nucleated around the now water-soluble particle. When NC concentration is low, there are few nucleation sites present in solution and micelle assembly occurs on only a few specific sites forming very large nanospheres. As the NC concentration increases there are many nucleation sites present leading to smaller and more uniform nanospheres. From the present studies, 50 mg/mL has been determined to be the optimal Si-NC concentration to obtain mesoporous silica nanospheres with narrow polydispersity containing a Si-NC core (with respect to the quantities and concentrations of the other reagents listed in 3.2.2).

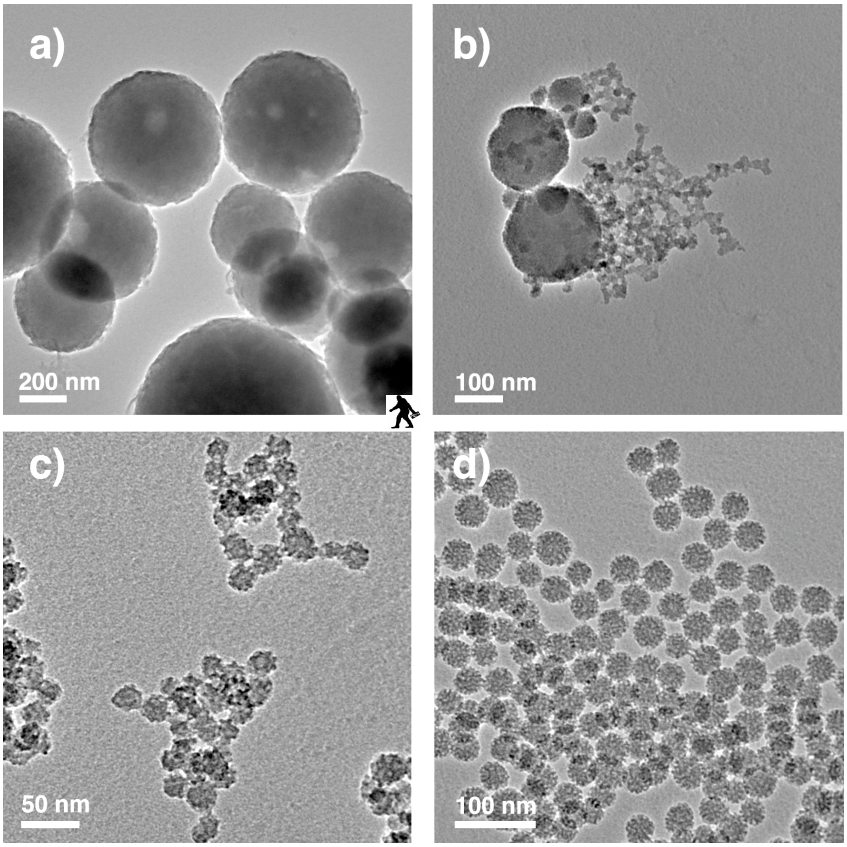

Figure 3.5: TEM images showing resulting nanosphere size from encapsulation with different concentrations of alkyl-terminated Si-NCs; a) 8.6 mg/mL, b) 15 mg/mL, c) 28 mg/mL and d) 50 mg/mL

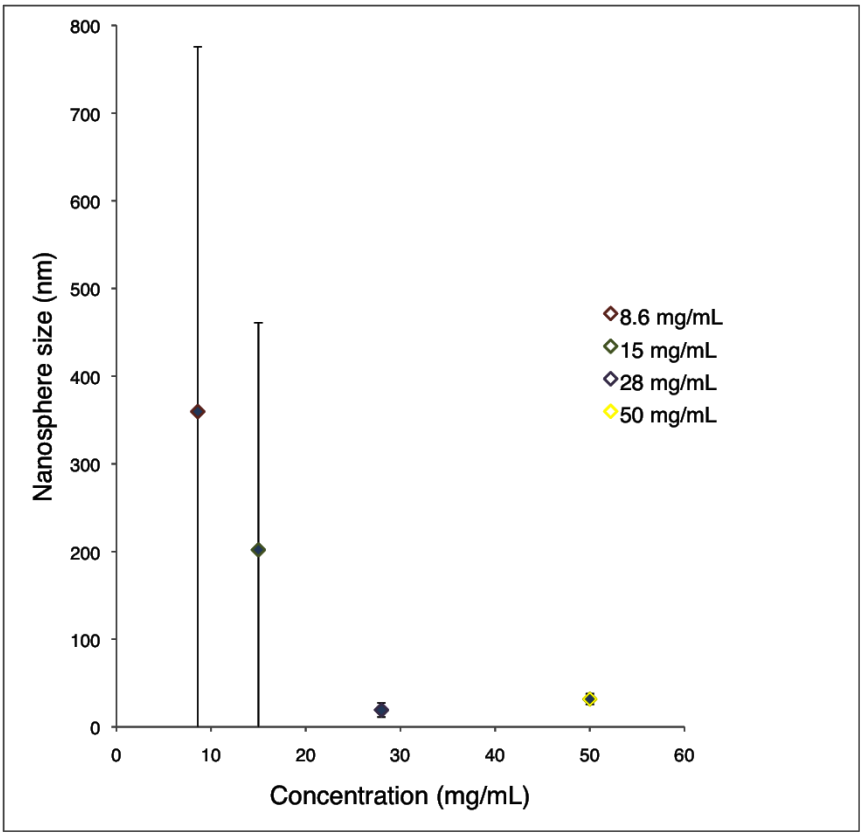

Figure 3.6: Plot of resultant nanosphere size after encapsulation using different Si-NC concentrations

3.3.2. Photoluminescent Properties of Encapsulated Si-NCs

A key motivation for preparing mesoporous silica encapsulated Si-NCs, was the realization of luminescent Si-NC species compatible with biological media (i.e. readily dispersible in biological media). After demonstrating such structures could be formed, PL of the encapsulated species were investigated. Figure 3.7 shows the PL taken at the indicated points throughout the synthetic procedure. Hydrophobic, dodecyl-terminated Si-NCs exhibit PL centered at *ca.* 750 nm. Addition of CTAB, rendering NCs water-soluble (second step in Scheme 3.2), induces a slight blue-shift in the PL to *ca.* 725 nm. Upon encapsulation of

the water soluble particle with a silica shell (i.e. after the addition of NaOH and TEOS) the PL further blue-shifts to *ca.* 670 nm.

The approximate 80 nm blue-shift was at first inspection an unexpected result because the Si-NCs have been passivated with dodecyl chains. Blue-shifts, along with loss of PL intensity, are often representative of Si-NC surface oxidation.[33, 34, 35] Strong bases, such as NaOH, will oxidize Si-hydride species, resulting in a blue-shift and loss of PL intensity.[36]

In the present system 13 mM NaOH was used to catalyze the sol-gel reaction of molecular precursor TEOS to form silica. This raises the concern of possible degradation of the particles due to oxidation from NaOH. The degree of oxidation would be challenging to analyze using standard spectroscopic techniques since the Si-NC core has a shell of silica surrounding it, and distinguishing between oxidation of the Si core and oxide species in the mesoporous shell would present a nontrivial challenge. Drawing conclusions about oxidation from PL intensities during various stages of the encapsulation reaction (Figure 3.7) also presents a challenge due to normalization of the PL curves and dilution from added reagents. Normalizing is essential for comparison because all PL measurements were performed using a He-Cd laser and intensities are relative to positioning of the fiber optic cable.

To evaluate the degree of oxidation of the NC core a qualitative, comparative experiment was performed. The experiment evaluated the change in PL intensity of the CTAB/Si-NC solution after the addition of base *in situ* (note this would be step 2 in Schematic 3.2, i.e., in the absence of TEOS). This

experiment was performed by the addition of 1 mL of 13 mM NaOH to a 5 mL sample of the CTAB/Si-NC solution in a vial, maintained in the same position with respect to the fiber optic cable. PL measurements were acquired at the specified time intervals and the corresponding spectra are shown in Figure 3.7b. After 1 minute of exposure to the base a slight blue-shift is observed in the PL. The PL maximum continues to blue-shift while decreasing in intensity over time. Three hours after NaOH addition the PL is completely quenched.

From this qualtitative comparison, it is evident that the mesoporous silica encapsulation process prevents the PL quenching observed for base addition to surfactant encapped NCs. This is shown in Figure 3.8 where the sample vials are placed atop of a standard bench-top UV-lamp.

From the qualitative PL experiments, it is postulated that partial oxidation of the Si-NC core is occurring during mesoporous silica encapsulation. It is apparent that formation of the silica shell prevents full PL quenching. It is reasonable that partial oxidation is occurring upon the initial addition of NaOH and as the sol-gel reaction proceeds, a protective later is formed around the Si-NC core inhibiting further diffusion of NaOH to the Si-NC core, protecting the PL.

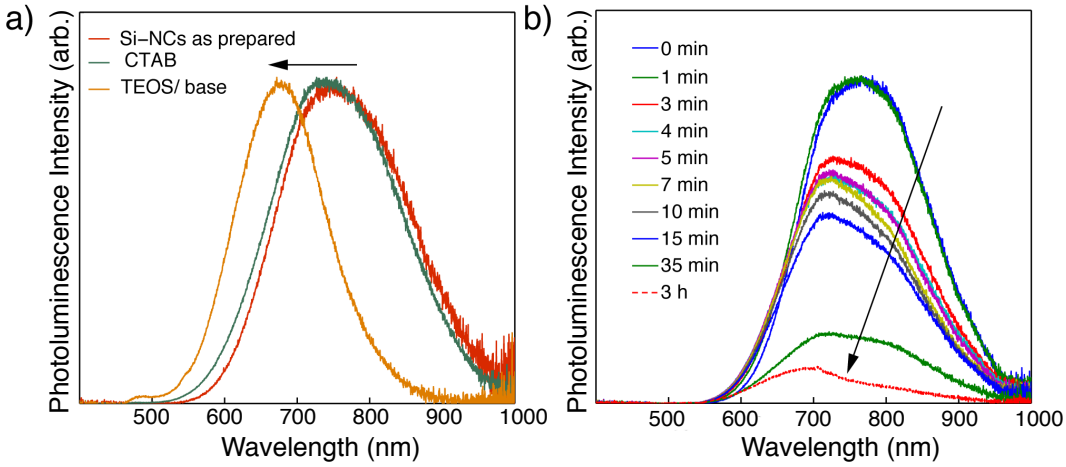

Figure 3.7: PL Spectra after irradiation with a 325nm line of a He-Cd laser; a) Normalized PL during encapsulation synthesis, b) PL after base addition to aqueous CTAB encapsulated Si-NCs

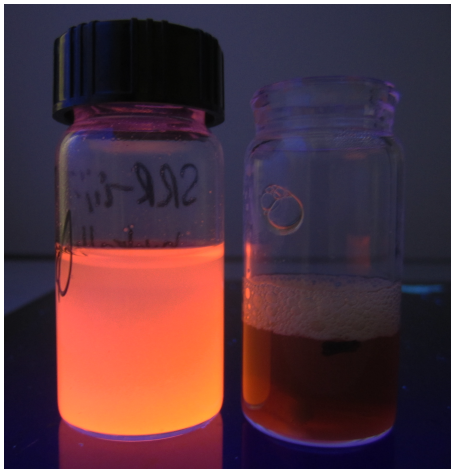

Figure 3.8: Qualitative PL from; Left- Mesoporous silica encapsulated Si-NCs in water, Right- CTAB/Si-NC emulsion 3 hours after base addition

3.3.3. Mesoporous Silica Encapsulation of Different Si-NC Sizes

Si-NCs larger than those described in Section 3.3.1 can be formed within the oxide matrix by increasing the processing temperature.[37,38] Through the influence of quantum confinement, larger NCs exhibit red-shifted PL into the near-IR (NIR) region of the electromagnetic spectrum.[39] This spectral region is of particular interest to biological imaging as tissue has a transparency window of

650-900 nm where absorption of light from water and hemoglobin is minimized.[40] In order to utilize the optical properties of NCs within the body, both excitation and emission photons need to be within this window.

Figure 3.9 shows low-resolution TEM images of encapsulated Si-NCs with core diameters ranging from 4 up to 9 nm. The polydispersity of the resulting mesoporous shells was quite similar; Si-NCs *ca.* 6 nm in size, gave an encapsulated nanosphere diameter of 29.9 nm ± 8.2 nm whereas for Si-NCs *ca.* 9 nm nanosphere diameters of 36.5 nm ± 10.8 nm are obtained. The slight difference in size may be attributable to the decrease in available nucleation sites as a function of increasing Si-NC size at the 50 mg/mL concentration.

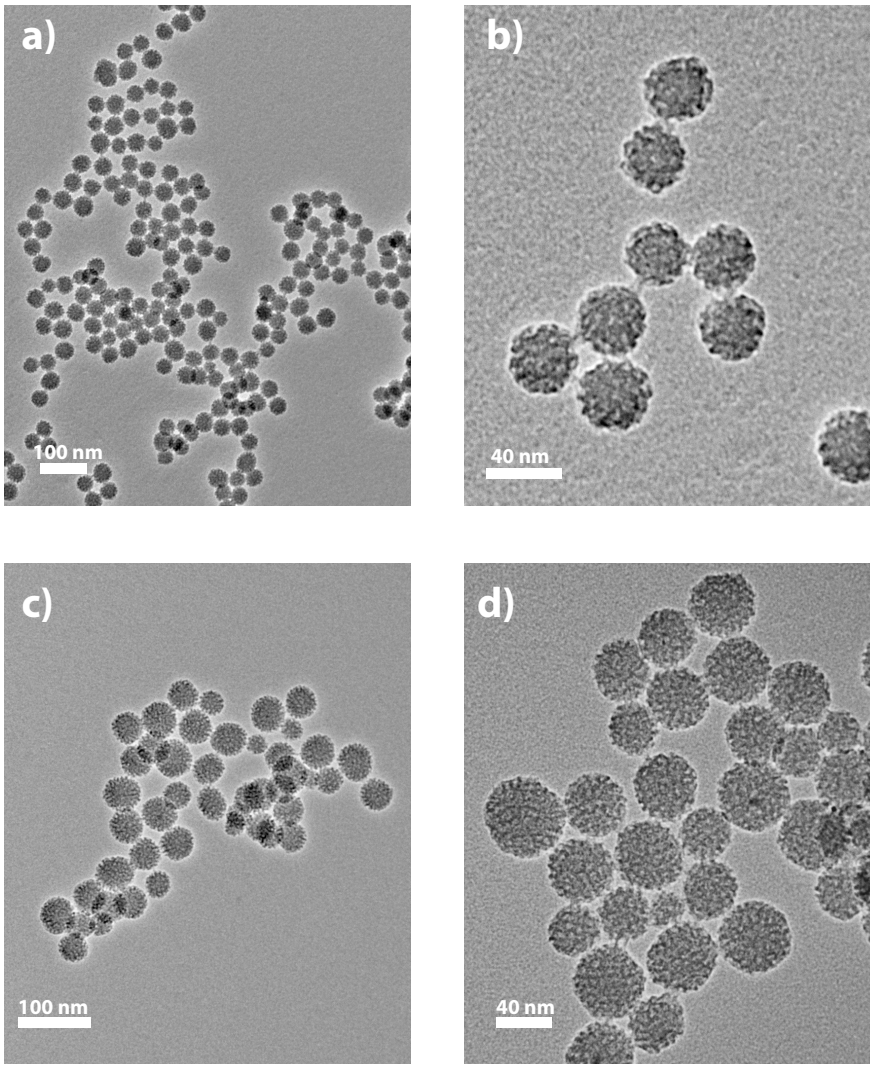

Figure 3.9: Mesoporous silica encapsulation of Si-NCs: a), b) approximately 6 nm in size c), d) approximately 9 nm in size

The encapsulation of larger Si-NCs was monitored by changes in the PL response. Figure 3.10 shows the Si-NC PL before and after encapsulation. As mentioned in Chapters 1 and 2, Si-NCs approximately 6 nm and 9 nm in size are formed by processing the NC/ oxide composite at 1200°C and 1300°C respectively. Figure 3.10a shows the PL of *ca.* 6 nm NCs (red trace) and the PL after encapsulation (blue trace). As was observed for the 4 nm NCs, a PL blue-

shift was observed after encapsulation (approximately 60 nm). The PL from 9 nm NCs (Figure 3.10b) is challenging to evaluate because of spectrometer limitations (i.e., detector and blackbody radiator cutoff). It is important to note that in Figure 3.10b, the encapsulated PL (green trace) was collected with an unusually high collection time (seconds). With these long collection times luminescence from the glass vial becomes significant at *ca.* 500 nm. Although, from Figure 3.10b there is not any clear indication of a shift, it important to note that Si-NCs *ca.* 9 nm in size encapsulated within a mesoporous silica shell exhibit NIR PL.

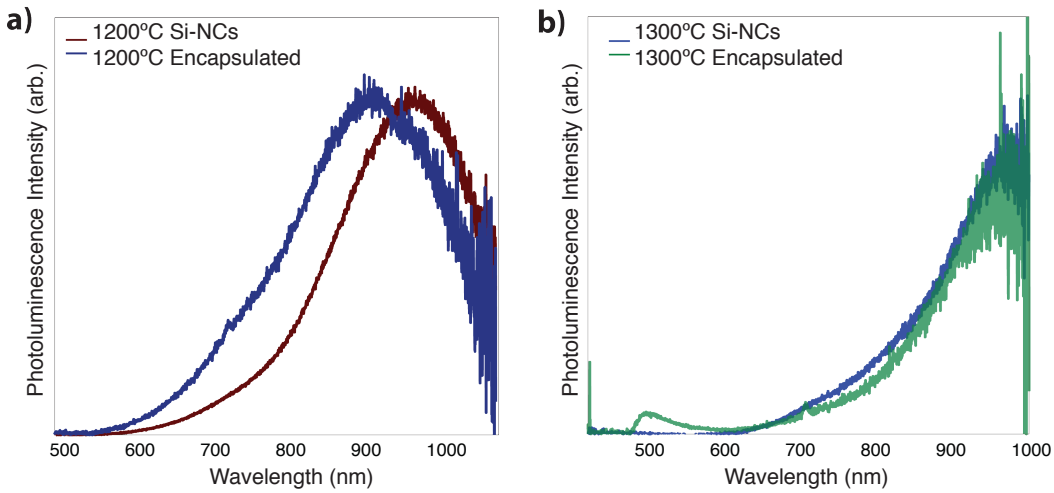

Figure 3.10: PL of larger NCs before and after encapsulation; a) ~6 nm and b) ~9 nm Si-NCs

3.3.4. TEM contrast of Mesoporous Silica Encapsulated Si-NCs

Direct comparision of TEM images obtained for mesoporous silica encapsulated Si-NCs with those obtained by Kim *et al.*[23] or Hu *et al.*,[25] shows the Si-NC cores are not directly visible where the NP core is very obvious with Fe_3O_3 and CdSe NP cores Figures 3.3-3.4. This is due to the limiting difference in contrast between the NP core and the silica shell.

In bright field TEM, an image is formed based upon the transmission of an electron beam through a thin specimen; for the present case nanospheres on an amorphous carbon coated copper grid. For samples reported by Kim[24] and Hu,[25] the Fe_3O_4 and CdSe NP cores have a differentiated contrast with silica, whereas silicon and silica have very similar contrasts in TEM. In bright field TEM imaging, the level of contrast is formed by the average atomic mass of the specimen.[41] The average atomic masses of silicon and silica are similar, resulting in similar contrasts in bright field TEM imaging. Since the average atomic mass of silicon is larger than that of silica, in a composite made up of Si-NCs embedded within a silica matrix, the Si-NCs would appear slightly darker than the silica matrix but would present a challenge to differentiate.[42]

High-resolution transmission electron microscopy (HRTEM) is a technique with exceptional resolution. In traditional bright-field TEM imaging, contrast within the image is achieved through changes in the amplitude of the incoming electron beam, sometimes referred to as "scattering contrast".[41] In HRTEM, contrast is achieved by changes in the electron wavefunction phase, sometimes referred to as "interference contrast", allowing for high-resolution images displaying the crystallinity of a sample.

A particular feature of some HRTEM instruments is the capability to perform energy filtered transmission electron microscopy (EFTEM). In EFTEM, a filter is used to select a specific energy inelastically scattered from the specimen. The energy lost from inelastic scattering is elemental specific, allowing for mapping of chemical species including the differentiation between silicon and

silica. Setting an energy filter (difference between initial electron beam and transmitted electron beam) to 0 eV improves the contrast of an image as all inelastically scattered beams are removed. By then setting an energy filter to 16 eV (corresponding to the plasmon loss of Si), regions containing Si can be filtered out.[43]

Figure 3.11 shows the results from HRTEM and EFTEM of mesoporous silica encapsulated *ca.* 6 nm Si-NCs. Figures 3.11a-b show HRTEM images of these encapsulated nanospheres. In a) the crystalline core of the Si-NC is visible (outlined by the red box). Figure 3.11 c-f show EFTEM of the same encapsulated Si-NCs. Figure 3.11 c, e show EFTEM images at different grid locations with an energy filter set to 0 eV. Figure 3.11 d, f show EFTEM images corresponding to the respective grid locations as in c) and e) with an energy filter set to 16 eV, to filter through electron beams with an energy loss characteristic of Si plasmon loss. From this investigation it became evident that a single Si-NC was encapsulated within the core of each MPS nanosphere.

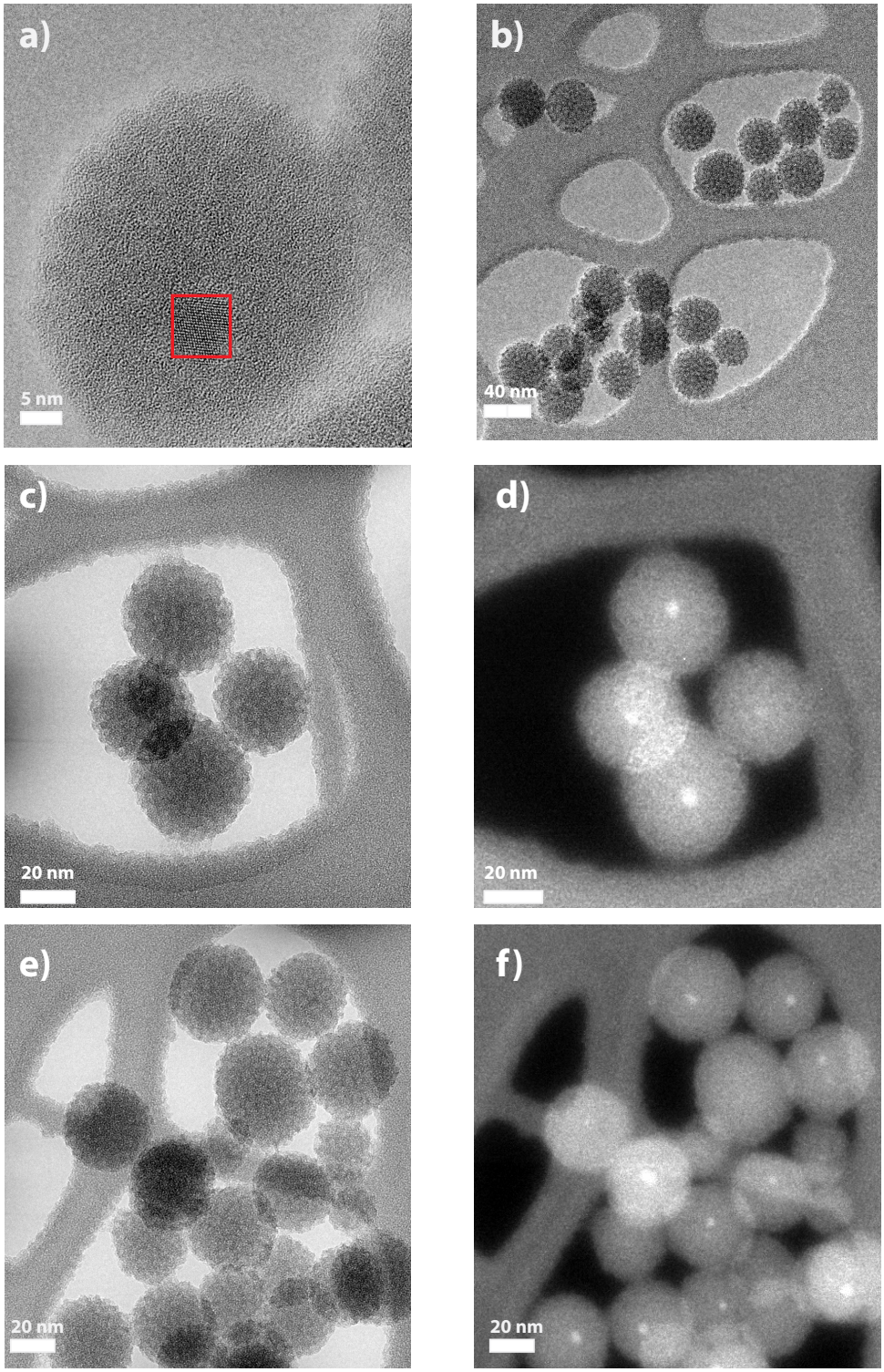

Figure 3.11: Mesoporous silica encapsulation of 5 nm Si-NCs; a) HRTEM of one single nanosphere, red box outlines the crystalline core, b) HRTEM of many nanospheres c) & e) EFTEM with a 0 eV energy filter, d) & f) EFTEM with a 16 eV energy filter correspond to their adjacent neighbors c) & e)

3.3.5. Water-Solubility of Mesoporous Silica Encapsulation Si-NCs

Many methods have been developed to synthesize organic-soluble Si-NCs,[44, 45] however methods for aqueous dispersions of Si-NCs are less common. Similar to alkyl passivated Si-NCs, it is possible to functionalize hydride terminated Si-NCs with olefins bearing terminal carboxylic acid or amine groups.[46, 47, 48, 49] Unfortunately, these surface groups often influence the PL response and lead to poorer surface passivation compared to alkyl surface modification.[48]

An alternative method for rendering NCs water soluble is to encapsulate alkyl passivated Si-NCs with a suitable dispersing agent. Erogbogbo *et al.* first showed this was possible by encapsulating many NCs within phospholipid micelles.[50] Hessel *et al.* presented the formation of water-soluble Si-NCs using alkyl terminated particles encapsulated within an amphiphilic polymer.[51] Recently, Henderson *et al.*, showed hydrophobic Si-NCs could be encapsulated within PEG-terminated solid lipid nanoparticles.[52] The effective preservation of PL provided by alkyl-termination has enabled the use of these initially hydrophobic Si-NCs in *in vivo* imaging applications.[50, 47, 52]

Mesoporous silica encapsulated Si-NCs, provides yet another alternative route to confer water-solubilty on the once hydrophobic NCs. While the hydroxyl-terminated silica surface allows for preferential dispersion in water over organic solvents, the nanoparticles tend to precipitate out over time (see Figure 3.12).

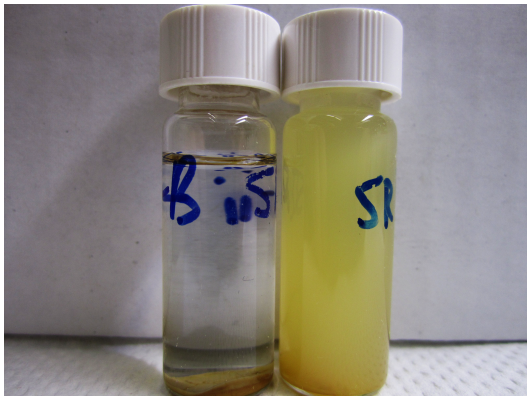

Figure 3.12: Mesoporous silica encapsulated Si-NCs in water, concentrate samples. Left- precipitation of the particles after 24 hours, Right- freshly shaken

Lin *et al.* showed that the stability of mesoporous silica NPs in biological media could be enhanced using a hydrothermal treatment of polyethylene glycol (PEG) functionalized NPs.[53] This synthesis utilized a PEG-silane to react with the surface of the mesoporous silica after the reaction had proceeded for approximately 1 hour.

This PEG hydrothermal treatment was applied to the present mesoporous silica encapsulated Si-NCs and resulted in increased water solubility. Figure 3.13a, shows a comparison of a vial of PEG-encapsulated NCs versus regular encapsulation. The solution of the PEG-encapsulated NCs is transparent. Figure 3.32b shows the PL of the water soluble nanospheres. The PL spectrum is identical to that obtained from the less soluble, unfunctionalized nanospheres.

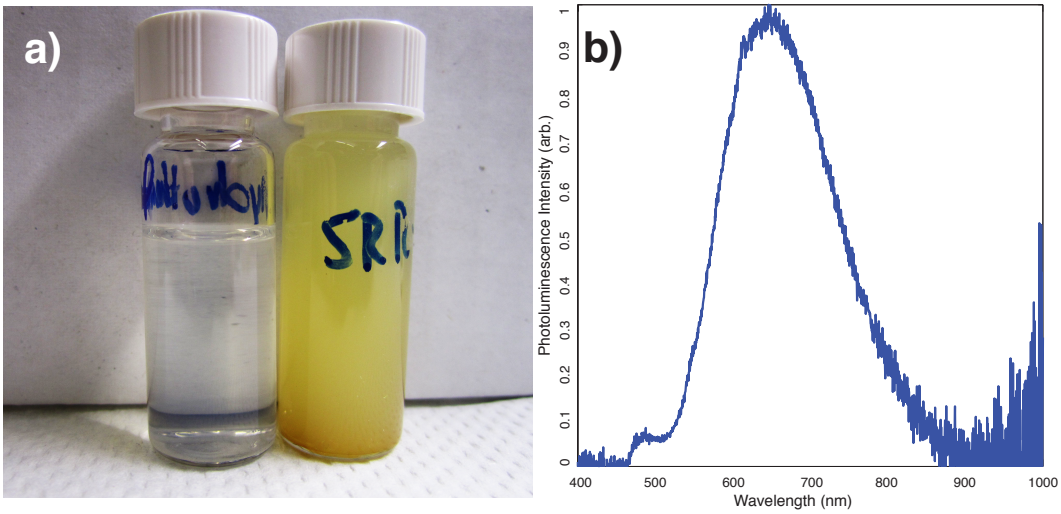

Figure 3.13: a) comparison of PEG-functionalized encapsulated Si-NCs (left) versus regular encapsulation (right), b) PL spectrum of water-soluble PEG-functionalized encapsulated Si-NCs

TEM was used to evaluate any changes resulting from the PEG-functionalization. It is clear in Figure 3.14, that the spherical shape is not maintained. The addition of the PEG-silane, appears to have caused agglomeration of the individual nanospheres into irregular shapes. The porosity of the water-soluble nanostructures is more evident than with the regular encapsulation, however. This may possibly be the result from effective removal of the CTAB surfactant template from the pores from the hydrothermal treatment (compare Figure 3.14 with Figure 3.5).

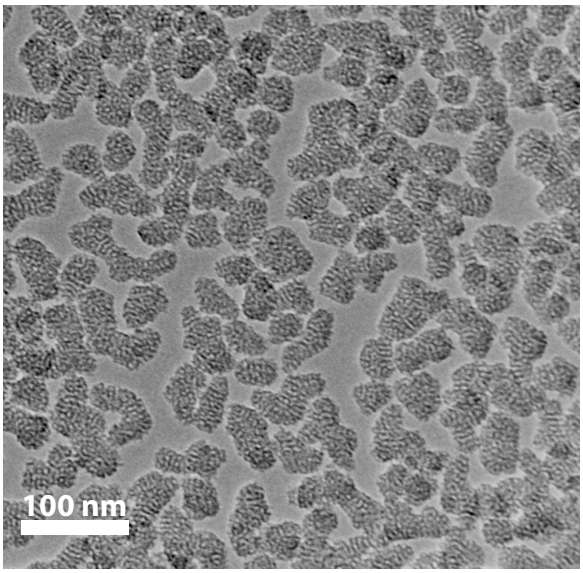

Figure 3.14: TEM of water-soluble PEG-silane functionalized nanospheres with Si-NC cores

Although the spherical nature of the mesoporous silica encapsulated Si-NCs is not maintained, their biological capabilities are not compromised. A luminescent, porous material is still obtained having potential for biological applications. Controlling the shape of water soluble, encapsulated Si-NCs is a subject for future investigation.

3.3.6. Drug Delivery Capabilities of Mesoporous silica encapsulated Si-NCs

One reason for preparing mesoporous silica encapsulated Si-NCs, was to form a biologically inert multifunctional material with luminescent properties. Some examples of Si-NCs being applied as a fluorescent, biological imaging agents have appeared.[47, 50, 52] Using methods described in 3.2.2.3 the encapsulated nanostructures can be loaded with a reagent such as ibuprofen (IBU), similar to bulk and nanoparticle mesoporous silica systems,[13] as well as other mesoporous

silica nanoparticle systems.[23] IBU loaded mesoporous silica encapsulated Si-NCs were dispersed into a phosphate buffer (pH=7) and the release of IBU using UV-VIS spectroscopy was monitored during specified time intervals. Figure 3.15a show typical UV-VIS spectra of IBU in a buffer. Each curve represents the absorbance of an aliquot of the supernatant at a specified time interval. This absorbance increases over time as IBU is released from the encapsulated nanostructures into the buffer. The absorbance maximum at 264 nm for IBU can be correlated to the mass of IBU released and a release curve can be plotted (See Figure 3.15b). The release curve begins to level off at 15.5 mg of IBU, indicating approximately 15.5 mg of IBU was loaded into the pores or adsorbed onto the nanosphere surface.

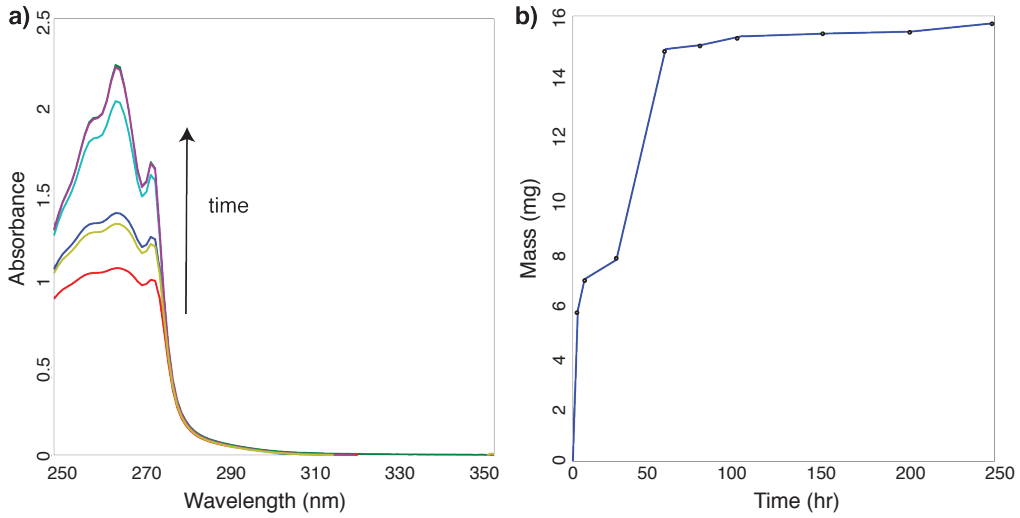

Figure 3.15: IBU release from mesoporous silica encapsulated Si-NCs ; a) UV-VIS spectroscopy data, b) Correlation to the amount of IBU released over time

In Figure 3.15b there is a feature in the curve at about 7 mg. This feature was unexpected, because a smooth increase has been reported for analogously encapsulated nanomaterials.[13,23] This feature could result from surface adsorbed

IBU initially diffusing into the buffer, followed by pore release. Increasing the washes of the loaded particles before dispersing into a buffer may effectively address this issue.

The release in Figure 3.15b shows that IBU can be released from mesoporous silica encapsulated Si-NCs and that mesoporous silica encapsulated Si-NCs hold promise as a drug-delivery vehicle. This is useful since Si-NCs are expected to be non-toxic in analogy to their porous Si counterparts. Park *et al.* have shown that a biodegradation product of p-Si is silicic acid ($Si(OH)_4$), which is effectively excreted from the human body through urine.[54]

By combining the luminescent properties of the NCs with the drug-delivery capabilities, and solubility in biological media these materials may hold promise as a multifunctional biological tool.

3.4. Conclusions

Mesoporous silica encapsulated Si-NCs have been effectively synthesized and the impact of the encapsulation process on the Si-NC PL evalulated. The initial Si-NC concentration was found to significantly alter the size of the mesoporous silica shell with a concentration of 50 mg/mL of Si-NCs in $CHCl_3$ determined to be the optimal NC concentration to prepare *ca.* 30 nm silica spheres with narrow polydispersity. The encapsulation method has also been extended to a range of NC sizes, as well as to include a PEG-functional group on the silica shell to enhance the water dispersibility. EFTEM was used to conclusively identify the presence of the Si-NC core within the nanosphere, and proof-of-concept drug release from the nanostructures was demonstrated.

This method to render hydrophobic Si-NCs compatible with biological media is unique in that it also presents a secondary function for drug-delivery through the high surface area mesopores. The presented synthesis does not compromise the Si-NC PL, minimizing changes such as quenching or shifts in the PL maxima when stored over months. By combining the luminescent properties of the NCs with drug-delivery capabilities, these materials may hold promise as a multifunctional biological tool.

3.5 References

1. Kresge, C.T.; Leonowicz, M.E.; Roth, W.J.; Vartuli, J.C.; Beck, J.S., *Nature*, **1992**, 359, 710-714.
2. Beck, J.S.; Vartuli, J.C.; Roth, W.J.; Leonowicz, M.E.; Kresge, C.T.; Schmitt, K.D.; Chu, C.T-W.; Olson, D.H.; Sheppard, E.W.; McCullen, S.B.; Higgins, J.B.; Schlenker, J.L., *J. Am. Chem. Soc.* **1992**, 114 (27), 10834-10843.
3. Okuda, H.; Imae, T.; Ikeda, S., *Colloids Surf.* **1987**, 27, 187.
4. Brinker, C.J.; Lu, Y.; Sellinger, A.; Fan, H., *Adv. Mater.* **1999**, 11 (7), 579-585.
5. Rosevear, F.B., *J. Soc. Cosmetic Chemists*, **1968**, 19, 581-594.
6. Trong On, D.; Desplantier-Giscard, D.; Danumah, C.; Kaliaguine, S., *Appl. Catal., A*, **2001**, 222 (1-2), 299-357.
7. Hartmann, M., *Chem. Mater.* **2005**, 17 (18), 4577-4593.
8. Melde, B.J.; Johnson, B.J.; Charles, P.T., *Sensors*, **2008**, 8 (8), 5202-5228.
9. Wang, S., *Microporous Mesoporous Mater.* **2009**, 117 (1-2), 1-9.
10. Giraldo, L.F.; López, B.L.; Pérez, L.; Urrego, S.; Sierra, L.; Mesa, M., *Macromol. Symp.*, **2007**, 258 (1), 129-141.
11. Shopsoqitz, K.E.; Qi, H.; Hamad, W.Y.; MacLachlan, M.J., *Nature*, **2010**, 468 (7322), 422-426.
12. Chernysheva, M.V.; Sapoletova, N.A.; Eliseev, A.A.; Lukashin, A.V.; Tretyakov, Y.D.; Goernet, P., *Pure Appl. Chem.*, **2006**, 78 (9), 1749-1757.
13. Vallet-Regí, M.; Rámila, A.; del Real, R.P.; Pérez-Pariente, J., *Chem. Mater.* **2001**, 13 (2), 308-311.
14. Manzano, M.; Aina, V.; Areán, C.O.; Balas, F.; Cauda, V.; Colilla, M.; Delgado, M.R.; Vallet-Regí, M., *Chem. Eng. J.* **2008**, 137 (1), 30-37.
15. Vallet-Regí, M.; Balas, F.; Colilla, M.; Manzano, M., *Prog. Sold State Chem.*, **2008**, 36 (3), 163-191.
16. Vallet-Regí, M.; Doadrio, J.C.; Doadrio, A.L.; Izquierdo-Barba, I.; Pérez-Pariente, J., *Solid State Ionics*, **2004**, 172 (1-4), 435-439.
17. Zhao, Y.; Lin, L-N.; Lu, Y.; Chen, S-F.; Dong, L.; Yu, S-H., *Adv. Mater.*, **2010**, 22 , 5255-5259.
18. Colilla, M.; Izquierdo-Barba, I.; Vallet-Regí, M., *Expert Opin. Ther. Patents*, **2008**, 18 (6), 639-656.
19. Zhao, Y.; Trewyn, B.G.; Slowing, I.I.; Lin, V.S-Y., **2009**, 131 (24), 8398-8400.
20. He, Q.; Gao, Y.; Zhang, L.; Zhang, Z.; Gao, F.; Ji, X.; Li, Y.; Shi, J., *Biomaterials*, **2011**, 32 (30).
21. Cotí, K.K.; Belowich, M.E.; Liong, M.; Ambrogio, M.W.; Lau, Y.A.; Khatib, H.A.; Zink, J.I.; Khashab, N.M.; Stoddart, J.F., *Nanoscale*, 1 (1), 16-39.
22. Popat, A.; Hartono, S.B.; Stahr, F.; Liu, J.; Qiao, S.Z.; Lu, G.Q., *Nanoscale*, **2011**, 3 (7), 2801-2818.
23. Kim, J.; Lee, J.E.; Lee, J.; Yu, J.H.; Kim, B.C.; An, K.; Hwang, Y.; Shin, C-H.; Park, J-G.; Kim, J.; Hyeon, T., *J. Am. Chem. Soc.* **2006**, 128 (3), 688-689.
24. Kim, J.; Kim, H.S.; Lee, N.; Kim, T.; Kim, H.; Yu, T.; Song, I.C.; Moon, W.K.; Hyeon, T., *Angew. Chem. Int. Ed.* **2008**, 47 (44), 8438-8441.

25. Hu, X.; Zrazhevskiy, P.; Gao, X., *Ann. Biomed. Eng.* **2009**, 37 (10), 1960-1966.
26. Kirchner, C.; Liedl, T.; Kudera, S.; Pellgrino, T.; Javier, A.M.; Gaub, H.E.; Stölzle, S.; Fertig, N.; Parak, W.J., *Nano Lett.* **2005**, 5 (2), 331-338.
27. Fu, A.; Gu, W.; Larabell, C.; Alivisatos, A.P., *Curr. Opin. Neurobiol.* **2005**, 15, 568-575.
28. Botella, P.; Corma, A.; Navarro, M.T.; Quesada, M., *J. Mater. Chem.* **2009**, 19 (20), 3168-3175.
29. Gorelikov, I.; Matsuura, N., *Nano Lett.* **2008**, 8 (1), 369-373.
30. Peng, Y.-K.; Lai, C.-W.; Liu, C.-L.; Chen, H.-C.; Hsiao, Y.-H.; Liu, W.-L.; Tang, K.-C.; Chi, Y.; Hsiao, J.-K.; Lim, K.-E.; Liao, H.-E.; Shyue, J.-J.; Chou, P.T., *ACS Nano,* **2011**, 5 (5), 4177-4187.
31. Alsharif, N.H.; Berger, C.E.M.; Varanasi, S.S.; Chao, Y.; Horrocks, B.R.; Datta, H.K., *Small*, **2009**, 5 (2), 221-228.
32. Bimbo, L.M.; Sarparanta, M.; Santos, H.A.; Airakasinen, A.J.; Mäkilä, E.; Laaksonen, T.; Peltonen, L.; Lehto, V-P.; Hirvonven, J.; Salonen, J., *ACS Nano*, **2010**, 4 (6), 3023-3032.
33. Pi, X.D.; Mangolini, L.; Campbell, S.A.; Kortshagen, U., *Phys. Rev. B.* **2007**, 75 (8), 085231-0854235.
34. Prtljaga, N.; D'Amato, E.; Pitanti, A.; Guider, R.; Froner, E.; Larcheri, S.; Scarpa, M.; Pavesi, L., *Nanotechnology*, **2011**, 22 (21), 2157041-2157049.
35. Biteen, J.S.; Lewis, N.S.; Atwater, H.A.; Polman, A., *Appl. Phys. Lett.* **2004**, 84 (26), 5389-5391.
36. Greenwood, N.N.; Earnshaw, A., *Chemistry of the Elements*; Pergamon Press, New York, 1984.
37. Hessel, C.M.; Henderson, E.J.; Veinot, J.G.C.; *J. Phys. Chem. C*, **2007**, 111 (19), 6956-6961.
38. Kelly, J.A.; Shukaliak, A.M.; Fleischauer, M.D.; Veinot, J.G.C., *J. Am. Chem. Soc.*, **2011**, 133 (24), 9564-9571.
39. Kim, T-Y.; Park, N-M.; Kim, K-H.; Sun, G.Y.; Ok, Y-W.; Seong, T-Y.; Choi, C-J., *Appl. Phys. Lett.* **2004**, 85 (22), 5355-5357.
40. Weissleder, R.; *Nat. Biotechnol.*, **2001**, 19 (4), 316-317.
41. Williams, D.B.; Carter, C.B., *Transmission Electron Microscopy*, Plenum Press, New York and London, 1996.
42. Hessel, C.M.; Henderson, E.J.; Veinot, J.G.C., *Chem. Mater.* **2006**, 18 (26), 6139-6146.
43. Duan, X.F.; Du, A.Y.; Chu, Y.M., *J. Appl. Phys.* **1991**, 70 (3), 1850-1852.
44. Veinot, J.G.C., *Chem. Commun.* **2006**, (40), 4160-4168.
45. Kelly, J.A.; Henderson, E.J.; Veinot, J.G.C., *Chem. Commun.* **2010**, 46 (46), 4645-4656.
46. Clark, R.J.; Dang, M.K.; Veinot, J.G.C., *Langmuir*, **2010**, 26 (19), 15657-15664.
47. Sato, S.; Swihart, M.T., *Chem. Mater.* **2006**, 18 (17), 4083-4088.
48. Li, Z.F.; Ruckenstein, E., *Nano Lett.* **2004**, 4 (8), 1463-1467.

49. Warner, J.H.; Hoshino, A.; Yamamoto, K.; Tilley, R.D., *Angew. Chem. Int. Ed.* **2005**, 44 (29), 4550-4554.
50. Erogbogbo, F.; Yong, K-T.; Roy, I.; Hu, R.; Law, W-C.; Zhao, W.; Ding, H.; Wu, F.; Kumar, R.; Swihart, M.T.; Prasad, P.N., *ACS Nano*, **2011**, 5 (1), 413-423.
51. Hessel, C.M.; Rasch, M.R.; Hueso, J.L.; Goodfellow, B.W.; Akhavan, V.A.; Puvanakrishnan, P.; Tunnel, J.W.; Korgel, B.A., *Small*, **2010**, 6 (18), 2026-2034.
52. Henderson, E.J.; Shuhendler, A.J.; Prasad,P.; Baumann, V.; Maier-Flaig, F.; Faulkner, D.O.; Lemmer, U.; Wu, X.Y.; Ozin, G.A., *Small*, **2011**, 7 (17), 2507-2516.
53. Lin, Y-S.; Abadeer, N.; Haynes, C.L., *Chem. Commun.* **2011**, 47 (1), 532-534.
54. Park, J-H.; Gu, L.; von Maltzahn, G.; Ruoslahti, E.; Bhatia, S.N.; Sailor, M.J., *Nat. Mater.*, **2009**, 8 (4), 331-336.

Chapter 4: Conclusions and Future Work

4.1 Conclusions

The present thesis explored the synthesis and functionalization of Si-NCs for biomedical applications. The photo-induced heating of Si-NCs was studied for potential use as a photothermal therapy (PTT) agent. This was followed by a synthetic study of the encapsulation of Si-NCs within mesoporous silica nanospheres.

Chapter 2 presented a mechanistic study for the origin of the PT effect in Si-NCs and the resulting impact on NC size. The exploration of different NC sizes revealed an enhanced PT effect from larger Si-NCs. Upon analysis using different irradiation wavelengths and NC samples formed from increased thermal processing times (fewer defects), it was proposed that the observed PT effect for Si-NCs was dominated due to carrier cooling.

Although Si-NCs absorb significantly less light than Au-nanorods (Au-NRs), Si-NCs show comparable PT effects when NC/toluene solutions are irradiated with a 1W 532 nm solid-state diode laser where higher Si-NC concentrations are required.[1] The advantage of investigating Si-NCs as photothermal therapy (PTT) agents lies in the non-toxicity of Si and the NC size, where 5-50 nm is the optimal size window to maximize bloodstream circulation time and the surfactant commonly used as a stabilizing agent (CTAB) has been shown to be toxic.[2,3,4]

Chapter 3 of the present thesis discussed the synthesis of mesoporous silica encapsulated of Si-NCs. Mesoporous silica nanospheres 30 nm in size with a 4 nm Si-NC core were synthesized by adapting synthetic procedures used for the encapsulation of magnetic NPs.[5] Encapsulated Si-NCs remained luminescent and experienced a blue-shift in their PL. Upon functionalization of the SiO_2 surface with PEG, the solubility of the

nanospheres in water was greatly enhanced while maintaining PL. Using ibuprofen (IBU), proof-of-concept drug loading and release were demonstrated, suggesting the potential for application of these nanospheres as a fluorescent drug-delivery vehicle.

The present thesis as a whole studied the ability for Si-NCs to be used as a potential PTT agent, biological imaging agent, and drug-delivery vehicle.

4.2 Future Work

To assess the Si-NCs studied in Chapter 2 as possible PTT agents, exploration into cancer cell death and near-IR irradiation is necessary. This could be done first by observing the PT effects resulting from NIR irradiation and second by observing cancer cell death after NC incubation and irradiation. These proposed studies should be sufficient in deducing the effectiveness of Si-NCs as PTT agents by comparing to studies involving Au-NRs.

Great potential lies in linking the results presented in Chapter 2 and Chapter 3. This project will investigate the possibility of using mesoporous silica encapsulated Si-NCs as a PT drug-delivery vehicle for targeted drug-release. The hypothesis is drug release from the mesoporous silica may be induced or expedited by the PT heating of the encapsulated Si-NC core. A preliminary study is shown in Figure 4.1. After one hour, a sample of mesoporous silica encapsulated Si-NCs has released 0.00570 mg of IBU in contrast to 0.0248 mg of IBU upon irradiation of an identical sample with a 250 mW (532 nm) laser. These preliminary results hold promise that these materials could be employed in PT drug-release for targeted drug-delivery. Further investigations are

required in order to quantitatively and statistically analyze the differences in IBU release resulting from laser irradiation.

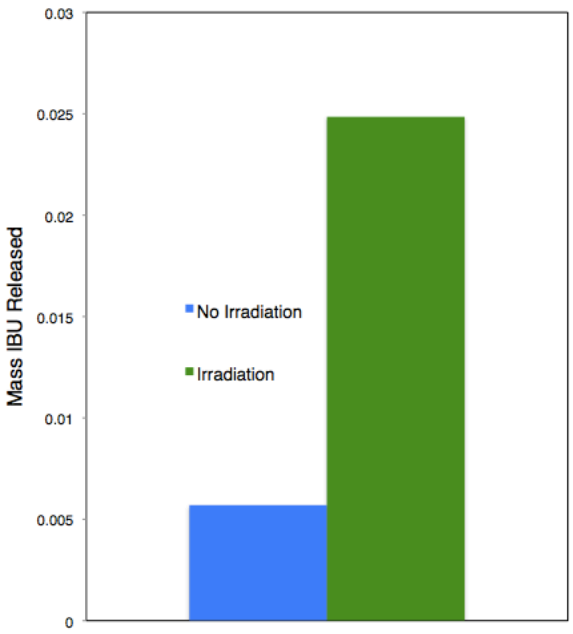

Figure 4.1: Ibuprofen release from mesoporous silica encapsulated Si-NCs over 1 hour

One method of characterization to enhance the study reported in Chapter 3 is the characterization of the porosity for the nanospheres. Obtaining pore size values will be a method to confirm whether the Si-NC system presented in Chapter 3 is in true anaology to the Fe_3O_4 system presented by Kim *et al.*[5] Porosity is often characterized using gas adsorption techniques. Within the chapter the functionalization study of the nanosphere surface with PEG groups facilitated enhanced water-solubility but the spherical nature of the nanospheres was compromised. Upon further investigation of PEG:TEOS ratios, spherical nature may possibly be retained.

In order to fully realize the utilization of mesoporous silica encapsulated Si-NCs in biological systems, the toxicity of nanosphere solutions in water should be assessed. Since the surfactant used for encapsulation (CTAB) is highly toxic, toxicity studies would be important to ensure complete surfactant removal is achieved. If these structures are found to be toxic, similar encapsulation syntheses with different non-toxic surfactants would prove useful to realize these nanospheres within biological applications such as fluorescent imaging.

Fluorescence imaging of cells using these mesoporous silica encapsulated Si-NCs with the enhanced water-solubility, is another area of study for these materials. The results in Chapter 3 showed that encapsulated Si-NCs maintain a photoluminescence which does not degrade over time, this particular result makes these materials ideal candidates for biological imaging. Fluorescence imaging is an important tool for imaging cells and is has been proven to be a useful tool for cancer cell identification.

This thesis has laid the preliminary groundwork for Si-NCs (derived from hydrogen silsesquioxane) to be potentially used in different biological applications ranging from photothermal cancer therapy, to drug-delivery and fluorescence imaging.

4.3 References

1. Chen, H.; Shao, L.; Ming, T.; Sun, Z.; Zhao, C.; Yang, B.; Wang, J., *Small*, **2010**, 6 (20), 2272-2280.
2. Jiang, W.; Kim, B.Y.S.; Rutka, J.T.; Chan, W.C.W., *Nat. Nanotechnol.*, **2008**, 3 (3), 145-150.
3. Choi, H.S.; Liu, W.; Misra, P.; Tanaka, E.; Zimmer, J.P.; Ipe, B.I.; Bawendi, M.G.; Frangioni, J.V., *Nat. Biotechnol.*, **2007**, 25 (10), 1165-1170.
4. Alkilany, A.M.; Nagaria, P.K.; Hexel, C.R.; Shaw, T.J.; Murphy, C.J.; Wyatt, M.D., *Small*, **2009**, 5 (6), 701-708.
5. Kim, J.; Lee, J.E.; Lee, J.; Yu, J.H.; Kim, B.C.; An, K.; Hwang, Y.; Shin, C-H.; Park, J-G.; Kim, J.; Hyeon, T., *J. Am. Chem. Soc.* **2006**, 128 (3), 688-689.

Appendix A: Sol-Gel Processes for Silicate Materials

Sol-gel processing is a method for preparing amorphous oxide materials using a soft chemical approach. The term *sol* refers to a stable suspension of very small particles in a liquid and the word *gel* refers to a porous continuous solid network surrounding and supporting a liquid phase.[1]

Silicate sol-gel processing proceeds first by hydrolysis and condensation of silicon-based precursors to form sols, followed by gelation. These processes will be described briefly below.

Hydrolysis and Condensation

Silicon alkoxides, $Si(OR)_4$, are common sol-gel precursors. The overall reaction for sol-gel processing of these types of precursors is given by:

$$Si(OR)_4 + 2\,H_2O \longrightarrow SiO_2 + 4\,ROH$$

A SiO_2 sol is formed upon addition of water to the alkoxide precursor. This overall reaction can be considered as two different categories of reactions: hydrolysis and condensation.

Hydrolysis:

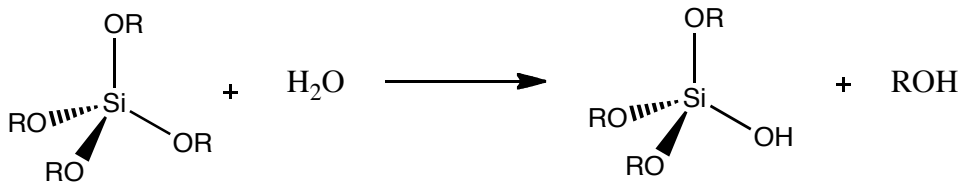

[1] Schubert, U.; Hüsing, N., *Synthesis of Inorganic Materials 2nd Edition*, Wiley-VCH, Weinheim, 2005.

Condensation:

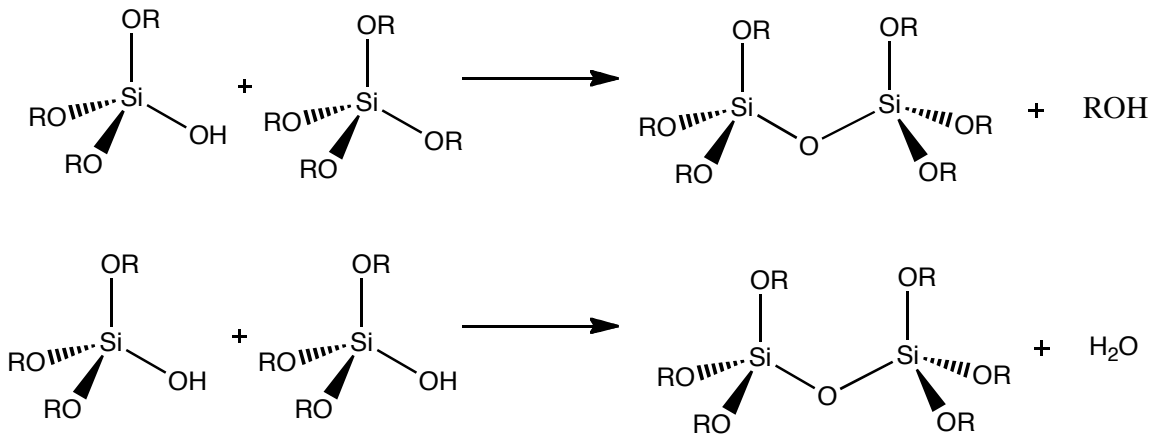

These general hydrolysis and condensation reactions are the basis to sol-gel reactions and proprogate to form a sol. Hydrolysis and condensation reactions of alkoxysilane precursors are very slow with 2 equivalents of water; this rate can be increase through the addition of acid or base catalysts. The choice of acid or base catalyst has a large impact on the resulting sol-gel product.

In general, for an acid catalyzed sol-gel reaction the rate of hydrolysis enhanced, whereas for base catalysis the rate of condensation is enhanced. To consider different structural developments of acid versus base catalyzed sol-gel reactions, it is important to consider how the electron density at the silicon center changes for different substituents:

Si-R > Si-OR > Si-OH > Si-O-Si

It is found that for acid catalysis linear chain-like networks are formed and branched (highly condensed) networks are obtained from base catalyzed sol-gel reactions.[1] As condensation perpetuates, aggregation of the sol particles occurs increasing the viscosity of the solution, eventually forming a gel, this is referred to as the sol-gel transition point.[1]

These methods can be extended to metal oxides, but for the purpose of the present thesis only silicon oxides will be considered. The precursor most common for the formation of SiO_2 is tetraethoxysilane (TEOS, $Si(OC_2H_5)_4$) and is the precusor used for any sol-gel reactions performed within the present thesis.